Serial No. N7641 NAFO SCR Doc. 25/014

SCIENTIFIC COUNCIL MEETING –JUNE 2025

Physical, Chemical, and Biological Oceanographic Conditions in the Labrador Sea in 2024

S. Clay, M. Ringuette, E. Devred, K. Azetsu-Scott, Z. Wang, B. Greenan, C. Gordon, D. Childs, and C. Layton

Bedford Institute of Oceanography
Fisheries and Oceans Canada, 1 Challenger Drive
Dartmouth, Nova Scotia, B2Y 4A2, Canada

CLAY, S., RINGUETTE, M., DEVRED, E., AZETSU-SCOTT, K., WANG, Z., GREENAN, B., GORDON, C., CHILDS, D., & LAYTON, C. 2025. Physical, Chemical, and Biological Oceanographic Conditions in the Labrador Sea in 2024. *NAFO Scientific Council Research Document*, SCR Doc. 25/014: 1-50.

Abstract

The Atlantic Zone Off-Shelf Monitoring Program (AZOMP) samples the AR7W line annually, extending from the Labrador Shelf to the Greenland Shelf. This report summarises the results from 2024 for three distinct regions: AR7W-W (Labrador shelf and slope), AR7W-C (central Labrador Sea), and AR7W-E (Greenland shelf and slope).

The winter 2024 NAO index was slightly below normal. Air temperature anomalies in the central Labrador Sea were positive, while sea surface temperatures were near normal in winter and spring, below normal in summer, and above normal in fall. Sea ice extent and concentration were generally lower than normal, with an unusually high concentration on the Greenland coast in winter and spring. Argo profiles revealed that surface and deep water were warmer and fresher than average.

Surface (0-100 m) nutrients were mainly below normal in 2024 in all regions, which could be attributed to mission timing. However, the below-average deep nutrients (>100 m, less impacted by sampling timing) in all three regions, which has persisted since 2019, suggests a profound change in the biogeochemistry of the Labrador Sea. This shift in nutrient budget coincides with a shift in Phytoplankton Apparent Absorption Wavelength toward positive anomalies, suggesting a possible change in overall biomass and cell structure, though this metric was negative again on the Labrador Shelf in 2024. Integrated (0-100 m) chlorophyll-a was slightly below normal in all three regions in 2024. Satellite data revealed a late spring bloom in AR7W-E and early elsewhere, late fall blooms on the shelves and early in the basin, and higher than normal concentrations of chlorophyll-a year-round. Mesozooplankton abundances are not yet available for 2024.

Introduction

The Labrador Sea is a deep basin nested between Labrador and Greenland with a cyclonic circulation pattern that leads to the mixing of Arctic and North Atlantic waters. The Baffin Island and Labrador currents transport cold and less-saline Arctic water southward along the Canadian coast (Wang et al., 2016). On the eastern side, the West Greenland Current brings warmer, more-saline waters northward, along the Greenland coast into the Baffin Bay, where it meets the Labrador Current (see Lozier et al. (2019) and Yashayaev I. and Loder (2017) for a detailed description of the Labrador Sea circulation). An ocean process called deep convection plays a vital role in the formation of dense water, which supplies the deep layers of the ocean. In this process, warm, buoyant water at the surface cools, becomes denser, and sinks to deeper layers (up to 2500 m). This vertical movement is a critical component of ocean circulation. The Labrador Sea is one of the few areas in the global ocean where surface water is exchanged with the deep ocean. It also has an important role in biogeochemical cycling in the Labrador Sea, and strong convection enhances the entrainment of gases such as oxygen and carbon dioxide into the deep water from the atmosphere, as well as from surface freshwater. The intensity of this phenomenon varies with environmental factors, including atmospheric forcing, freshwater runoff from adjacent glaciers, precipitation, intrusion of warm and saline inflow from the adjacent North Atlantic, and intrusion of cold and fresh water from the Arctic Ocean. In turn, this deep mixing strongly impacts heat flux, stratification, and by extension, the chemical balance and biological productivity of the Labrador Sea. Consequently, changes in the physical and chemical environment of the aphotic zone influence both plankton community composition and annual biological production cycles, including fish and higher trophic levels.

Since 1990, as part of the World Ocean Circulation Experiment (WOCE), the Ocean and Ecosystem Sciences Division (OESD) at the Bedford Institute of Oceanography (BIO) has carried out an annual occupation, usually in the spring, of the AR7W (Atlantic Repeat Hydrography Line 7 West) oceanographic section across the Labrador Sea (Figure 1). Soon after its inception, the program morphed into Fisheries and Oceans Canada (DFO) Atlantic Zone Off-shelf Monitoring Program (AZOMP), following the OESD's overarching objectives to: 1) characterize and understand the causes of ocean variability at seasonal, inter-annual, and inter-decadal scales; 2) provide adequate data to monitor the health of the marine ecosystem and support decision-making based on scientific evidence; and 3) to build historical databases to address future issues. The program also contributes to the international Global Climate Observing System (GCOS) and the Climate Variability (CLIVAR) component of the World Climate Research Program (WCRP), the Global Ship-based Hydrographic Investigations Program (GO-SHIP), the Global Ocean Acidification Observing Network (GOA-ON), the United Nations Sustainable Development Goals 14.3.1 (UN SDG14.3.1), the Global Ocean Data Analysis Project (GLODAP), and it reports annually with an environmental synopsis to the Northwest Atlantic Fisheries Organization (NAFO). The annual AZOMP multidisciplinary survey of the Labrador Sea primarily consists of AR7W occupations and deployments/recoveries of moorings and Argo floats. The ideal timing of the mission in May aims to capture the fading winter-deep-convection signal and the beginning of the phytoplankton bloom and productivity season, while avoiding possible sea ice on the Labrador shelf early in the spring. With nearly three decades of measurements, the time series allows examination of decadal trends in all key ecosystem variables (i.e, temperature, nutrients, plankton biomass and abundance).

Shipboard observations play a crucial role in studying changes in the ocean, complementing the valuable data provided by the Argo program. While Argo floats offer a large, three-dimensional view of the upper ocean, shipboard observations provide a more comprehensive and detailed picture. Ships can carry a wider array of instruments, allowing for measurements of various physical, chemical, and biological properties. This includes high-resolution sampling of the water column, collection of chemical and biological samples, and direct observations of surface phenomena. In addition, shipboard observations offer flexibility, adaptability, and can be strategically deployed to investigate specific regions or phenomena of interest. This targeted approach allows for focused investigations and the collection of unique datasets that may not be captured by the more standardized Argo network. Ships can also carry out long-term time-series measurements at fixed locations, providing crucial insights into the variability and trends of ocean properties over time, and this is one of many merits of the on-going AZOMP program for the AR7W line.

The upper layers of the Labrador Sea exhibit significant interannual variability in temperature and salinity. These fluctuations are primarily driven by three key factors: 1) atmospheric forcing, 2) variations in the warm and saline inflows of the West Greenland Current, and 3) changes in freshwater input from both liquid and ice sources originating from the Arctic and Greenland. Seasonal cycles in each of these forcing mechanisms induce a pronounced seasonal cycle in the upper ocean properties of the Labrador Sea.

During the early 1990s, deep winter convection within the Labrador Sea resulted in the upper two kilometers of the water column being filled with cold, fresh water. However, milder winters in recent decades have led to more limited formation of mode waters, which have also become warmer, saltier, and less dense compared to those observed a decade and a half ago. This trend experienced an abrupt shift during the exceptionally cold winter of 2008, when deep convection extended to a depth of 1600 meters. The specific environmental conditions that facilitated this deep convection event in 2008 have been comprehensively documented by Yashayaev I. and Loder (2009).

About one quarter of the carbon dioxide (CO_2) released by human activities is taken up by the global ocean (Sabine et al., 2004), altering ocean chemistry, and correspondingly, the marine carbonate system. The Labrador Sea hosts a strong "solubility pump", whereby anthropogenic CO_2 sequestrated from the atmosphere is transported to the deep ocean through chemical and physical processes. The dissolution of anthropogenic CO_2 has decreased global ocean pH by 0.1 units over the past 200 years, resulting in a 30% increase in acidity (Caldeira and Wickett, 2003). If global emissions of CO_2 remain at their present rate, ocean pH is predicted to drop by an additional 0.3 units by 2100. The oceans have not experienced such a rapid pH decrease (ocean acidification), or one of such a high magnitude, for at least 20 million years (Feely et al., 2004), raising serious concerns about the ability of marine ecosystems to adapt. The major impact of decreasing pH will be felt by organisms that form calcium carbonate ($CaCO_3$) shells and skeletons, because rising acidity increases the solubility of $CaCO_3$. Since $CaCO_3$ shells and skeletons are naturally more soluble at lower temperatures and higher pressures, high latitudes and deep water ecosystems, such as the one encountered in the Labrador Sea, are more vulnerable to the added stress of ocean acidification than those at intermediate latitudes. Ocean acidification also influences the capacity of the ocean to take up CO_2 from the atmosphere. Furthermore, rapid environmental changes, such as receding sea-ice extent and enhanced hydrological cycles, may amplify these problems.

Transient tracers dichlorodifluoromethane (CFC-12) and sulfur hexafluoride (SF_6) are used to study ocean circulation, ventilation, and mixing processes. Specifically, they are used to study ventilation rates and age determination of water masses. As the Labrador Sea is the site of direct uptake of these tracers by deep convection during winter, these measurements provide the boundary conditions for the global network of tracer observations, which are used to trace ocean circulation pathways such as spreading of North Atlantic Deep Water. These tracers are also used to estimate anthropogenic CO_2 storage and track their changes (Haine and Hall, 2002; Hall et al., 2002; L. Raimondi et al., 2021).

The AR7W transect crosses two productive shelves (Labrador and Greenland shelves) and the central Labrador Sea, where phytoplankton production is subject to local forcing (eddies, mixing, stratification) that drive phytoplankton biomass and community structure. In the central Labrador Sea, light limits primary production for most of the year (Fragoso et al., 2016; Harrison and Li, 2008), while a shallow mixed layer, and relatively low nitrate concentration, limit phytoplankton growth on the Labrador shelf following the spring bloom. Phytoplankton growth, in particular diatoms, also seemed to be limited by availability of silicate in the central Labrador Sea (Harrison and Li, 2008). These conditions support the emergence of small flagellates such as *Phaeocystis pouchetii* in the northern and eastern region of the Labrador Sea, which can form large blooms under favorable conditions (Fragoso et al., 2016). In recent years, large blooms of *Phaeocystis spp.* have also been observed in the western part of the central Labrador Sea (Devred et al., 2024). The Labrador shelf, influenced by Arctic waters, is dominated by polar diatom species (*Thalassiosira spp.*, *Chaetoceros spp.*, and *Bacteriosira bathyomphala*) and species associated with sea-ice (*Porosira glacialis* and *Fossula arctica*). Primary production patterns and mesoscale features leave their imprint on the mesozooplankton distribution and abundance (Yebra et al., 2009). One species of copepod, *Calanus finmarchicus*, dominates the mesozooplankton biomass throughout the central region of the Labrador Sea, while on the shelves, two Arctic *Calanus* species, *C. glacialis* and *C. hyperboreus*, are equally important (Head et al., 2003). *C. finmarchicus* abundance shows regional variations that are generally consistent from year-to-year and are related to differences in the timing of life-cycle events, which are influenced by environmental conditions, including spring bloom dynamics.

This report describes the physical, chemical, and biological state of the Labrador Sea in 2024. Data presented in this report come from: 1) the annual survey carried out over a 3-week period, typically between early May and early June depending on vessel and crew availability; 2) satellite remote-sensing of daily observations of ocean colour converted into chlorophyll-a concentration (chl-a), and 3) Argo float data for temperature, oxygen, and occasionally dissolved oxygen when available in sufficient concentrations.

Data and Methods

In situ samples collection

Missions

AZOMP sampling period is dictated by the Canadian Coast Guard operational constraints and ship availability, which has been challenging since the 2010's due to mechanical issues with the research vessel CCGS Hudson. From 2008 to 2018 (except 2013), AZOMP missions have started slightly early each year, with about 25 days difference over the entire period (Figure 2). The timing of the mission has been highly variable since 2019 with the chartering of foreign oceanographic vessels, and the 2021 mission was skipped entirely due to the lack of ship availability. In addition, the COVID pandemic in 2020 prevented the chartering of foreign vessels and the mission was only possible on the CCGS Amundsen at a later date in July – August.

In 2024, the mission (CAR2024924) aboard the CCGS Captain Jacques Cartier started on May 27th in St. John's and concluded on June 18th, 2024, at the Bedford Institute of Oceanography. Samples were collected from the Labrador Sea from May 29th to June 9th. A total of 87 hydrographic and 6 biological stations were sampled, and 72 plankton net operations, including 14 Multinet vertical tows, were performed. Stations planned for the Greenland shelf region were not executed due to the presence of drifting pack ice and poor visibility due to fog.

Core stations

The core stations (Figure 1) remain the priority of the monitoring program to ensure geographical consistency over time when reporting on the data. The main goal of the sampling is to obtain a complete suite of measurements at selected locations from surface to bottom to characterize the physical and chemical properties of the entire water column, while measurements of biological properties are restricted to the upper layers (0 to 100 m).

The CTD (Conductivity, Temperature, Depth)-rosette system is used to collect water at 24 selected depths distributed over the entire water column using 12 L Niskin bottles and profiles of physical and biogeochemical properties are recorded using a core of twinned sensors for temperature, salinity and oxygen, as well as additional sensors to measure fluorescence (both chl-a and Colored Dissolved Organic Matter (CDOM)), pH, light attenuation, Photosynthetically Active Radiation (PAR) and current velocity (LADCP). CTD profiles are collected on both the downcast and upcast from surface to near bottom (often several thousand meters deep). The CTD-rosette is first lowered down to 10 m due to the requirement for an underwater acclimation period at depth for the sensors, and this part of the cast is removed during quality control processing. Following the acclimation period, the CTD-rosette system is brought as close as possible to the surface but, partly because of the ship's movements, it does not reach the theoretical 0 m depth. Surface values are obtained by linear extrapolation of the temperatures at the two depths closest to the surface. The CTD is then lowered to within 7 to 12 meters of the bottom depending on sea conditions. The speed of descent is around 0.5 m/s for the top and bottom 200 m and 1 m/s otherwise. At the bottom, the CTD is stopped to acclimate for at least one minute before beginning its ascent (Mitchell et al., 2002). The same acclimation procedure is applied on the upcast at each depth where one or more bottles are closed. The CTD sensor data is recorded from the scan that occurs at the moment the bottle is closed to use in conjunction with the water sample data (see section 2.4.1). The full downcast CTD profiles are presented in conjunction with the physical data (section 2.2) as the downcast is not interrupted to close the bottles. Data for pressure, temperature, conductivity, salinity, and dissolved oxygen undergo rigorous calibration and quality control to meet WOCE standards. This process utilizes data from water samples (e.g., Autosal salinity and Winkler titration), SBE35 temperature recorders, and laboratory calibrations.

When the CTD-rosette returns to the deck, water samples are immediately collected to measure transient gases (CFC-12 and SF_6), oxygen, partial pressure of carbon dioxide (pCO_2), Total Inorganic Carbon (TIC), alkalinity, pH, nutrients, and salinity. In addition to the previous measurements, four bottles located in the surface-layer (2, 25, 50 and 100 m) are sampled for chl-a and cell abundance (Flow Cytometry). The 2 m depth is sampled for phytoplankton absorption and pigment composition, particulate organic carbon, and

CDOM absorption. The collection of water from the Niskin bottles is carried out as listed previously (i.e., gases first and phytoplankton last) from bottom to surface waters to minimize the loss of transient tracers and other gases during sampling. All variables were sampled and analyzed following GO-SHIP protocols (Hood et al., 2010; Mitchell et al., 2002). In addition to water sampling from the Niskin bottles, mesozooplankton are collected in vertical net hauls in the upper 100 m using a 0.75 m diameter ring net fitted with a 200 µm mesh, and 0.5 m diameter ring net with a 76 µm mesh size. A detailed description of the processing of the physical oceanographic data is presented in Yashayaev I. et al. (2021).

When time allows, additional stations are added between core stations in order to increase the spatial resolution of the sampling. However, at these stations only measurements from the sensors located on the CTD-Rosette are recorded and water is not collected unless requested by programs outside the core program. At these stations, the CTD-Rosette system is lowered to the ocean bottom to profile the entire water column.

Biological stations

The purpose of these stations is to increase the vertical resolution compared to core stations where only four depths are sampled over the first 100 m, and to carry out Photosynthesis-Irradiance (P-I) 14C-uptake experiments with phytoplankton (water) samples. In these experiments, 20 aliquots of phytoplankton from two depths (surface and close to the deep chl-a maximum) are incubated with 14C-bicarbonate at in situ temperatures and 20 light levels (+ 3 dark bottles) for approximately 3 hours. The P-I measurements are used to estimate the rate of primary production according to Platt and Jassby (1976). The timing of the 14C experiments at the biological stations is more critical than the exact location, so the vessel is stopped mid-morning at any location on the AR7W transect in order to start the incubations around noon (Halifax time) to ensure consistency of the method. Because the biological stations focus on the upper layers of the water column, the CTD sensor is only lowered to 200 m, allowing for a greater vertical resolution of all the biogeochemical parameters. Bottles are closed at 2, 10, 20, 30, 40, 50, 60, 80, 100, and 150 m, with an additional bottle at the depth of the deep chl-a maximum, as revealed by the in situ fluorescence sensor. In general, a total of seven biological stations are sampled, which are spread along the AR7W transect: two on the Labrador shelf, three in the central Labrador Sea, and two on the Greenland shelf.

Mission data presented in this report

In the current report, we present the data for a subset of the in situ measurements listed in this subsection, which includes: CTD data (temperature, salinity, and density), transient tracers, TIC, pH, nutrients, chl-a, and mesozooplankton abundances. The remaining datasets are available from the Canadian Integrated Ocean Observing System (CIOOS, https://cioos.ca) and Open Data (https://search.open.canada.ca). Links can be provided upon request to the corresponding author.

Physical data

North Atlantic Oscillation (NAO) Index

The NAO index data were downloaded from the Physical Sciences Laboratory at NOAA (Table 1). The winter (January to March) NAO index anomalies presented in this report were calculated by subtracting the climatology (2001-2020) from the winter NAO index.

Air temperatures

Air temperature data for this study were obtained from the NCEP Reanalysis dataset, a joint project by the National Centers for Environmental Prediction (NCEP) and the National Center for Atmospheric Research (NCAR) (Table 1). This dataset provides a comprehensive analysis of historical surface air temperature since 1948, along with near-real-time analyses of the current atmospheric state (Kalnay et al., 1996).

To investigate air temperature variations over the central Labrador Sea, as defined by I. Yashayaev (2007), we focused on the area within 150 km of the AR7W line where bottom depth exceeds 3300 m (P3300, the magenta polygon in Figure 1). Air temperature anomalies were computed by subtracting the seasonal climatologies (2001-2020) from the data, offering a clear view of deviations from long-term averages. Seasons were defined as follows: January to March (winter), April to June (spring), July to September (summer), and October to December (winter).

Sea surface temperature (SST)

The sea surface temperature (SST) data used in this study were sourced from the Hadley Centre Sea Ice and Sea Surface Temperature (HadISST) dataset (Rayner et al., 2003). HadISST is a widely recognized gridded dataset that provides historical records of global SST and sea ice concentration. HadISST combines observations from various sources, including ships, buoys, and satellites. It employs statistical interpolation methods to create a comprehensive global coverage of SST and sea ice data. Areas covered by sea ice are assigned a value of -1.8 °C. The HadISST dataset spans the period from 1870 to the present, offering a valuable long-term perspective on oceanic conditions. It is a crucial resource for understanding historical and ongoing changes in global sea surface temperatures and sea ice extent. The data were downloaded from Met Office Hadley Centre observations datasets (Table 1). Similar to the air temperature analysis, the seasonal SST anomalies were derived by subtracting the 2001-2020 climatologies from the data, where seasons are defined as in section 2.1 and analyses are focused on the area within the P3300 polygon (Figure 1).

Sea ice extent and concentration

Sea ice concentrations derived from satellite passive microwave data since late 1978 were obtained from the U.S. National Snow and Ice Data Center (Table 1) (Cavalieri et al., 1996; Fetterer et al., 2017). Monthly sea ice concentration climatologies were calculated for the reference period 2001-2020, and standardized anomalies were calculated for 2024 using this reference period. Ice extent was defined as the area in which sea ice concentration was at least 15%.

Argo profiling float data

The Argo program is a global array of about 4000 free-drifting profiling floats that measure the temperature and salinity of the upper 2000 m of the ocean (Table 1, Wong et al. (2020)). Argo floats are essentially robotic oceanographers that are deployed from ships to autonomously collect and report data for their entire lifetime, typically about 5 years. The main advantage of Argo floats is their ability to take measurements all year long with a large spatial distribution when compared to ship-based measurements. Limitations of this approach include the absence of control of the sampling location, and a sampling depth limit of 2000 m (however, deep Argo floats with depths ranging from 3500 to 6000 m are currently being deployed).

The float sinks to a predetermined depth (typically around 1000 meters) and drifts with the ocean currents. After a set period (usually 10 days), the float descends to 2000 m using a bladder system to regulate its density (and hence its buoyancy), and then begins its ascent toward the surface. During its ascent, the float measures temperature, salinity, and pressure of the water column. Some biogeochemical floats are further equipped with oxygen, chlorophyll fluoresence, particulate backscatter, pH, nitrate, or radiometry sensors. Once at the surface, the float transmits the collected data via Iridium satellite to scientists on land where it is openly available within 24 hours. The float then repeats this cycle, providing a continuous stream of valuable oceanographic data.

Data was downloaded using the Python package *argopy* (Maze and Balem, 2020). To investigate changes in ocean conditions, we focused on three depth ranges within the water column: 100-500 dbar, 500-1000 dbar, and 1000-2000 dbar. A climatology was established by averaging values over the period 2002-2020. The climatology was either calculated within 1 degree by 1 degree grid boxes (Figures 9-15) or monthly means within the P3300 polygon (Figures 16-17), using all available Argo float profiles after standard quality control processing. The anomaly for 2024 was then calculated as the deviation of 2024 conditions from the appropriate climatological baseline.

Mixed Layer Depth and convection depth

To estimate the 2024 winter convection depth in the Labrador Sea, we analyzed CTD data from the AR7W line survey conducted in 2024. Two distinct methodologies were employed: 1) Mixed Layer Depth (MLD) Approach: We calculated the MLD using an adaptation of the 'ra_mld.m' MATLAB function (Patel, 2025). The temperature difference criterion within the function was set to 0.29 °C. This approach assumes the base of the mixed layer corresponds to the depth of active convective process. 2) Vertical Temperature Gradient Maximum Approach: This method postulates that the depth of maximum vertical temperature gradient coincides with the deepest extent of convective mixing.

Recognizing that the upper 400m of the water column exhibited significant temperature and salinity variability, primarily driven by upper-ocean dynamics/processes rather than deep convection, we excluded this layer from our convection depth calculations. This exclusion ensured a focus on the deeper, convection-driven processes. In addition, the established climatology of Labrador Sea convection, as documented by Yashayaev I. and Loder (2016) and I. Yashayaev (2024), indicates convection depths exceeding 500m throughout the period from the early 1990s to 2023, even during periods of very low winter NAO index.

Chemical data

Transient tracers SF_6 and CFC-12

Prior to analysis, seawater samples from the rosette were drawn directly into 250 mL glass syringes and were stored at approximately 4 °C in a low-temperature incubator for up to 12 hours. Immediately before analysis, the samples were warmed to approximately 20 °C in a water bath then injected into the purge vessel of a custom-made purge-and-trap system, where dissolved gases were stripped from the sample in a stream of ultra-high-purity nitrogen with a flow rate of 140 mL per minute. The SF_6 and CFC-12 gases were quantitatively retained in a trap comprised of 30 cm of 1/16" diameter stainless steel tubing packed with 100–120 mesh Carboxen 1000, held at -70 °C over liquid nitrogen. After each 7 minute purge cycle, the trap was heated to 180 °C with a low-voltage electric current and the desorbed gases directed to a Varian gas chromatograph equipped with an electron-capture detector. SF_6 and CFC-12 were separated on a one-meter pre-column packed with Porasil B and a three-meter main column packed with Molecular Sieve 5A held isothermally at 100 °C. Total run-time was 11.5 minutes for each sample. The chromatographic sample peaks were quantified with Varian Galaxie software and the analytical system calibrated at least once each day using an air standard supplied by the Climate Monitoring and Diagnostics Laboratory of the National Oceanic and Atmospheric Administration (CMDL/NOAA), Boulder, Colorado. Analytical precision, as determined by repeated standard injections, was around ± 2% for SF_6 and ± 0.7% for CFC-12. (Punshon et al., 2016)

Total Inorganic Carbon (TIC), Total Alkalinity (TA), and pH

Samples for Total Inorganic Carbon (TIC) and Total Alkalinity (TA) were collected in 500 mL borosilicate glass bottles. Before 2013, TIC and TA were measured onboard within six hours of sample collection. After 2013, samples were preserved with mercuric chloride following best practices described by Dickson et al. (2007) and stored at room temperature until analysis at BIO's chemical laboratory. TIC was measured using gas extraction and coulometric titration with photometric endpoint detection (Johnson et al., 1987). TA was measured by open-cell potentiometric titration with full-curve Gran Point determination using a Titrando dosimat with Tiamo software, along with a sample delivery system that was built in-house. Certified Reference Material (CRM) (supplied by Professor Andrew Dickson, Scripps Institution of Oceanography, San Diego, USA) was analyzed in duplicate every 20 samples to ensure accuracy.

Spectrophotometric pH measurements, using an Agilent 8453 UV-Vis spectrophotometer, began in 2009. Samples were collected in 60 mL borosilicate glass tubes, stored at 4 °C, and analyzed onboard within six hours of collection following best practices (Dickson et al., 2007). Detailed methods for TIC, TA, and pH analyses are described in Punshon et al. (2019) and Raimondi L. et al. (2019).

pH values were calculated from TIC and TA measurements using CO2SYS, applying the dissociation constants of Lueker et al. (2000), and are presented here to ensure consistency throughout the study period. However, in 2012 and 2014, pH values were derived using direct pH measurements and TIC due to a TA instrument failure. All pH values are reported on the total scale.

Spatio-temporal binning and trend calculations

Statistics were limited to samples collected within 150 to 500 m depth and stations from 56°N to 59.1°N along the AR7W line. These samples were considered representative of the Newly Ventilated Labrador Sea Water (NV-LSW) as they are less impacted by seasonal variability than surrounding waters (Azetsu-Scott et al., 2003).

Tracer, TIC, and pH data were averaged annually over the NV-LSW and presented as time series in Figures 22 and 21. Linear trends were calculated for SF_6, TIC, and pH using an ordinary least squares method, as each exhibited monotonic trends over time. Note that pH is a logarithmic expression of hydrogen ion concentration, which is the actual measure of acidity. Because of this, a unit change in pH corresponds to a tenfold change in $[H^+]$, meaning that shifts at lower pH levels reflect much larger changes in acidity than equivalent shifts at higher pH.

Biological data

Surface temperature (0 to 100 m)

While the CTD downcast provides the temperature profile of the entire water column at high resolution, for this metric we used the temperature data recorded at the discrete depths at which water was collected for biological sampling during the CTD upcast (see section 2.1).

Nutrients

Nutrient measurements were made using a SEAL Analytical continuous-flow AutoAnalyzer 3 (AA3) and concentrations are expressed in micromoles per liter. The analytical methods have been modified from the historically used Technicon II: Technicon for Seawater Analysis (Silicate 186 72W, Phosphate 155 71W, Nitrate/Nitrite 158 71W) (Kérouel and Aminot, 1997) so as to remain compatible with methods described in the nutrient section of The GO-SHIP Repeat Hydrography Manual (Becker et al., 2020). Duplicate nutrient samples were drawn into 10 ml collection vials directly from the rosette without using tubing, with technicians wearing vinyl gloves to avoid contamination. Since 2024, samples were filtered through a 0.2 µm mesh filter to avoid potential contamination by particulate material. Samples were stored at 4 °C and analyzed within 12 hours. Five dissolved inorganic nutrients were analyzed, namely, nitrate plus nitrite ($NO_3 + NO_2$), nitrite (NO_2), phosphate (PO_4), silicate (SiO_4), and ammonium (NH_4). Note that in 2023 and 2024, nutrients were frozen and analyzed upon return to BIO due to a lack of laboratory space in the fishing trawler CCGS Jacques Cartier preventing the installation of the auto-analyser.

The instrument was calibrated for every analytical run, using a six-point calibration curve from pre-made solutions diluted using artificial seawater of same salinity as the samples, distributed over the concentration range for each nutrient. The analysis was followed by a drift standards analysis and blank samples to determine the method’s detection limits. The baseline was re-assessed every 12 sample duplicates (i.e., every 6 samples). The pH of the imidazole buffer was monitored to ensure optimal pH levels (i.e. approximately 7.83-7.85) for the nitrate plus nitrite analyses, and adjusted as needed using hydrochloric acid, thus improving the lifespan and stability of the cadmium reduction column. Ultimately, this method diminished drift issues observed in the past between analytical runs.

The quality of these analyses was validated by analyzing a CRM for nutrients produced by KANSO Co., Ltd, Japan. There is no existing reference material for ammonium in seawater, although CRM values were tracked for consistency. The mean of the duplicates is used in this report.

In situ chlorophyll-a concentration

Phytoplankton biomass is represented by the concentration of its main pigment, chl-a, which was measured using Turner fluorometry (Yentsch and Menzel, 1963). Details of the protocol and method can be found in Mitchell et al. (2002). In brief, two replicates of 100 mL aliquots of seawater were drawn from each sampling depth and filtered via vacuum filtration (PSI < 10) onto 25 mm glass fiber filters (GF/F). The GF/Fs were immediately deposited into separate scintillation vials containing 10 mL of 90% acetone, which were kept at -20 °C for at least 24 hours to ensure extraction of all the chl-a pigments. Following the extraction period, the aliquots were warmed to room temperature and transferred into fluorometer cuvettes (glass test tubes). The extracts were exposed to blue light (excitation wavelengths) in the fluorometer, which leads them to emit red light. This red light is detected and quantified by a photomultiplier (Holm-Hansen et al., 1965). Chloropigments other than chl-a (e.g., chlorophyll-b, chlorophyll-c1, -c2, and -c3) can contribute to the overall fluorescence signal, but their contribution is generally minor. Chl-a degradation products (a-type phaeopigments associated with senescent phytoplankton or zooplankton fecal pellets) may sometimes be present in a sample and contribute to the fluorescent signal. To account for their contribution, after taking the first fluorescence measurement, samples were acidified, which converts chl-a into phaeophytin-a. A conversion factor was then applied to retrieve the concentrations of both the chl-a and a-type phaeopigments (Welschmeyer, 1994).

Phytoplankton Apparent Absorption Wavelength (PAAW)

PAAW is the harmonic mean of the phytoplankton absorption spectrum from 400 to 700 nm, namely, the wavelength-weighted mean of phytoplankton absorption coefficients. This approach emphasizes the absorption values in the blue/green (short) wavelengths rather than the red (long) wavelengths (Devred et al., 2022) and provides a single metric in nm that summarises the shape of the absorption spectrum, which changes depending on total phytoplankton biomass and community composition. In the Labrador Sea, PAAW varies from about 461 nm (blue/green) to 498 nm (orange), the low values being indicative of low biomass and likely small phytoplankton cells, while the higher wavelengths suggest high biomass and a phytoplankton community structure dominated by large cells such as diatoms.

Surface (1-2 m depth) water samples (250 to 1000 mL depending on visual inspection of the filter to ensure enough material was retained) were filtered on a GF/F 25 mm filter immediately after collection from the Niskin bottle, flash frozen in liquid nitrogen, and stored in a -80°C freezer until analysis upon return to BIO. Particulate absorbance was measured on the filter using a UV-Vis Shimadzu 2600i using an integrating sphere, and the filter was then placed in hot methanol (60°C) for 25 to 45 minutes to extract pigments. A second measurement of the filter after pigment extraction was performed to obtain detritus absorbance. Particulate and detritus absorption were derived by using the path length correction formula from Stramski et al. (2015) with coefficients from Equation 5.5 in Neeley et al. (2018) on the absorbance values. Phytoplankton absorption (m^{-1}) was calculated by subtracting detritus absorption from particulate absorption, and the spectra were smoothed using the *smooth.spline* function from the *stats* package in *R* (R Core Team, 2022) with the degree of smoothing set to 55. The absorption at 700 nm was subtracted from the spectrum, assuming the absorption at 700 nm would be zero. Finally, PAAW was calculated using the smoothed phytoplankton absorption as input to the equation from Devred et al. (2022).

Satellite-derived chlorophyll-a concentration and bloom metrics

In addition to in situ measurements, chl-a concentrations were derived using satellite ocean colour. This mode of observation provides information on phytoplankton biomass at synoptic scales and daily frequency (assuming clear skies). These satellite-derived data are used to complement the in-situ observations by providing context to the seagoing missions, including a suite of metrics to characterize the phytoplankton spring bloom (described below in this section). Satellite data presented in this document were retrieved from the OC-CCI multi-sensor product generated by the Plymouth Marine Laboratory (PML) as part of the European Space Agency (ESA) climate change initiative (Table 1), which provides daily data from September 1997 to the present. Previous reports used data from the MODIS-Aqua sensor alone, which was launched in 2002. However, there has been a decline in data quality from this sensor since 2023, and therefore a decision was made to adopt the OC-CCI product, which offers improved spatial and temporal coverage due to the use of multiple satellite optical sensors.

For this report, global daily level-3 binned data at 4 km resolution were downloaded from PML (Table 1) and data were extracted for the three regions of interest, namely, AR7W-West (AR7W-W, -55.7°E to -53.7°E and 53.6°N to 55.5°N), AR7W-Central (AR7W-C, -53.7°E to -48.8°E and 55.5°N to 60.1°N), and AR7W-East (AR7W-E, -48.8°E to -48.1°E and 60.1°N to 60.7°N) (Figure 1). The boundaries of these boxes were designed to delineate the main regions along the AR7W line: Labrador shelf and slope, central Labrador Sea, and the Greenland shelf and slope. In previous reports, these polygons were referred to as the Labrador Shelf (LAS), Central Labrador Sea (CLS), and the Greenland Shelf (GS), respectively, but have been renamed to reduce confusion when referring to the shelves or the central Labrador Sea as a whole. Remote sensing reflectances were used to generate chl-a using the POLY4 algorithm (Clay et al., 2019), a modified version of the band ratio model OCx (O'Reilly et al., 1998) with regionally-tuned coefficients to correct for a bias observed in the Northwest Atlantic.

Metrics were derived from satellite chl-a using the PhytoFit R shiny app (Clay et al. (2021), see Table 1). Data were $\log_{10}$-transformed to allow better modelling of the exponential increase in chl-a at the initiation of the bloom. Daily averages and standard deviations were calculated within each of the three Labrador Sea polygons (AR7W-W, AR7W-C, and AR7W-E), filtering pixels outside ±3 standard deviations from the mean. Days with less than 20 % coverage were excluded from the time series, and the remaining points were smoothed using the LOESS method (locally-estimated scatterplot smoothing) as implemented in *R* (*loess* function, R Core Team (2022)) with a span window of 0.2 (a parameter that controls the degree of smoothing) and weighted by percent coverage (i.e. percent area of the region of interest that is observed by the satellite, as cloud cover results in missing data). A symmetric shifted Gaussian was fitted to the smoothed points with nonlinear least squares regression using the *nlsLM* function of the *minpack.lm* package in *R* (Elzhov et al., 2023), and the chl-a baseline was allowed to vary linearly as a function of time. The Gaussian fits were restricted to days 85 to 299, and the day of initiation and day of maximum concentration were restricted to day ranges 85-226 and 108-247, respectively to avoid classification of small early peaks of the spring bloom.

In previous reports, the spring bloom metrics (the timing of the start of the bloom, the duration, peak concentration during the bloom period, and "magnitude" or total chl-a produced during the bloom period) relied mainly on the accuracy of the Gaussian fit, which was subject to high variability in chl-a concentration and low data coverage, particularly in the north and early in the year. This resulted in an absence of model fits, or problematic fits that may not have accurately captured the interannual anomalies in each region. To reduce the impact of these bad fits on the scorecards, and retrieve information about bloom timing and intensity, a new set of a metrics were recently proposed: spring bloom peak timing and fall bloom initiation, and "seasonal" averages, where the season boundaries are region-specific and based on the climatology of the spring and fall bloom periods observed over the time series (See Figure 30, and Blais et al., in prep). While the spring metrics are still derived from a Gaussian fit, we now report on the peak of the curve instead of its initiation, as it does not require a subjective threshold (i.e., percentage of maximum chl-a) and it remains robust to small variation in chl-a early in spring. All fits were visually inspected to ensure that the bloom peak timing was accurately captured by the model, and the input parameters were adjusted if necessary.

The fall bloom period is less predictable than the spring bloom as its signal is not as large as in the spring, and satellite data are more sparse due to cloud cover. Rather than a Gaussian model, a threshold method was used to define the start of the bloom as the day of year when chl-a concentration surpasses 5% over the annual median and remains above this threshold for 14 consecutive days (Layton et al., 2022). In this case we used the LOESS-smoothed data spanning between day of year 151 and 365 with the initiation occurring between day of year 151 to 270. The timing of the fall bloom initiation was reported rather than the peak, as the peak may occur late in the year when data coverage is poor.

The mean chl-a for each region-specific "season" was calculated as an average of the daily chl-a concentrations within that season, weighted by daily percent coverage. Note that in this calculation, daily chl-a concentrations correspond to the averages calculated using absolute (i.e. not log-transformed) values within the polygons, after filtering outlying pixels. Data coverage is very sparse or non-existent in the

Labrador Sea from November to January (see Figure 30). Days with valid data that have low coverage (<20%), a common occurrence early or late in the year, might not be representative of the overall conditions. Sea ice also impacts the quality of the data and may introduce artifacts close to the ice edge (Bélanger et al., 2007). Although weighting points by percent coverage lessens the impact of low data coverage, extra caution must be used when interpreting results in late fall or winter due to these issues.

Mesozooplankton

Mesozooplankton were collected using vertical net hauls in the upper 100 m, where 95% of the biomass in spring-summer occurs (Astthorsson and Gislason, 2003), using a 0.75 m diameter ring net fitted with a 200 µm mesh size and a 0.5 m diameter ring net with a 76 µm mesh size. The cod-end was attached via a clamp to a weighted hydro-wire and the towing bridles were attached to a crossbow mounted on the wire, at a height equal to the length of the net such that the net was held vertically during the descent and ascent. In this configuration, zooplankton were only collected as the net was towed upwards. The towing speed was about 0.5 m s^{-1} and the volume of water sampled was assumed to be the volume of the cylinder sampled by the net, until 2010, when the filtered volumes started to be measured using a Danemark K/C flowmeter. The flowmeter was equipped with a back-spin pin, to prevent the impeller from spinning during the descent of the net, so that it only measured flow during the ascent. Samples were preserved in 2% formalin. For *C. finmarchicus*, *C. hyperboreus*, and *C. glacialis*, specimens were identified and enumerated to the level of species and stage, and size-frequency distributions of sizes-at-stage were constructed for all stages at each station. To track anomalies in reproduction events and population growth, the Population Development Index (%PDI) was calculated as the ratio of young copepodite stages (CI-CIII) over the total abundance, expressed as a percentage (Head et al., 2008). Other taxa were identified to the level of species (sometimes to stage), genus, or group, depending on their abundance in the samples. Meaningful abundances were obtained when a minimum of 300 organisms, and a minimum of 200 *Calanus spp.*, were counted to allow assessment of community structure and *Calanus* population growth/development, respectively.

Spatio-temporal binning

All data are aggregated following a spatio-temporal scheme to summarise the information in simple metrics. The data in this subsection are summarized over the three main regions of interest defined in section 2.4.5 (AR7W-W, AR7W-C, and AR7W-E, see Figure 1).

All nutrients and chl-a concentrations were integrated over selected depth ranges, namely, chl-a from 0 to 100 m, surface nutrients from 0 to 100 m, and deep nutrients from the first depth below 100 m to bottom. Temperatures were averaged from 0 to 100 m. Zooplankton values correspond to the integrated abundances in the water column (0–100 m) since collection was carried out using vertical net tows (see section 2.4.6). Following the vertical binning, the data were averaged by region and year.

Scorecards

Annual anomalies for surface temperature, surface and deep nutrients, chl-a concentration, mesozooplankton abundance, PAAW, and satellite ocean colour metrics were calculated as the deviation of an individual year from the mean of the annual estimates over a reference period (defined below), and expressed as normalized quantities (i.e., by dividing by the standard deviation of the annual estimates over the same period):

$$A_y = \left(M_y - M_r\right)/\sigma_r$$

where A_y is the anomaly for a given property in a given year (y) and region, M_y is the annual mean, M_r is the reference period mean and σ_r is the standard deviation for the reference period (1999-2020). This method was selected because it provides good estimates of anomalies and trends for data with large gradients and gaps (Jones and Hulme, 1996). Note that years when sampling occurred after day of year 170 (i.e. during summer, see 1998, 1999, 2002, 2003, and 2020 in Figure 2) were excluded from calculation of the in situ data reference period and omitted from the scorecards (Figures 23-26 and 29). These samples, collected in the summer rather than spring during the typical bloom period, would reflect a different dynamic and skew the climatology. Due to the lack of mission in 2017 and 2021, these cells are also greyed out in the scorecards.

Access to data products

Data products presented in the figures of this document are available on request to the corresponding author. The satellite ocean colour data can be found in Phytofit and the bloom metrics (i.e. bloom timing and weighted "seasonal" averages, see Figure 28) are available in the PhytoFit github repository (Table 1). All the chemical data are available at Ocean Carbon Data System (OCADS, Table 1).

Results and Discussion

Physical data

North Atlantic Oscillation (NAO) Index

The North Atlantic Oscillation (NAO) is a crucial teleconnection pattern that significantly impacts atmospheric processes in the Labrador Sea (Barnston and Livezey, 1987; Hauser et al., 2015). During a positive NAO phase, low-pressure anomalies over Iceland and the Arctic, coupled with high-pressure anomalies across the subtropical Atlantic, drive stronger-than-average westerly winds at mid-latitudes. This leads to colder and drier conditions in the northwestern Atlantic, including the Labrador Sea region. Conversely, a negative NAO weakens both the Icelandic low and the Azores high, reducing the pressure gradient across the North Atlantic and resulting in weaker westerlies and warmer conditions. Both NAO phases are associated with basin-wide changes in the intensity and location of the atmospheric jet stream and storm track over the North Atlantic ocean, as well as large-scale fluctuations in zonal and meridional heat and moisture transport (Hurrell, 1995). These changes ultimately modify temperature and precipitation patterns. While this report primarily focuses on the past several decades, we analyze the NAO record to contextualize recent conditions within the broader history of atmospheric patterns over the North Atlantic.

The wintertime (JFM) NAO exhibits significant multi-decadal variability (Hurrell (1995); Figure 3). A notable upward trend in the NAO index was observed from the 1960s to the 1990s (Visbeck et al., 2001). However, a slight downward trend followed the peak in the 1990s, persisting until 2010. Recent research has identified an atmospheric circulation pattern that becomes more pronounced during periods of low NAO (Hauser et al., 2015). Further investigation of this complementary pattern will enhance our comprehension of atmospheric and oceanic conditions, ultimately improving forecasting capabilities. In 2010, the NAO index reached a record low (Figure 3). The following year it rebounded, only to strengthen significantly in 2012, reaching levels comparable to the mid-1990s. A dramatic shift occurred in 2013, with the NAO index becoming strongly negative. The index returned to a high positive phase in 2014, though slightly weaker than 2012. Another peak in positive NAO values was observed in 2015, the largest since 1989. More recently, 2020 saw a strong positive NAO, followed by a moderate negative phase in 2021. In 2022, the NAO index returned to a strong positive phase, slightly weaker than 2020. 2024 exhibited a slightly negative NAO condition.

Air temperatures

In 2024, a pervasive warming trend is evident in nearly all seasons (Figure 4), with the exception of regions surrounding both sides of Greenland within the sub-arctic and small area in the south. The most pronounced warm anomalies are observed over the Hudson Bay and Baffin Bay during the winter, reaching values of approximately 4.0 °C and above over the climatological mean.

Figure 5 presents time series plots of air temperature anomalies within the central Labrador Sea (outlined by the black polygon, P3300) for the four seasons from 1950 to 2024. Mid-1980s experienced the lowest temperature in all the four seasons in this period, and 1993 recorded the second lowest temperature in the winter season. The air temperature in winter season appears to have stronger inter-annual variability than in the other three seasons, particularly in the spring and summer. In 2024, winter exhibited the most significant anomaly in the central Labrador Sea, with temperatures exceeding normal by 1.0 °C. Spring followed with a substantial warm anomaly of 0.8 °C, continuing a trend of positive anomalies that started in 2019. Summer experienced the least pronounced warming, at 0.3 °C, likely influenced by southward intrusions of cold anomalies originating from the Greenland region (as depicted in Figure 4). However, summer experienced a similar pattern to spring, with positive anomalies occurring since 2019 after a period of high variability (2009 to 2018). Fall recorded a warm anomaly of 0.7 °C, again a trend that started in 2020. Notably, these warming events within the central Labrador Sea coincided with the negative phase of the North Atlantic Oscillation (NAO) during the winter of 2024 (Figure 3).

Sea surface temperature (SST)

The summer exhibited the most pronounced anomalies (Figure 6), with significant warming in the southeast portion (>1.5 °C) and substantial cooling around Greenland (~ -1.0 °C). The spatial distribution of winter anomalies was more complex, showcasing a mix of both cold and warm areas, although warming generally prevailed. Spring anomalies displayed a pattern resembling summer but with generally smaller magnitudes. The anomalies in the fall are similar to the spring ones but with smaller positive anomalies and larger area of negative anomalies in the southern part of the region.

To illustrate SST variability in the central Labrador Sea, Figure 7 presents SST anomalies relative to the 2001-2020 climatology. Consistent with the air temperature, mid-1980s recorded the largest negative changes in all the four seasons, while the second largest ones were in early 1970s. SST variations at the Ocean Weather Station Bravo (56 °N, 51 °W; in the central Labrador Sea) investigated by Loder and Wang (2015) (see their Figure 3) are consistent with the pattern observed in summer in the current document (Figure 7). In 2024, winter and spring SST anomalies were generally close to normal (-0.06 °C and -0.05 °C, respectively). In contrast, summer anomalies were below normal (-0.23 °C), likely influenced by the southward intrusion of cold anomalies originating around Greenland, while fall anomalies were above normal (0.24 °C). Notably, these cold SST anomalies around Greenland closely mirrored cold air temperature anomalies observed in the same region. Unlike air temperature, no continuous positive anomalies have been observed over the last few years in any season, but rather a high variability with both positive and negative anomalies.

Sea ice observations

Sea ice extent in 2024 was lower than the climatology in January on the entire Labrador coast and close to the climatology extent along Greenland and around Newfoundland (Figure 8). In February and March the sea ice extent was close to normal on the Greenland and Labrador shelves, while it was significantly lower than normal around Newfoundland and in the Gulf of Saint Lawrence. Sea ice concentration was lower than normal in areas of reduced sea ice extent (i.e., Labrador Shelf, Newfoundland, and Gulf of Saint Lawrence) during the three winter months. A large positive anomaly occurred in March in the northern Labrador Sea near Davis Strait. On the Greenland Shelf, positive sea ice concentration anomalies persisted from January to March, which is consistent with observations from the May mission when the presence of sea ice on the Greenland shelf prevented sampling at those stations.

Argo profiling float data

Argo data is used to monitor the state of the ocean and to improve our understanding of climate variability and change, particularly during periods when ship and satellite measurements are limited. By tracking temperature changes at various depths, Argo data reveals the rate of ocean warming or cooling. This information is vital for understanding the impact of climate change on marine ecosystems and sea level rise. By measuring salinity variations, Argo data helps scientists understand how the global water cycle is being altered by climate change.

Since 2002, the near real-time temperature and salinity Argo float data collectively draw a large-scale picture of the world oceanographic structure in general and the Labrador Sea in particular. The array is typically used to reconstruct the seasonal and interannual variability of the physical characteristics and dissolved oxygen in the upper 2000 m water column. The value of the Argo floats is even more significant in winter, when they serve as the only means of providing information about real-time development of winter convection, and when there are no shipboard measurements available. Because of the “parking” depth of Argo floats (i.e. 1000 m), they do not sample on the shelves.

A total of 17490 profiles were used to compute the climatology by grouping them in 1° x 1° grid cells from 2002 to 2020 (Figure 9, left panel), and mean temperature, salinity, and density were computed for three layers: 100-500 dbar, 500-1000 dbar, and 1000-2000 dbar. In 2024, 1237 Argo profiles were collected across the entire Labrador Sea region (Figure 9, middle panel). Deployment of Argo floats in the Labrador Sea started in 2002 with about 150 measured profiles (Figure 9, right panel). The number of profiles increased continuously to about 1200 profiles in 2012, with a peak exceeding 2000 profiles in 2021.

The climatological temperature distribution in the 100-500 dbar layer (Figure 10, left panel) exhibits cold waters between 3 and 4 °C in the central and southeastern regions, as well as along the Labrador slope, contrasting with warmer (> 4 °C) waters observed elsewhere. The cold water along the Labrador slope is attributed to the influence of the Labrador Current as suggested by its temperature and salinity signature of fresh and cold waters. Conversely, the presence of warmer waters on the Greenland side indicates the influence of the Irminger Current, which advects warm salty Atlantic waters into the region. The climatological salinity distribution (Figure 11, left panel) reveals a band of fresher waters along the Labrador slope, while the majority of the region exhibits saltier waters.

The general temperature and salinity patterns observed in 2024 (Figures 10 and 11, middle panels) exhibit similarities to the climatological distributions, albeit with varying magnitudes. In 2024, the Labrador Sea experienced predominantly warmer-than-normal temperatures between 100 and 500 dbar, with relatively smaller anomalies in the central region and larger anomalies elsewhere (Figure 10, right panel). Sparse cold anomalies were also evident in the south and southeast regions. Regarding salinity, 2024 conditions revealed lower-than-normal values in the central region, while other areas, particularly in the north and west, exhibited saltier-than-normal conditions.

Figures 12 and 13 illustrate temperature and salinity distributions, respectively, within the 500-1000 dbar depth range. Both climatologies showed a smaller range of variations of both temperature and salinity compared to the ones for the surface layer (100-500 dbar). As depth increases, water masses become isolated from surface forcing, resulting in homogenization of the physical properties. This layer corresponds to the upper limit of the Labrador Sea Water resulting from winter convection (I. Yashayaev, 2007). The climatological distributions (Figure 12 and 13, left panels) reveal a pattern of cold and fresh waters in the central and southeastern regions, contrasting with warmer and saltier waters prevailing in other areas. At this depth range, the influence of the Irminger Current becomes more pronounced. While the temperature and salinity patterns observed in 2024 (Figure 12 and 13, middle panels) generally resemble their climatological counterparts, substantial differences in magnitude are evident.

Temperature anomalies (Figure 12, right panel) were predominantly positive, with sparse cold anomalies observed south of Greenland and in the central and southeastern regions. Salinity anomalies in 2024 (Figure 13, right panel) were largely negative, indicating fresher conditions.

The climatological temperature and salinity patterns at 1000-2000 dbar (Figures 14 and 15, left panels) exhibit similarities to those observed in the 500-1000 dbar depth range, which are typical of the Labrador Sea Water. While the general temperature and salinity features in 2024 (Figure 14 and 15, middle panels) resemble the climatology, significant magnitude differences are evident with 2024 being warmer and fresher than the climatology.

Warm temperature anomalies in 2024 (Figure 14, right panel) were primarily observed in the western portion of the Labrador Sea, with near-normal conditions dominating other areas. Sparse cold anomalies were present south of Greenland and in the southeastern region. Salinity anomalies in 2024 (Figure 15, right panel) were predominantly negative (fresher), with salty anomalies or near-normal conditions observed in the central zone.

Seasonal changes in the Labrador Sea within the 100–500 dbar depth range are a compelling research topic under a changing climate, particularly in the upper ocean layers. A monthly climatology of temperature and salinity for the central Labrador Sea was derived from Argo data spanning 2002–2020. The climatological temperature in the central Labrador Sea between 100 and 500 dbar (blue line, Figure 16) reaches its minimum in March (~3.5 °C) and maximum in November (~4.0 °C). Salinity in the same layer (Figure 17) is lowest in January (~35.00 psu) and highest in October (~35.02 psu).

In 2023 and 2024, temperatures in the central Labrador Sea closely followed the climatology. However, March 2023 was exceptionally cold, deviating by -0.24 °C from the climatology, making it the coldest month in the two-year period (Figure 16). In contrast, December 2024 was the warmest, exceeding the climatology by +0.24 °C. Conversely, salinity was consistently lower (fresher) than the climatology in every month of 2023 and 2024 (Figure 17). This freshening may indicate increased freshwater inputs, potentially from enhanced Greenland glacier melting or Arctic sea ice melt, driven by warming air temperatures at high latitudes (Schiller-Weiss et al., 2024).

Shipboard observations

To capture interannual variability amidst strong seasonal fluctuations in physical, chemical, and biological conditions, the annual AR7W surveys are conducted as early in the spring as feasible. Sea ice typically restricts access to the Labrador Shelf until mid-May. Each mission encompasses at least 30 stations between Labrador and Greenland, where CTD profiles are obtained, and water samples are collected at up to 24 depths. While CTD data are paramount, a comprehensive suite of sensors is routinely deployed on every AZOMP mission.

Due to an unforeseen staff shortage, climatological conditions derived from the CTD profiles along the AR7W line could not be included in this report. We plan to compile these climatologies for the next annual report, along with anomalies relative to these climatologies. This report currently describes only the conditions observed in 2024. Water on the Labrador Shelf is characterized by cold temperatures and low salinity, contrasting sharply with conditions in the Labrador basin. Therefore, we include an additional plot to illustrate the specific water conditions in this region.

In 2024, the surface waters were relatively warm, with temperatures gradually decreasing with depth (top panel of Figure 18). Relatively warm waters (4 to 5 °C) are present in the upper layer of the shelf break on both the Labrador and Greenland sides located below the cold surface layers, with warmer waters on the Greenland side, in agreement with Argo data. Warm waters are also observed in the central region from the surface to depths of approximately 500 m. A prominent thermocline (a zone of rapid temperature change) occurs near 500 m depth followed by a relatively constant temperature until 2000 m, and another thermocline from 2000 m to the bottom. The coldest water, below 2.5 °C, occurred below 2500 m and corresponds to the North Atlantic Deep Water and the Denmark Strait Overflow Water (I. Yashayaev, 2007).

Salinity generally increases with depth, which is typical for ocean environments (middle panel of Figure 18). The halocline, a zone of rapid salinity change, coincides with the thermocline as expected. This suggests that the factors controlling temperature also influence salinity distribution. The deep waters exhibit higher salinities compared to the surface waters.

Density generally increases with depth, following the trends in temperature and salinity (bottom panel of Figure 18). The pycnocline, the zone of rapid density change, is clearly defined and aligns with the thermocline and halocline. The deep waters are denser than the surface waters due to the combined effects of lower temperatures and higher salinities. An ongoing decrease in water density in deep layers has been identified as a mechanism for the weakening the Atlantic Meridional Overturning Circulation (AMOC; Wang et al. (2019)).

The Labrador Current, encompassing both its inshore and offshore branches, is a southward extension of the Baffin Island Current. It transports cold, relatively low-salinity waters originating from Baffin Bay and the Hudson Strait outflow (Wang et al., 2015). These waters are enriched with freshwater inputs from Arctic and subarctic sources, contributing to the current's distinct thermohaline characteristics. On the Labrador Shelf, a cold intermediate layer (CIL) is observed between approximately 20 m and 100 m depth (Figure 19), characterized by its low temperature and salinity. The low salinity and cold temperatures observed at the surface are thus likely a direct reflection of these freshwater influences, modulated by seasonal and regional oceanographic processes.

It is clear the central Labrador Sea water mass experienced significant changes over the 30 year-period as indicated by records of temperature, salinity, and density (Figure 20). In early 1990s, a cold, fresh and dense water mass was the dominant feature which is consistent with the high NAO indices (Figure 3) and low air temperatures (Figure 5) during this period, indicating the role of atmospheric forcing on the water mass formation in the Labrador Sea, resulting in a well-mixed water column during the winter from the surface to approximately 2000 m (Wang et al., 2019, 2022; I. Yashayaev, 2024; Yashayaev I. and Loder, 2016).

Mixed Layer Depth and convection depth

The parameters of both methodologies presented in section 2.2.6 were tuned against historical convection depth estimates (I. Yashayaev, 2024; Yashayaev I. and Loder, 2016) to ensure accuracy and consistency with the historical estimates. Our analyses yielded convection depth estimates in 2024 of 900 m (MLD approach) and 700 m (gradient maximum approach). The observed disparity underscores the sensitivity of convection depth estimates to the chosen methodology.

Chemical data

Transient tracers CFC-12 and SF_6

During the second half of the twentieth century, the atmospheric burden of CFCs increased steadily, due mainly to their widespread use as refrigerants and aerosol propellants. The invasive atmospheric flux of these mostly inert gases provided an excellent record of ocean circulation, and profiles of dissolved CFC-12 concentration have been measured annually along the AR7W line since 1991 (Figure 21). As a consequence of restrictions on the manufacturing and use of ozone-depleting substances introduced in 1989, the atmospheric mixing ratio of CFC-12 has been in decline since 2003 and its capacity at tracking recent ventilation episodes has become limited. Unfortunately, the instrument malfunctioned in 2022 and 2023, resulting in a lack of CFC-12 data for those years (Figure 21). Measurements of an alternative transient tracer, SF_6, were introduced in 2011. There has been a rapid, near-linear increase in atmospheric SF_6 since 2011 (+0.08 fmol kg^{-1} y^{-1}) and it is reflected in the dissolved concentration profiles of the NV-LSW (Figure 21). Data from 2023 requires additional quality control and is not yet available.

Total Inorganic Carbon and pH

The Labrador Sea hosts a strong "solubility pump": atmospheric anthropogenic CO_2 is sequestrated to the deep ocean by chemical and physical processes. The depth of the NV-LSW varies from year to year, ranging from 500 m to over 2000 m. TIC concentration increased by 0.84 µmol kg^{-1} y^{-1} from 1996 to 2023 (Figure 22). As a result, the pH decreased by 0.09 pH units during the same period (Figure 22) representing a decline rate of 0.003 y^{-1}. Trends between 1996 and 2023 were highly significant with a correlation coefficient, r^2, explaining respectively 97% and 80% of the variance in TIC and pH, respectively. Notably, the increasing trend in TIC concentration from 2019 to the 2022 peak was lower overall at 0.51 µmol kg^{-1} y^{-1} (not shown). Arctic outflow and the local uptake of anthropogenic CO_2 in the deep-convection region of the Labrador Sea are major controlling mechanisms for the state of ocean acidification in the Northwest Atlantic. The observed progress of acidification affects not only the local region but also downstream areas. The Arctic water inflows to the highly productive regions in the Northwest Atlantic, which have important commercial fisheries and make these regions more susceptible to future ocean acidification than other regions (Azetsu-Scott et al., 2010).

Biological data

Surface temperature (0 to 100 m)

Because the timing of the cruise affects the average temperature for a given region and year, removal of the years 1998, 1999, 2002, 2003, and 2020 (due to later-than-usual sampling dates, Figure 2) from the reference period (1999-2020) lowered the temperature by about 0.2 °C with little effect on the anomaly patterns (not shown here). AR7W-W exhibited a lower temperature in the top 100 m (mean of 0.8 °C) than AR7W-C (mean of 3.8 °C) and AR7W-E (mean of 2.2 °C) due to the inflow of Arctic water (Figure 23). The warmest years occurred in 2000 (AR7W-W, +1.71 standard deviations from the mean, unitless), 2019 (AR7W-C, +1.54), and 2008 (AR7W-E, +2.08) (Figure 23). The coolest years occurred in 2007 (AR7W-W, -1.36), 2018 (AR7W-C, -1.48), and 2011 (AR7W-E, -1.36).

In 2024, AR7W-W exhibited the second highest temperature in the time series with an anomaly of +1.58, following two years of negative or near-normal temperature anomalies. Temperature in AR7W-C was slightly above normal (+0.27), a decline from 2023 which had a higher positive anomaly. In contrast, AR7W-E showed temperature slightly below normal (-0.12), continuing the negative anomaly trend that has been observed since 2011 (with the exception of 2016 and 2019).

Nutrients

All near-surface nutrient concentrations (i.e., 0–100 m, nitrate, phosphate, and silicate) exhibited inter-annual variations between 1997 and 2010, followed by three years (2011 to 2013) of near or below average nutrient levels for all regions, except for silicate (AR7W-W, 2011) and phosphate (AR7W-C, 2013) (Figure 24). From 2014 to 2018, all nutrients levels were above normal except for nitrate and phosphate in 2015 in AR7W-C. While no patterns are observed between nutrients and regions before 2011, all regions and nutrients anomalies were correlated between 2011 and 2019.

Since 2019, surface nutrients have shown negative trends in AR7W-W and AR7W-C. AR7W-E trends were similarly negative with the exception of 2022 nutrients and 2023 silicate. In 2024, surface nutrients exhibited negative anomalies in all regions, with record low anomalies of all nutrients in both AR7W-W and AR7W-C. Note that in 2024, AZOMP implemented filtration of nutrients water samples through a 0.2 μm mesh to reduce the impact of particulate nutrients on the measurements, which may explain some of the decreased concentrations observed in the scorecards.

Deep nutrients (>100 m) showed a different pattern than the surface nutrients in agreement with the hydrodynamics of the Labrador Sea and the surface-layer biological activity (Figure 25). Deep nutrients levels are less impacted by the timing of the mission as they are not consumed by phytoplankton and microbial remineralization at depth replenishes the nutrient pool. Filtration of water samples may not impact deep nutrients to the same degree as shallow nutrients, as there is less particulate material collected at depth. Deep nutrients anomalies showed large interannual variability between 1999 and 2018 (Figure 25). Interestingly, most of the record-high levels occurred in the first half of the time series, except for nitrate in AR7W-C (2018), and nitrate and silicate in AR7W-W, which occurred in 2015, a notable year given an unusual large bloom of *Phaeocystis spp.* (Devred et al., 2024). On the other hand, record-low levels of nutrients occurred after 2009. While no clear trend has emerged for the scorecards, since 2019 all deep nutrients have showed below-average levels, except for nitrate in AR7W-C in 2022 and AR7W-E in 2024, which were near normal. In 2024, deep nutrients exhibited mainly negative anomalies in all regions, with record low phosphate and silicate concentrations in AR7W-C. It is noteworthy that these below-average levels of nutrients that started in 2019 coincided with the trend for surface nutrients (Figures 24 and 25), which suggests a change in overall nutrient budget in the Labrador Sea ecosystem.

In situ chlorophyll-a concentration

In general, the AR7W-E region has high levels of integrated chl-a with a mean of 394 mg m^{-2} from 1999 to 2020 (Figure 26), and is dominated by nanophytoplankton with low concentrations of picophytoplankton. Conversely, AR7W-C is a region with low integrated chl-a (165 mg m^{-2}) and a low proportion of nanophytoplankton, with high concentrations of picophytoplankton. AR7W-W exhibits the lowest concentrations of integrated chl-a (122 mg m^{-2}) and micro and nano-phytoplankton dominates the phytoplankton assemblage, with low biomass of picophytoplankton. Upper ocean (< 100 m depth) phytoplankton sampled on the AR7W section in spring and early summer between 1999 and 2022 showed region-specific characteristics (Devred et al., 2024; Fragoso et al., 2016; Li and Harrison, 2014).

Integrated chl-a shows a low frequency variability with a given trend (above or below average) that remains for several years at a time. In that respect, the time series for AR7W-W and AR7W-C show two periods of lower-than-normal levels, from about 2001 to 2005 and from 2014 to 2019, while the remaining periods show above-normal values. Record-high levels of integrated chl-a occurred in 2022 in AR7W-W and in 2015 in AR7W-C. Both years corresponded to the very large blooms of *Phaeocystis spp.* (Devred et al., 2024). AR7W-E showed a different pattern than the two other regions, with lower than normal values between 2004 and 2008, followed by a period of large interannual variability (2009 to 2013, 2009 being the record high). Since 2014, integrated chl-a has been lower than average.

In 2024, integrated chl-a anomalies returned to below-normal in AR7W-W and AR7W-C after a two-year period of high positive anomalies. AR7W-E integrated chl-a remained below normal, continuing the trend observed since 2014 in this region.

Integrated chl-a levels do not necessarily reflect nutrients concentrations, which can be somewhat explained by the timing of the missions (Figure 2). For instance, in 2013, the mission sampled the transect at the peak of the bloom (as indicated by satellite ocean colour), resulting in high integrated chl-a and low nutrients, likely depleted by phytoplankton consumption. Conversely, in 2014, the mission sampled the AR7W before or at the start of the spring bloom, when chl-a concentration was low and nutrients levels high. Similarly, both 2022 and 2023 missions in AR7W-W and in AR7W-C occurred at the peak of the spring bloom (Figure 2), corresponding to high integrated chl-a values and low nutrients values, while the 2024 mission sampled these regions at the tail end of the bloom when chl-a concentrations were lower and nutrients depleted.

Phytoplankton Apparent Absorption Wavelength (PAAW)

PAAW is a measure of phytoplankton color and biomass. Higher values, indicated by orange in Figure 27, occur when the spectral shape of the phytoplankton absorption curve is flatter (Devred et al., 2022). A shift in anomaly patterns could indicate a shift in community structure, though it might be more the result of sample timing than a change in the properties of the ecosystem.

The mean PAAW wavelengths were similar in AR7W-W and AR7W-C (476 nm), and slightly higher in AR7W-E (479 nm). Up to 2007, PAAW anomalies were predominantly negative, but variability between lower and higher than normal PAAW started in 2008 with no clear pattern, unlike integrated chl-a. Since 2019 PAAW anomalies have been mainly positive, indicating a possible increase in phytoplankton biomass with a change of structure toward larger cells. In 2024, PAAW showed higher than normal anomalies except for AR7W-W. It's noteworthy that the general shift in PAAW since 2019 coincides with the low surface and deep nutrient trends.

Satellite-derived chlorophyll-a concentration and bloom metrics

Satellite-derived chl-a allows observation of the Labrador Sea all year long, but is limited by sea ice and cloud cover. The main advantage of the satellite is that information on phytoplankton biomass and spring bloom timing can be reported when sea-going missions have been cancelled or delayed. Here we report on the timing of the spring and fall blooms, and the annual and seasonal mean chl-a in the three regions of interest. Previous reports used data from the MODIS-Aqua sensor whereas this report uses the OC-CCI multi-sensor product, resulting in some minor differences in the climatological means that can be partially explained by the improvement in data coverage from OC-CCI.

The timing of the spring bloom peak is highly variable and depends on several factors, including the thermal stratification, the amount of nutrients, the light available for photosynthesis, and the grazing pressure. The spring bloom generally occurs first in AR7W-E (day of year (doy) 138 on average), then in AR7W-W (doy 157 on average) and shortly after in AR7W-C (doy 168 on average) (Figure 28).

AR7W-W spring bloom peak timing has typically been early since 2003, with the exception of 2004, 2007, 2009, and the second latest bloom on record in 2018. In contrast, AR7W-E bloom timing has been highly variable over the time series. AR7W-C has experienced periods of early or late blooms (late from 2000-2004, early from 2005-2015 with the exception of 2009 and 2011, late again from 2016-2021, and early since 2022). Note that in both 2015 and 2022, very large and unusual blooms of *Phaeocystis spp.* were observed (Devred et al., 2024). Since 2022, AR7W-E spring bloom peaks have been later than normal, while AR7W-W and AR7W-C blooms have been early, with 2024 showing record-early timing in AR7W-W (-1.96) and the second earliest timing in AR7W-C (-2.14).

A secondary bloom occurs in the fall, less intense than the spring one, triggered by the replenishment in nutrients of the surface-lit layer by storm-induced vertical mixing when light is still sufficient to stimulate phytoplankton productivity. The changes in fall bloom timing have followed different patterns than the spring bloom, with more variability in AR7W-W before 2015 but late blooms since then, and a record late bloom in 2024 (anomaly of +2.45). AR7W-C and AR7W-E fall bloom timings were highly variable up to 2021, after which they have been earlier than normal in AR7W-C and later than normal in AR7W-E.

Annual and spring chl-a average anomalies show correlations in all three regions, suggesting that the spring bloom drives the annual production. The mean annual and seasonal chl-a show high interannual variability, with a notable increase in the number of high positive chl-a anomalies in fall and winter in the past decade. In 2024, mean annual and spring chl-a were below normal in AR7W-W, near normal in AR7W-C, and above normal in AR7W-E. All other seasonal anomalies were above normal with the exception of fall chl-a in AR7W-W. Winter exhibited the highest anomaly on record in AR7W-E (+5.95) and the second highest in AR7W-C (+3.09).

Mesozooplankton

Note the mesozooplankton collection here only covers the time series up to the year 2023. Analysis of the samples from the 2024 mission is still ongoing.

C. finmarchicus copepods dominate the mesozooplankton biomass in AR7W-C, while they and their congeners *C. glacialis* and *C. hyperboreus* contribute about one third each of total biomass on the shelves (AR7W-W and AR7W-E) (Head et al., 2003). *C. finmarchicus* total abundance is greatly influenced by the abundance of young stage copepodites, which develop from laid eggs that have overwintered as pre-adults in the deep central basin and re-ascended in spring. The phytoplankton spring bloom provides the fuel required for egg-laying and the development of subsequent population, so that regional differences in spring bloom dynamics lead to differences in the timing of the development of *C. finmarchicus* populations. Since spring blooms are generally earlier and more intense in AR7W-E than in the other regions, *C. finmarchicus* abundance is generally higher in AR7W-E than in other regions of the Labrador Sea at the time of sampling (Figure 29).

In AR7W-W, 2011 had an exceptionally high abundance of *C. finmarchicus*, which remains unexplained (Figure 29). For the rest of the time series, abundances have been variable, with two higher-than-average values in 2001 and 2019 and a sustained period of relatively-low abundance occurring between 2004 and 2008. The high abundance in 2019 was mostly due to the large number of younger stages, which is reflected in the higher-than-average %PDI typical of a post-phytoplankton bloom sampling. In AR7W-C, development of the spring bloom and the relatively late development of *C. finmarchicus* result in higher abundance of *C. finmarchicus* in summer than in spring (Figure 29). Young stages were seldom very abundant, perhaps due to high mortality (Head et al., 2015) except for the summer of 1995, with an exceptionally higher total abundance year. There was no trend in spring total abundance for *C. finmarchicus* between 1997 and 2023. The high abundance in 2022 reflects the extension of the large *Phaeocystis* bloom favoring the growth of young copepodite stages as showed by a higher PDI anomaly. In AR7W-E, there was one exceptionally high *C. finmarchicus* abundance value in May 2006, the cause of which is unclear.

High climatological abundance of *C. glacialis* and *C. hyperboreus* in AR7W-W ($2x10^3$ and $4x10^3$ individuals per m^2, respectively) and AR7W-E ($1x10^3$ and $3x10^3$ individuals per m^2) compared to AR7W-C ($3x10^2$ and $1x10^3$ individuals per m^2) may result from the transport of individuals in the inflows, since neither species have a local source of overwintering population. The abundance of both species has generally shown considerable year-to-year variability, but with sustained periods of low abundance for *C. glacialis* on both shelves since 2014 with the exception of 2019 where abundance were higher or around the average in all regions. Sustained periods of high abundance for *C. hyperboreus* occurred in AR7W-E between 2009 and 2012 while low abundance occurred in AR7W-W between 2012 and 2018 (Figure 29).

Pseudocalanidae spp. have been generally more abundant than average in AR7W-C since 2008, whereas a general decreasing trend was observed in AR7W-W and AR7W-E between 2014 and 2018 (Figure 29). Since 2019, abundances in all 3 regions are either close to or higher than the average with the exception of AR7W-E in 2022, which remained below but close to normal conditions. The extent of a large bloom of the phytoplankton species *Phaeocystis* (Devred et al., 2024) beyond AR7W-E and into AR7W-C at that time of year may explain the large abundance of *Pseudocalanidae*. In contrast, *Oithonidae* remained persistently less abundant than average in AR7W-C since 2013, while the decrease in abundance on both shelves became more prevalent around 2014 (AR7W-W) and 2015 (AR7W-E) (Figure 29). In AR7W-W the *Oithona* abundance was significantly higher than average in 2022 and 2023 and close to the average in AR7W-E.

Up to 2013, *Euphausiid* showed large interannual variability in the three regions of interest (Figure 29). Between 2014 and 2019, *Euphausiid* abundance was consistently lower than average in all regions, except in AR7W-W in 2019 which was slightly higher than average. Abundance has been low to normal since 2022 in AR7W-E, high in AR7W-W with the second highest abundance on record in 2022, and high in 2022 and low in 2023 in AR7W-C. Amphipods, mostly represented here by *Parathemisto libellula*, showed lower-than-average abundances throughout the LS since 2016, following a decade-long period of higher interannual variability. In 2023, Amphipoda abundances reached record lows in AR7W-E and AR7W-C and the third lowest abundance on record in AR7W-W.

Summary

The Atlantic Zone Off-Shelf Monitoring Program (AZOMP) provides observations on ocean climate and plankton variability within the Labrador Sea and adjacent shelves affecting ecosystems of Atlantic Canada and the climate at both regional and global scales. In the Labrador Sea, surface heat losses in winter result in the formation of dense waters, which spread across the ocean, ventilating the deep layers, thus contributing to the global ocean-overturning circulation.

The winter (January to March) NAO index in 2024 was slightly below normal. In the central Labrador Sea, winter 2024 had the largest air temperature anomaly with 1.0 °C above normal, and 2024 summer had the smallest one with 0.3 °C above normal. The winter and spring SST anomalies in the central Labrador Sea (derived from the HadISST product) were close to normal, summer anomalies were below normal (-0.23 °C), and fall anomalies were above normal (0.24 °C). Sea ice extent and concentration anomalies in the winter of 2024 were generally negative for the Labrador shelf, but a notable positive anomaly of sea ice concentration persisted along the Greenland shelf throughout the winter months and interfered with sampling during the AZOMP mission that spring. In 2024, data retrieved from Argo profilers revealed that the temperature anomalies relative to the 2002-2020 reference period in the Labrador Sea for three layers (100-500 dbar, 500-1000 dbar, and 1000-2000 dbar) were mostly positive (warm), particularly in the northern and western areas, and the salinity anomalies were mostly negative (fresh), particularly in the two deep layers. Argo data showed that the temperature in 2023 and 2024 resembled the climatology, however the salinity in 2023 and 2024 was fresher in every month in these two years. The analysis of the AR7W temperature and salinity data from CTD profiles collected during the 2024 mission indicated that the winter convection in the Labrador Sea reached about 700 to 900 m.

CFC-12 concentration experienced a decline from 2019-2020, but the lack of sampling in 2021 and instrument malfunction from 2022 to 2023 could not confirm the continuing downward trend. SF_6 concentration continued increasing linearly at a rate of 0.08 fmol kg^{-1} y^{-1}, but the 2023 data requires additional quality control before reporting. TIC concentrations from the NV-LSW in the central Labrador Sea have continued to increase as in previous years, though at a slower rate (0.84 µmol kg^{-1} y^{-1} from 1996 to 2023, but only 0.51 µmol kg^{-1} y^{-1} from 2019 to the 2022 peak). The increase resulted in pH levels continuing their declining trend (0.003 pH units per year).

Average surface layer temperature derived from CTD measurements taken in conjunction with water samples in the AR7W-C has fluctuated between anomalously low (2022) and high (2019, 2023) values, returning to near-normal but slightly positive in 2024. The shelves (AR7W-W and AR7W-E) have been near-normal except for the cold period in 2022, but 2024 saw a large positive anomaly on the Labrador Shelf.

Strong inter-annual variability was observed in surface nutrient concentrations, which are consistent among regions. From 2014 to 2018, there were positive anomalies in all regions, with the exception of nitrate and phosphate in AR7W-C in 2015. Negative anomalies have been observed since 2019 in AR7W-W and AR7W-C for all nutrients except for silicate in AR7W-C in 2022, which was normal. In contrast in AR7W-E, silicate concentrations rebounded in 2022-2023, and nitrate and phosphate anomalies were positive in 2022 and negative again in 2023 and 2024. Deep nutrient concentrations also experienced high interannual variability, but have been negative across all regions since 2019, including 2024 except for the AR7W-E region. Chl-a concentrations have followed an inverse pattern to surface nutrients, with lower than normal concentrations for all three regions since 2014, except for the anomalously high concentration in 2015 in AR7W-C, and high concentrations in AR7W-W and AR7W-C in 2022-2023. In 2024 chl-a anomalies were negative for all three regions. The high chl-a anomalies and below-normal nitrate and phosphate anomalies in AR7W-C in 2015 and 2022 were associated with an intense phytoplankton bloom consisting mainly of *Phaeocystis spp.* which was identified from shipboard observations. Recurrent earlier sampling dates from year to year may partly explain the observed negative anomalies in chl-a concentrations, since sampling may have occurred before the start of the spring bloom. Ocean color metrics (spring peak timing, fall bloom initiation, and annual and seasonal averages) showed no obvious trends over time or correlations between regions, though correlations between spring and annual averages suggest the spring bloom is the biggest contributor to overall annual biomass production. In 2024, the spring bloom was early in AR7W-W and AR7W-C and late in AR7W-E, while the fall bloom was late on the shelves (i.e. AR7W-W and E) and early in the central basin. Mean annual chl-a was above normal in AR7W-C and AR7W-E but lower than normal in AR7W-W. At the seasonal level, mean chl-a was above normal in all regions except in spring and fall in AR7W-W and spring in AR7W-C.

With the exception of *Pseudocalanus spp.* and Amphipoda, which exhibited high and low abundance anomalies respectively, other taxa do not show clear trends during the 2019-2023 period. In AR7W-W and AR7W-C, the higher than average %PDI in *C. finmarchicus* may have been linked in part to their seasonal life-cycle where the populations were consistently more advanced in development than the average. The AR7W-E region, generally sampled later in the bloom season, showed a population growth rate which was slower or close to the average.

Acknowledgements

The authors thank the sea-going staff of the Bedford Institute of Oceanography and the officers and crew of the Canadian Coast Guard ship Captain Jacques Cartier. Jay Barthelotte, Robert Benjamin, Jay Bugden, Diana Cardoso, Raven Elwell, Melissa Falkner, Jennifer Field, Yuri Geshelin, Jason Green, Adam Hartling, Flo Hum, Jeff Jackson, Meng Ji, Matt Lawson, Claire McIntyre, Tim Perry, Peter Thamer, Mike Vining, Kristen Wilson, and Jinshan Xu contributed to sample collection, sample analysis, data analysis, data management, and data sharing.

References

Astthorsson, O. S., and Gislason, A. (2003). Seasonal variations in abundance, development and vertical distribution of Calanus finmarchicus, C. hyperboreus and C. glacialis in the East Icelandic Current. *Journal of Plankton Research*, *25(7)*, 843–854. **https://doi.org/10.1093/plankt/25.7.843**

Azetsu-Scott, K., Clarke, A., Falkner, K., Hamilton, J., Jones, E. P., Lee, C., Petrie, B., Prinsenberg, S., Starr, M., and Yeats, P. (2010). Calcium carbonate saturation states in the waters of the Canadian Arctic Archipelago and the Labrador Sea. *Journal of Geophysical Research*, *115*(C11021). https://doi.org/**https://doi.org/10.1029/2009JC005917**

Azetsu-Scott, K., Jones, E. P., Yashayaev, I., and Gershey, R. M. (2003). Time series study of CFC concentrations in the Labrador Sea during deep and shallow convection regimes (1991–2000). *Journal of Geophysical Research: Oceans*, *108*(C11). https://doi.org/**https://doi.org/10.1029/2002JC001317**

Barnston, A. G., and Livezey, R. E. (1987). Classification, seasonality and persistence of low-frequency atmospheric circulation patterns. *Monthly Weather Review*, *115*(6), 1083–1126. **https://doi.org/10.1175/1520-0493(1987)115<1083:CSAPOL>2.0.CO;2**

Becker, S., Aoyama, M., Woodward, E. M. S., Bakker, K., Coverly, S., Mahaffey, C., and Tanhua, T. (2020). GO-SHIP repeat hydrography nutrient manual: The precise and accurate determination of dissolved inorganic nutrients in seawater, using continuous flow analysis methods. *Frontiers in Marine Science*, *7*, 581790. **https://doi.org/10.3389/fmars.2020.581790**

Bélanger, S., Ehn, J. K., and Babin, M. (2007). Impact of sea ice on the retrieval of water-leaving reflectance, chlorophyll a concentration and inherent optical properties from satellite ocean color data. *Remote Sensing Env.*, *111*(1), 51–68. **https://doi.org/10.1016/j.rse.2007.03.013**

Caldeira, K., and Wickett, M. E. (2003). Anthropogenic carbon and ocean pH. *Nature*, *425*, 365. **https://doi.org/10.1038/425365a**

Cavalieri, D., Parkinson, C., Gloersen, P., and Zwally, H. (1996). *Sea ice concentrations from nimbus-7 SMMR and DMSP SSM/i-SSMIS passive microwave data, version 1*. NASA National Snow; Ice Data Center Distributed Active Archive Center. **https://doi.org/10.5067/8GQ8LZQVL0VL**

Clay, S., Layton, C., and Devred, E. (2021). *PhytoFit: First release (v1.0.0)*. https://doi.org/**https://doi.org/10.5281/zenodo.4770754**

Clay, S., Peña, A., DeTracey, B., and Devred, E. (2019). Evaluation of satellite-based algorithms to retrieve Chlorophyll-a concentration in the Canadian Atlantic and Pacific oceans. *Remote Sens.*, *11*(22). **https://doi.org/10.3390/rs11222609**

Devred, E., Perry, T., and Massicotte, P. (2022). Seasonal and decadal variations in absorption properties of phytoplankton and non-algal particulate matter in three oceanic regimes of the Northwest Atlantic. *Frontiers in Marine Science*, *Volume 9 - 2022*. **https://doi.org/10.3389/fmars.2022.932184**

Devred, E., Wilson, K. L., Perry, T., Hardy, M., Brosnahan, M., and Ringuette, M. (2024). *Identification and validation of phytoplankton taxonomic assemblages derived from pigment signatures using samples collected in the Labrador Sea from 2014 to 2022* (Can. Tech. Rep. Fish. Aquat. Sci. 3596: Viii + 55 p No. 3596). **https://www.researchgate.net/publication/379220093_Identification_and_validation_of_phytoplankton_taxonomic_assemblages_derived_from_pigment_signatures_using_samples_collected_in_the_Labrador_Sea_from_2014_to_2022_Canadian_Technical_Report_of_Fisherie**

Dickson, A. G., Sabine, C. L., and Christian, J. R. (Eds.). (2007). Guide to best practices for ocean CO2 measurements. *PICES Special Publication 3*. **https://data.ess-dive.lbl.gov/portals/CDIAC**

Elzhov, T. V., Mullen, K. M., Spiess, A.-N., and Bolker, B. (2023). *Minpack.lm: R interface to the levenberg-marquardt nonlinear least-squares algorithm found in MINPACK, plus support for bounds*. **https://CRAN.R-project.org/package=minpack.lm**

Feely, R. A., Sabine, C. L., Lee, K., Berelson, W., Kleypas, J., Fabry, V. J., and Millero, F. J. (2004). Impact of anthropogenic CO2 on the CaCO3 system in the oceans. *Science*, *305*(5682), 362–366. **https://doi.org/10.1126/science.1097329**

Fetterer, F., Knowles K., Meier W., Savoie M., and A., W. (2017). *Sea ice index, version 3*. NSIDC. **https://doi.org/10.7265/N5K072F8**

Fragoso, G. M., Poulton, A. J., Yashayaev, I. M., Head, E. J. H., Stinchcombe, M. C., and Purdie, D. A. (2016). Biogeographical patterns and environmental controls of phytoplankton communities from contrasting hydrographical zones of the Labrador Sea. *Progress in Oceanography*, *141*, 212–226. **https://doi.org/10.1016/j.pocean.2015.12.007**

Haine, T. W. N., and Hall, T. M. (2002). A generalized transport theory: Water-mass composition and age. *Journal of Physical Oceanography*, *32*(6), 1932–1946. **https://doi.org/10.1175/1520-0485(2002)032<1932:AGTTWM>2.0.CO;2**

Hall, T. M., Haine, T. W. N., and Waugh, D. W. (2002). Inferring the concentration of anthropogenic carbon in the ocean from tracers. *Global Biogeochemical Cycles*, *16*(4), 1131. https://doi.org/**https://doi.org/10.1029/2001GB001835**

Harrison, W. G., and Li, W. K. W. (2008). Phytoplankton growth and regulation in the Labrador Sea: Light and nutrient limitation. *Journal of Northwest Atlantic Fishery Science*, *39*, 71–82. **https://doi.org/10.2960/J.v39.m592**

Hauser, T., Demirov, E., Zhu, J., and Yashayaev, I. (2015). North atlantic atmospheric and ocean inter-annual variability over the past fifty years - dominant patterns and decadal shifts. *Progress in Oceanography*, *132*, 197–219. https://doi.org/**https://doi.org/10.1016/j.pocean.2014.10.008**

Head, E. J. H., Azetsu-Scott, K., Harrison, G., Hendry, R., Li, W., Yashayaev, I., and Yeats, P. (2008). *Changes in environmental conditions and the population dynamics of Calanus finmarchicus in the Labrador Sea (1990-2006)*. **https://doi.org/10.17895/ices.pub.25244281.v1**

Head, E. J. H., Gentleman, W. C., and Ringuette, M. (2015). Variability of mortality rates for Calanus finmarchicus early life stages in the Labrador Sea and the significance of egg viability. *Journal of Plankton Research*, *37*(6), 1149–1165. **https://doi.org/10.1093/plankt/fbv080**

Head, E. J. H., Harris, L. R., and Yashayaev, I. (2003). Distributions of Calanus spp. And other mesozooplankton in the Labrador Sea in relation to hydrography in spring and summer (1995–2000). *Progress In Oceanography*, *59*(1), 1–30. **https://doi.org/10.1016/S0079-6611(03)00111-3**

Holm-Hansen, O., Lorenzen, C. J., Holmes, R. W., and Strickland, J. D. H. (1965). Fluorometric determination of chlorophyll. *ICES Journal of Marine Science*, *30*(1), 3–15.

Hood, E. M., Sabine, C. L., and Sloyan, B. M. (Eds.). (2010). *The GO-SHIP repeat hydrography manual: A collection of expert reports and guidelines, version 1* [(IOCCP Report 14), (ICPO Publication Series 134)]. **https://www.go-ship.org/HydroMan.html**

Hurrell, J. W. (1995). Decadal trends in the North Atlantic Oscillation: Regional temperatures and precipitation. *Science (New York, N.Y.)*, *269*, 676–679. **https://doi.org/10.1126/science.269.5224.676**

Johnson, K. M., Sieburth, J.McN., Williams, P. J.leB., and Brändström, L. (1987). Coulometric total carbon dioxide analysis for marine studies: Automation and calibration. *Marine Chemistry*, *21*(2), 117–133. https://doi.org/**https://doi.org/10.1016/0304-4203(87)90033-8**

Jones, P. D., and Hulme, M. (1996). Calculating regional climatic time series for temperature and precipitation: Methods and illustrations. *International Journal of Climatology*, *16*(4), 361–377. https://doi.org/**https://doi.org/10.1002/(SICI)1097-0088(199604)16:4<361::AID-JOC53>3.0.CO;2-F**

Kalnay, E., Kanamitsu, M., Kistler, R., Collins, W., Deaven, D., Gandin, L., Iredell, M., Saha, S., White, G., Woollen, J., Zhu, Y., Chelliah, M., Ebisuzaki, W., Higgins, W., Janowiak, J., Mo, K. C., Ropelewski, C., Wang, J., Leetmaa, A., … Joseph, D. (1996). The NCEP/NCAR 40-year reanalysis project. *Bulletin of the American Meteorological Society*, *77*(3), 437–472. **https://doi.org/10.1175/1520-0477(1996)077<0437:TNYRP>2.0.CO;2**

Kérouel, R., and Aminot, A. (1997). Fluorometric determination of ammonia in sea and estuarine waters by direct segmented flow analysis. *Marine Chemistry*, *57*(3), 265–275. https://doi.org/**https://doi.org/10.1016/S0304-4203(97)00040-6**

Layton, C., Devred, E., and Detracey, B. (2022). *A comparison of phytoplankton spring bloom fitting methods using MODIS satellite-derived chlorophyll-a concentration for the Maritimes region* (Can. Tech. Rep. Hydrogr. Ocean Sci. 340: Vii + 22p No. 340). **https://publications.gc.ca/collections/collection_2022/mpo-dfo/Fs97-18-340-eng.pdf**

Li, W. K. W., and Harrison, W. G. (2014). *The state of phytoplankton and bacterioplankton in the Labrador Sea: Atlantic Zone Off-Shelf Monitoring Program 1994–2013* (Can. Tech. Rep. Hydrogr. Ocean. Sci. 302: Xviii + 181p No. 302). **https://waves-vagues.dfo-mpo.gc.ca/Library/354345.pdf**

Loder, J. W., and Wang, Z. (2015). Trends and variability of sea surface temperature in the Northwest Atlantic from three historical gridded datasets. *Atmosphere-Ocean*, *53*(5), 510–528. **https://doi.org/10.1080/07055900.2015.1071237**

Lozier, M. S., Li, F., Bacon, S., Bahr, F., Bower, A., Cunningham, S., De Jong, M. F., Steur, de, L., Deyoung, B., Fischer, J., Gary, S., Greenan, B., Holliday, N., Houk, A., Houpert, L., Inall, M., Johns, W., Johnson, H., Johnson, C., and Zhao, J. (2019). A sea change in our view of overturning in the subpolar North Atlantic. *Science*, *363*(6426), 516–521. **https://doi.org/10.1126/science.aau6592**

Lueker, T. J., Dickson, A. G., and Keeling, C. D. (2000). Ocean pCO2 calculated from dissolved inorganic carbon, alkalinity, and equations for K1 and K2: Validation based on laboratory measurements of CO2 in gas and seawater at equilibrium. *Marine Chemistry*, *70*(1), 105–119. https://doi.org/**https://doi.org/10.1016/S0304-4203(00)00022-0**

Maze, G., and Balem, K. (2020). Argopy: A python library for argo ocean data analysis. *Journal of Open Source Software*, *5*(53), 2425. **https://doi.org/10.21105/joss.02425**

Mitchell, M. R., Harrison, G., Pauley, K., Gagné, A., Maillet, G., and Strain, P. (2002). Atlantic Zonal Monitoring Program sampling protocol. In *Can. Tech. Rep. Hydrogr. Ocean. Sci. 223: iv + 23p* (Vol. 223). **https://waves-vagues.dfo-mpo.gc.ca/Library/265754.pdf**

Neeley, A., Mannino, A., Boss, E., D'Sa, E., Freeman, S., Fry, E., Mueller, J., Pegau, W., Reynolds, R., Roesler, C., Röttgers, R., Stramski, D., Twardowski, M., Ronald, J., and Zaneveld, V. (2018). *IOCCG Protocol Series ocean optics & biogeochemistry protocols for satellite ocean colour sensor validation, volume 1: Inherent optical property measurements and protocols: Absorption coefficient (v1.0)*. **https://doi.org/10.25607/OBP-119**

O'Reilly, J. E., Maritorena, S., Mitchell, B. G., Siegel, D. A., Carder, K. L., Garver, S. A., Kahru, M., and McClain, C. (1998). Ocean color chlorophyll algorithm for SeaWiFS. *J. Geophys. Res.*, *103*, 937–953. **https://doi.org/10.1029/98JC02160**

Patel, R. (2025). *To compute Mixed Layer Depth based on subjective method*. MATLAB Central File Exchange. **https://www.mathworks.com/matlabcentral/fileexchange/53370-to-compute-mixed-layer-depth-based-on-subjective-method**

Platt, T., and Jassby, A. D. (1976). The relationship between photosynthesis and light for natural assemblages of coastal marine phytoplankton. *Journal of Phycology*, *12*, 421–430. **https://onlinelibrary.wiley.com/doi/epdf/10.1111/j.1529-8817.1976.tb02866.x**

Punshon, S., Azetsu-Scott, K., Sherwood, O., and Edinger, E. N. (2019). Bottom water methane sources along the high latitude eastern Canadian continental shelf and their effects on the marine carbonate system. *Marine Chemistry*, *212*, 83–95. https://doi.org/**https://doi.org/10.1016/j.marchem.2019.04.004**

Punshon, S., Childs, D., and Azetsu-Scott, K. (2016). *A purge-and-trap gas chromatographic method for shipboard determination of the transient tracers sulphur hexafluoride and dichlorodifluoromethane in seawater and in air* [Can. Tech. Rep. Hydrogr. Ocean Sci. 309: vii + 21p].

R Core Team. (2022). *R: A language and environment for statistical computing*. R Foundation for Statistical Computing. **https://www.R-project.org/**

Raimondi, L., Matthews, J. B. R., Atamanchuk, D., Azetsu-Scott, K., and Wallace, D. W. R. (2019). The internal consistency of the marine carbon dioxide system for high latitude shipboard and in situ monitoring. *Marine Chemistry*, *213*, 49–70. https://doi.org/**https://doi.org/10.1016/j.marchem.2019.03.001**

Raimondi, L., Tanhua, T., Azetsu-Scott, K., Yashayaev, I., and Wallace, D. W. R. (2021). A 30-year time series of transient tracer-based estimates of anthropogenic carbon in the central Labrador Sea. *Journal of Geophysical Research: Oceans*, *126*(5), e2020JC017092. https://doi.org/**https://doi.org/10.1029/2020JC017092**

Rayner, N. A., Parker, D. E., Horton, E. B., Folland, C. K., Alexander, L. V., Rowell, D. P., Kent, E. C., and Kaplan, A. (2003). Global analyses of sea surface temperature, sea ice, and night marine air temperature since the late nineteenth century. *Journal of Geophysical Research: Atmospheres*, *108*(D14). https://doi.org/**https://doi.org/10.1029/2002JD002670**

Sabine, C. L., Feely, R. A., Gruber, N., Key, R. M., Lee, K., Bullister, J. L., Wanninkhof, R., Wong, C. S., Wallace, D. W. R., Tilbrook, B., Millero, F. J., Peng, T.-H., Kozyr, A., Ono, T., and Rios, A. F. (2004). The oceanic sink for anthropogenic CO2. *Science*, *305*(5682), 367–371. **https://doi.org/10.1126/science.1097403**

Schiller-Weiss, I., Martin, T., and Schwarzkopf, F. U. (2024). Emerging influence of enhanced greenland melting on boundary currents and deep convection regimes in the labrador and irminger seas. *Geophysical Research Letters*, *51*(9), e2024GL109022. https://doi.org/**https://doi.org/10.1029/2024GL109022**

Stramski, D., Reynolds, R., Kaczmarek, S., Uitz, J., and Zheng, G. (2015). Correction of pathlength amplification in the filter-pad technique for measurements of particulate absorption coefficient in the visible spectral region. *Applied Optics*, *54*, 6763–6782. **https://doi.org/10.1364/AO.54.006763**

Visbeck, M. H., Hurrell, J. W., Polvani, L., and Cullen, H. M. (2001). The North Atlantic Oscillation: Past, present, and future. *Proceedings of the National Academy of Sciences*, *98*(23), 12876–12877. **https://doi.org/10.1073/pnas.231391598**

Wang, Z., Brickman, D., and Greenan, B. J. W. (2019). Characteristic evolution of the Atlantic Meridional Overturning Circulation from 1990 to 2015: An eddy-resolving ocean model study. *Deep Sea Research Part I: Oceanographic Research Papers*, *149*, 103056. https://doi.org/**https://doi.org/10.1016/j.dsr.2019.06.002**

Wang, Z., Brickman, D., Greenan, B. J. W., and Yashayaev, I. (2016). An abrupt shift in the Labrador Current System in relation to winter NAO events. *Journal of Geophysical Research: Oceans*, *121*(7), 5338–5349. **https://doi.org/10.1002/2016JC011721**

Wang, Z., Yang, J., Johnson, C., and DeTracey, B. (2022). Changes in deep ocean contribute to a “see-sawing” Gulf Stream path. *Geophysical Research Letters*, *49*(21), e2022GL100937. https://doi.org/**https://doi.org/10.1029/2022GL100937**

Wang, Z., Yashayaev, I., and Greenan, B. (2015). Seasonality of the inshore labrador current over the newfoundland shelf. *Continental Shelf Research*, *100*, 1–10. https://doi.org/**https://doi.org/10.1016/j.csr.2015.03.010**

Welschmeyer, N. A. (1994). Fluorometric analysis of chlorophyll a in the presence of chlorophyll b and pheopigments. *Limnology and Oceanography*, *39*(8), 1985–1992. https://doi.org/**https://doi.org/10.4319/lo.1994.39.8.1985**

Wong, A. P., Wijffels, S. E., Riser, S. C., Pouliquen, S., Hosoda, S., Roemmich, D., Gilson, J., Johnson, G. C., Martini, K., Murphy, D. J., and al., et. (2020). Argo data 1999-2019: Two million temperature-salinity profiles and subsurface velocity observations from a global array of profiling floats. *Frontiers in Marine Science*, *7*. **https://doi.org/10.3389/fmars.2020.00700**

Yashayaev, I. (2007). Hydrographic changes in the Labrador Sea, 1960–2005. *Progress in Oceanography*, *73*(3), 242–276. https://doi.org/**https://doi.org/10.1016/j.pocean.2007.04.015**

Yashayaev, I. (2024). Intensification and shutdown of deep convection in the Labrador Sea were caused by changes in atmospheric and freshwater dynamics. *Communications Earth & Environment*, *5*. **https://doi.org/10.1038/s43247-024-01296-9**

Yashayaev, I., and Loder, J. W. (2009). Enhanced production of Labrador Sea Water in 2008. *Geophys. Res. Lett.*, *36*(1), L01606. **https://doi.org/10.1029/2008GL036162**

Yashayaev, I., and Loder, J. W. (2016). Recurrent replenishment of labrador sea water and associated decadal-scale variability. *Journal of Geophysical Research: Oceans*, *121*(11), 8095–8114. https://doi.org/**https://doi.org/10.1002/2016JC012046**

Yashayaev, I., and Loder, J. W. (2017). Further intensification of deep convection in the Labrador Sea in 2016. *Geophysical Research Letters*, *44*(3), 1429–1438. https://doi.org/**https://doi.org/10.1002/2016GL071668**

Yashayaev, I., Peterson, I., and Wang, Z. (2021). *Meteorological, sea ice and physical oceanographic conditions in the Labrador Sea during 2018* (DFO Can. Sci. Advis. Sec. Res. Doc. 2021/042. Iv + 26 p No. 42). **https://waves-vagues.dfo-mpo.gc.ca/library-bibliotheque/40974698.pdf**

Yebra, L., Harris, R. P., Head, E. J. H., Yashayaev, I., Harris, L. R., and Hirst, A. G. (2009). Mesoscale physical variability affects zooplankton production in the Labrador Sea. *Deep Sea Research Part I: Oceanographic Research Papers*, *56*(5), 703–715. **https://doi.org/10.1016/j.dsr.2008.11.008**

Yentsch, C. S., and Menzel, D. W. (1963). A method for the determination of phytoplankton chlorophyll and phaeophytin by fluorescence. *Deep Sea Research*, *10*(3), 221–231. **https://doi.org/10.1016/0011-7471(63)90358-9**

Tables

Table 1. Links to data sources used in this report.

Data	Link	Date accessed
Winter NAO	psl.noaa.gov/data/climateindices	18 May 2025
Air temperature	ftp.cdc.noaa.gov	18 May 2025
SST (HadISST)	metoffice.gov.uk/hadobs/hadisst/data/ download.html	18 May 2025
Sea Ice	nsidc.org/data/g02135/versions/3	18 May 2025
Argo floats	argo.ucsd.edu	18 May 2025
Tracers, TIC, and pH	ncei.noaa.gov/products/ ocean-carbon-acidification-data-system	18 May 2025
Satellite ocean colour info	climate.esa.int/en/projects/ocean-colour	18 May 2025
Satellite ocean colour data	oceancolour.org	18 May 2025
Satellite bloom metrics	github.com/BIO-RSG/PhytoFit/tree/master/ verified_fits	18 May 2025
PhytoFit	cioosatlantic.ca/phytofit	18 May 2025

Figures

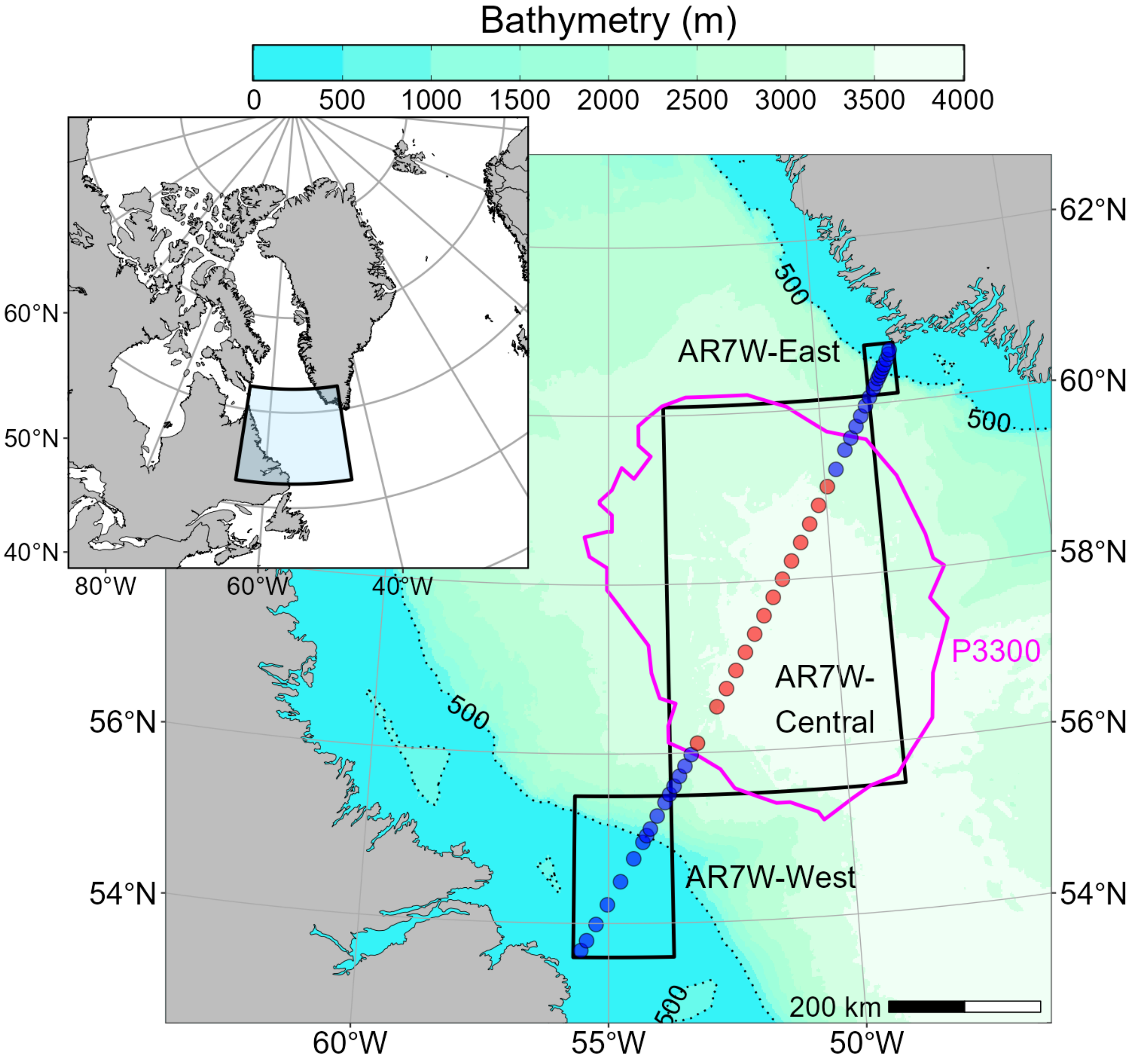

Figure 1. AR7W transect within the Labrador Sea. Blue and red dots represent the location of the core stations. Red stations are used in the calculation of annual averages for TIC, pH, and tracers for the NV-LSW from 150-500 m depth. Boxes correspond to the regions where satellite chl-a concentration is extracted (i.e., AR7W-West, AR7W-Central, and AR7W-East). Magenta polygon (P3300) indicates the area used in the physical data analysis (i.e. the area within 150 km of the AR7W line where bathymetry exceeds 3300 m). Dotted black lines correspond to the 500 m isobath.

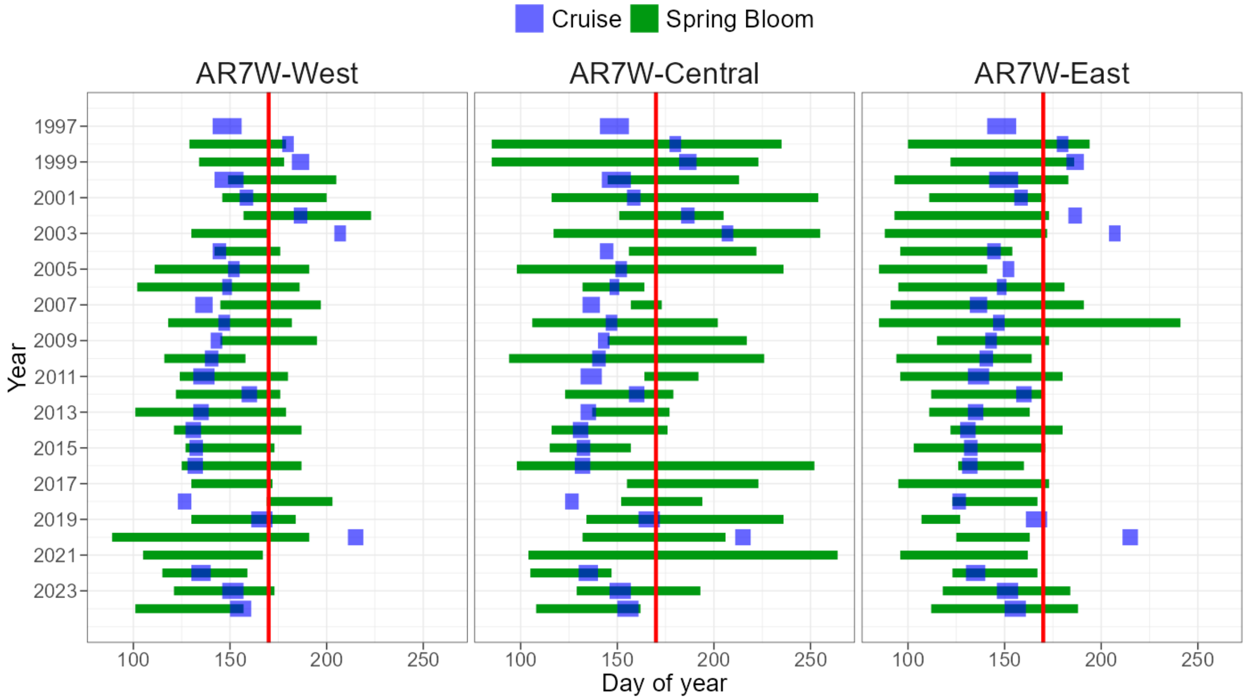

Figure 2. Blue rectangles represent the sampling period (actual occupation of AR7W line) and green rectangles correspond to the duration of the spring bloom within each region as derived from satellite ocean colour for AR7W-West (left), AR7W-Central (middle), and AR7W-East (right). Dates are reported in day of year. Missions in 2019 and 2020 were onboard CCGS Amundsen in late-June and August respectively. The COVID pandemic prevented the execution of the mission in spring 2020. Lack of vessel availability lead to the absence of a mission in 2021. Vertical red line (day of year 170) represents our cutoff date separating early and late missions.

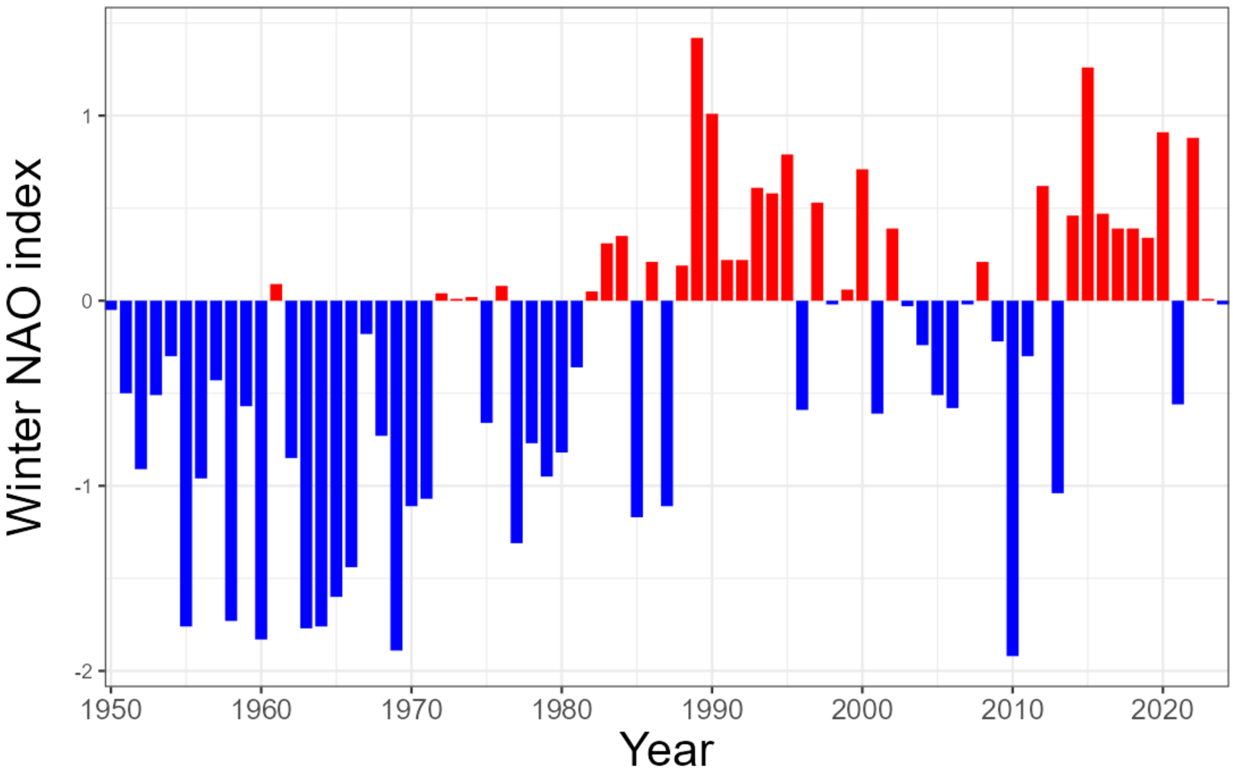

Figure 3. Anomalies of the winter (January to March) North Atlantic Oscillation (NAO) index, relative to the 2001-2020 mean.

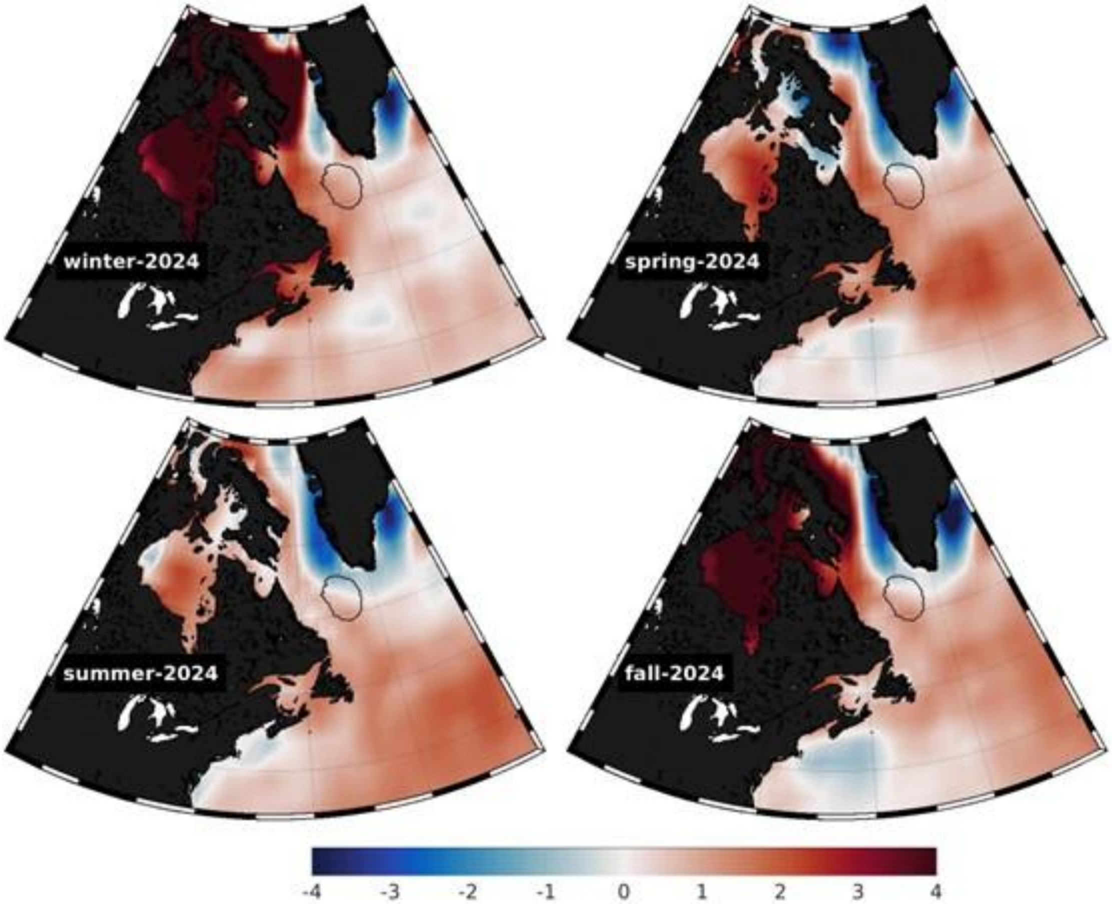

Figure 4. Surface air temperature anomaly for winter (Jan-Mar), spring (Apr-Jun), summer (Jul-Sep), and fall (Oct-Dec) periods in 2024 as derived from NCEP/NCAR reanalysis. The black polygon represents the area defined as the central Labrador Sea for this report.

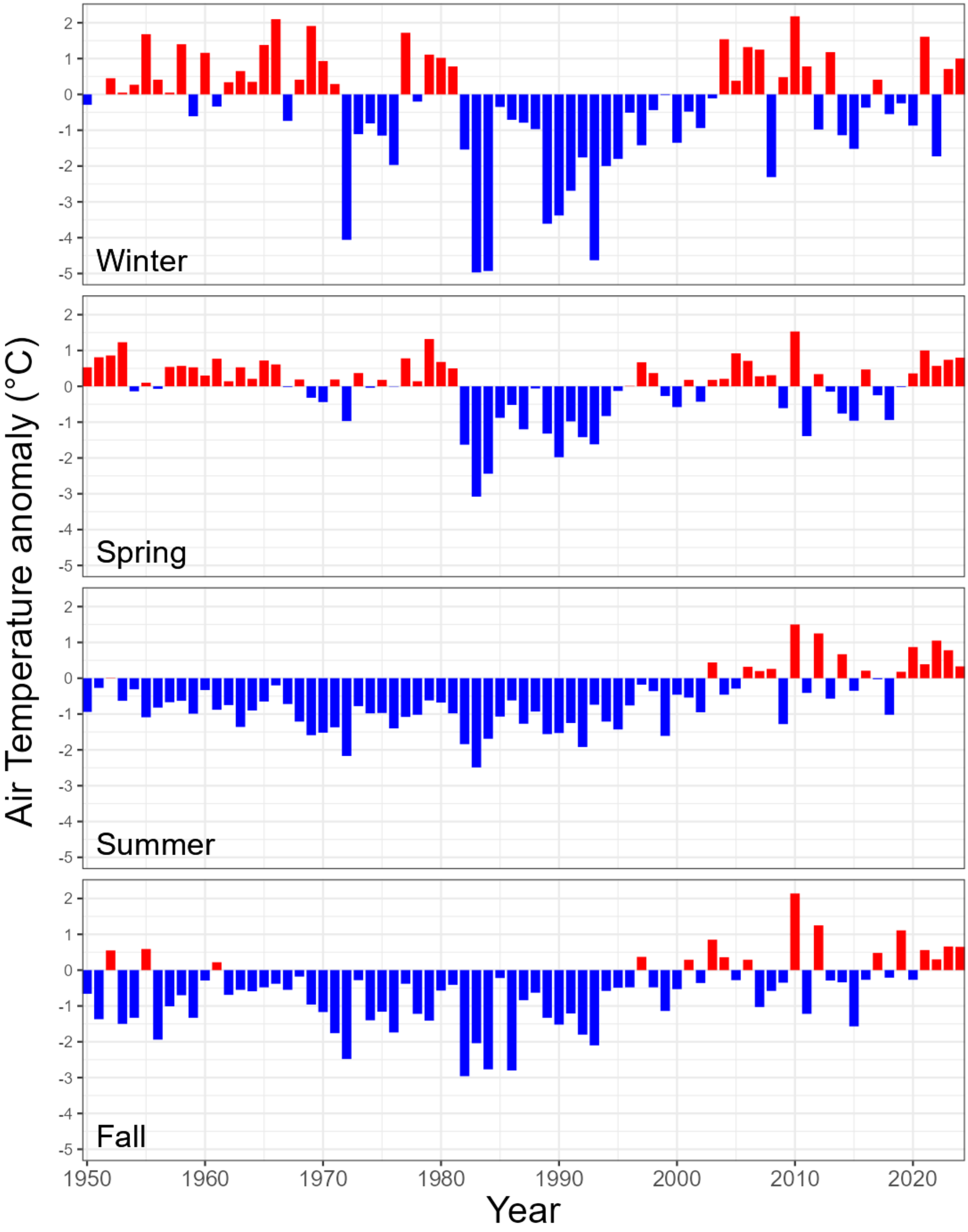

Figure 5. Anomalies of winter (Jan-Mar), spring (Apr-Jun), summer (Jul-Sep), and fall (Oct-Dec) air temperature in the central Labrador Sea, relative to the 2001-2020 mean.

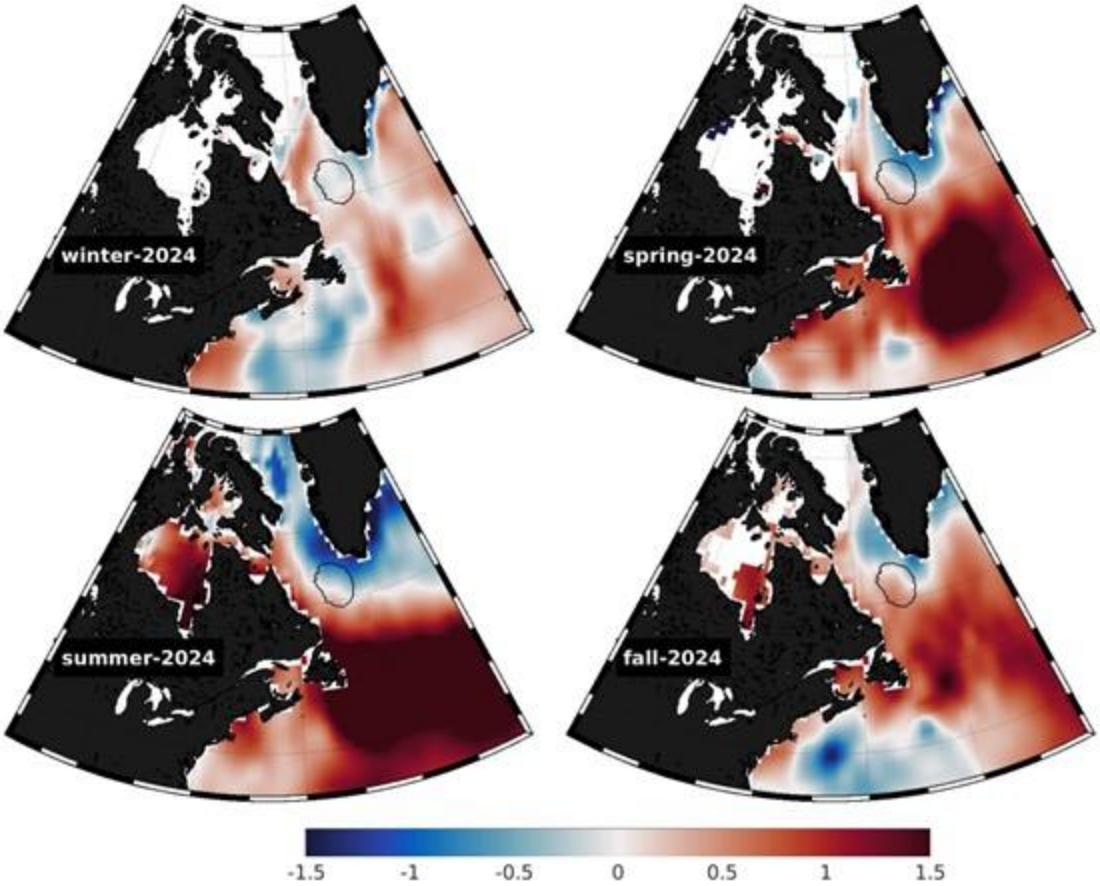

Figure 6. Sea surface temperature anomaly for winter (Jan-Mar), spring (Apr-Jun), summer (Jul-Sep), and fall (Oct-Dec) periods in 2024 as derived from HadISST. The black polygon represents the area defined as the central Labrador Sea for this report.

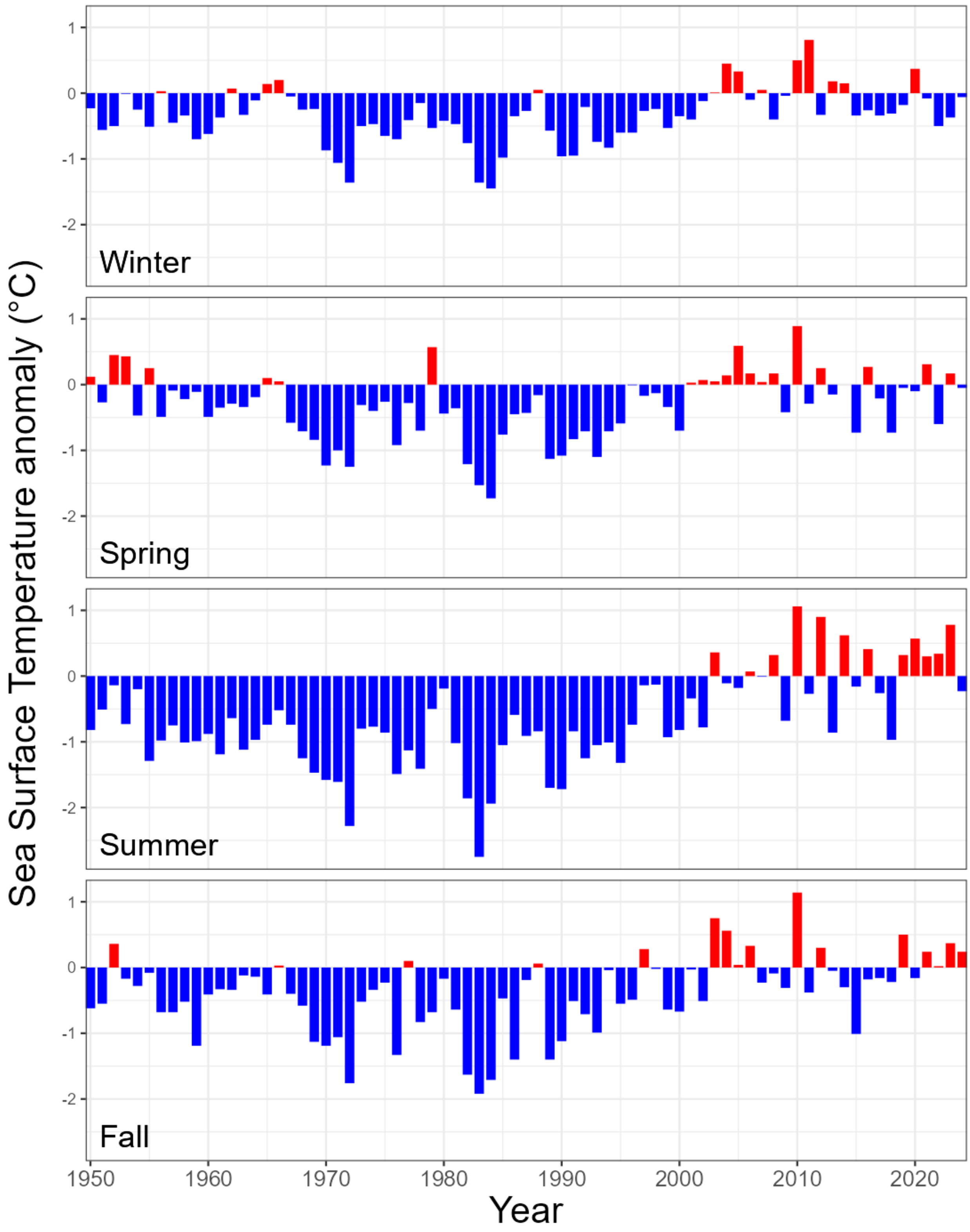

Figure 7. Anomalies of winter (Jan-Mar), spring (Apr-Jun), summer (Jul-Sep), and fall (Oct-Dec) sea surface temperature in the central Labrador Sea, relative to the 2001-2020 mean.

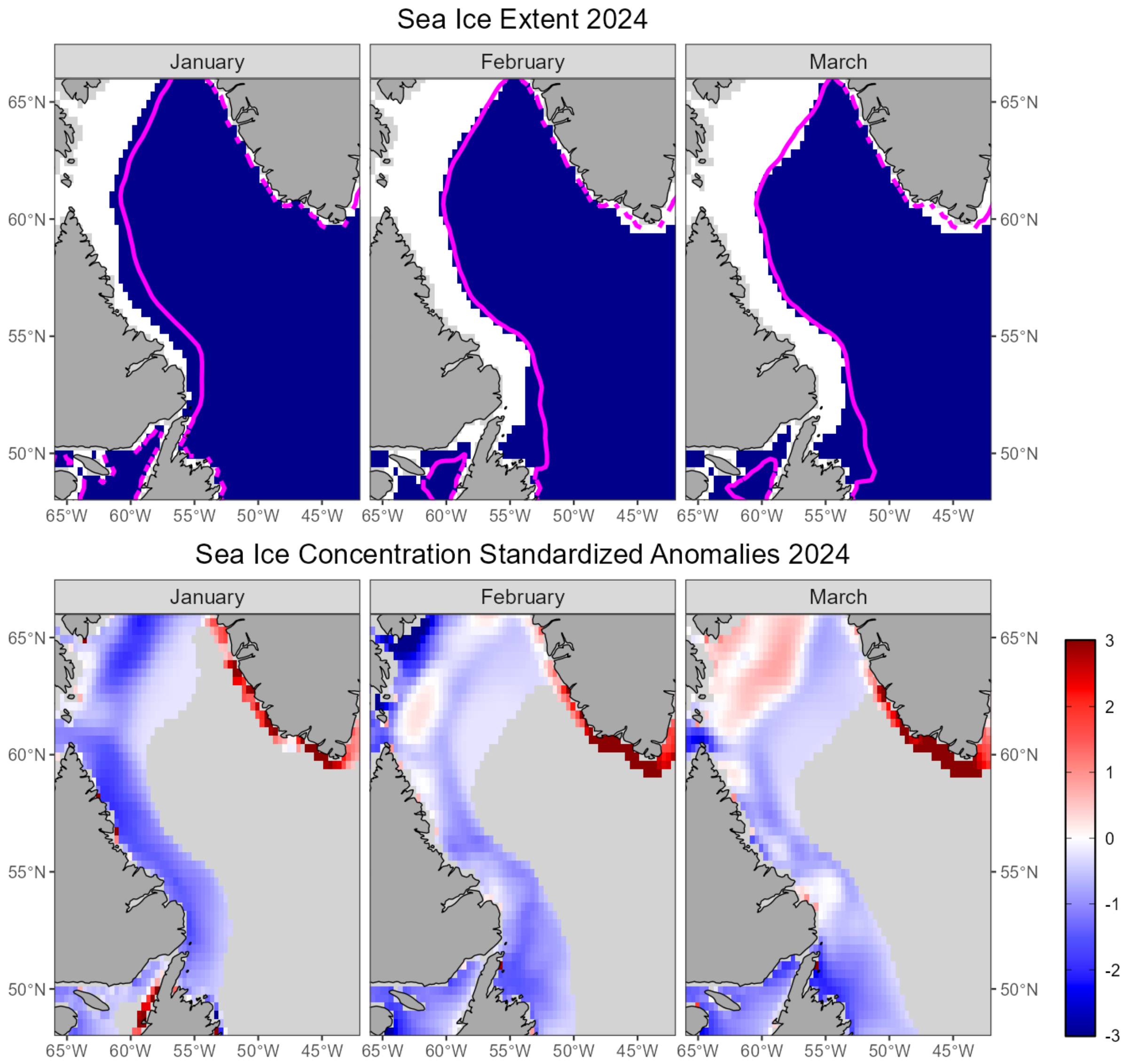

Figure 8. Top row: Sea ice extent for January to March 2024 (white pixels indicate sea ice concentration >=15%, blue pixels have low ice concentration or no ice, and light grey pixels have no data). The magenta line indicates the climatological median sea ice extent. Bottom row: Standardized anomalies of monthly sea ice concentration from January to March 2024, relative to the 2001-2020 climatological period. Pixels are greyed out where the climatological mean sea ice concentration was less than 1%.

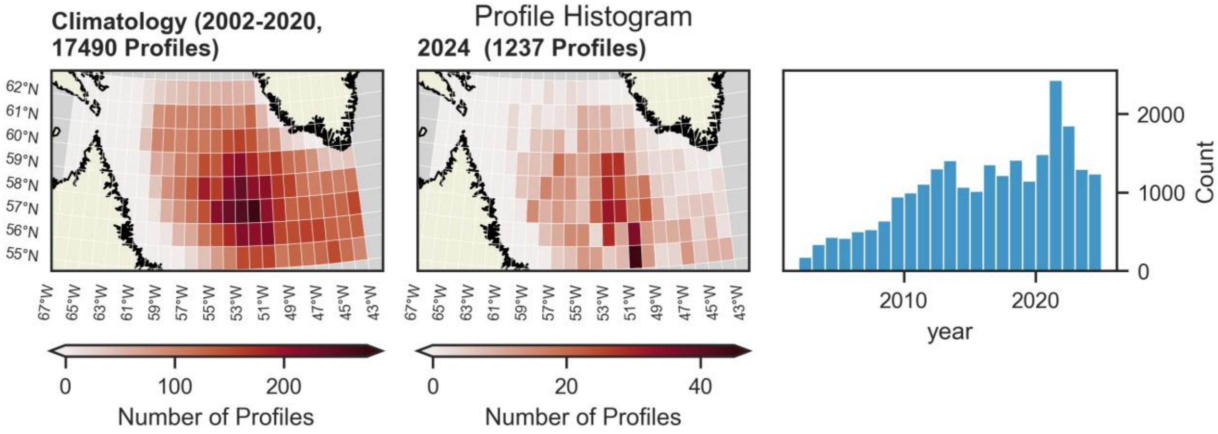

Figure 9. The number of Argo profiles in the Labrador Sea (right: climatology; middle: 2024; right: evolution of the number of profiles).

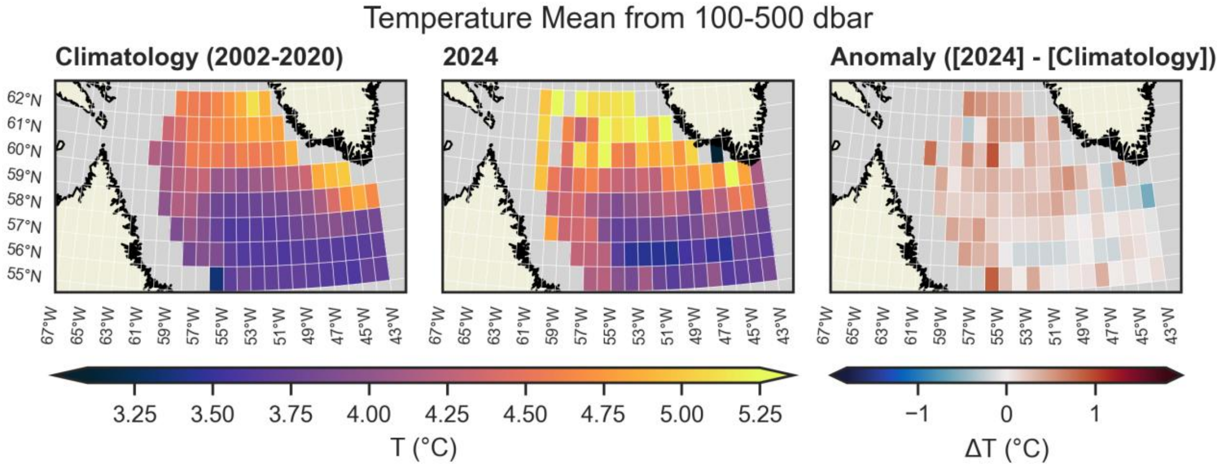

Figure 10. The averaged temperature in the water column in the range of 100-500 dbar, measured by Argo profiles (right: climatology; middle: 2024; left: 2024 anomalies relative to the climatology).

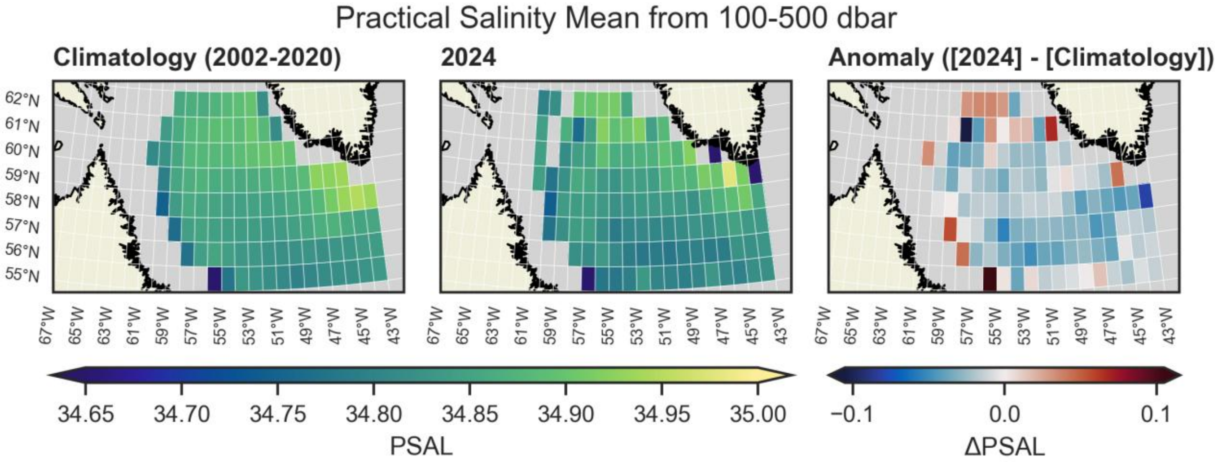

Figure 11. The averaged salinity in the water column in the range of 100-500 dbar, measured by Argo profiles (right: climatology; middle: 2024; left: 2024 anomalies relative to the climatology).

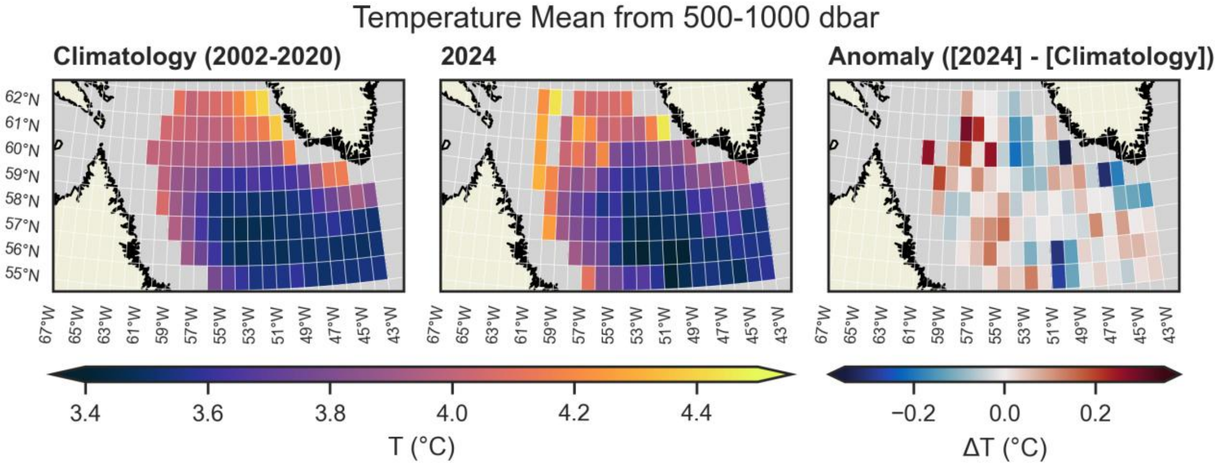

Figure 12. The averaged temperature in the water column in the range of 500-1000 dbar, measured by Argo profiles (right: climatology; middle: 2024; left: 2024 anomalies relative to the climatology).

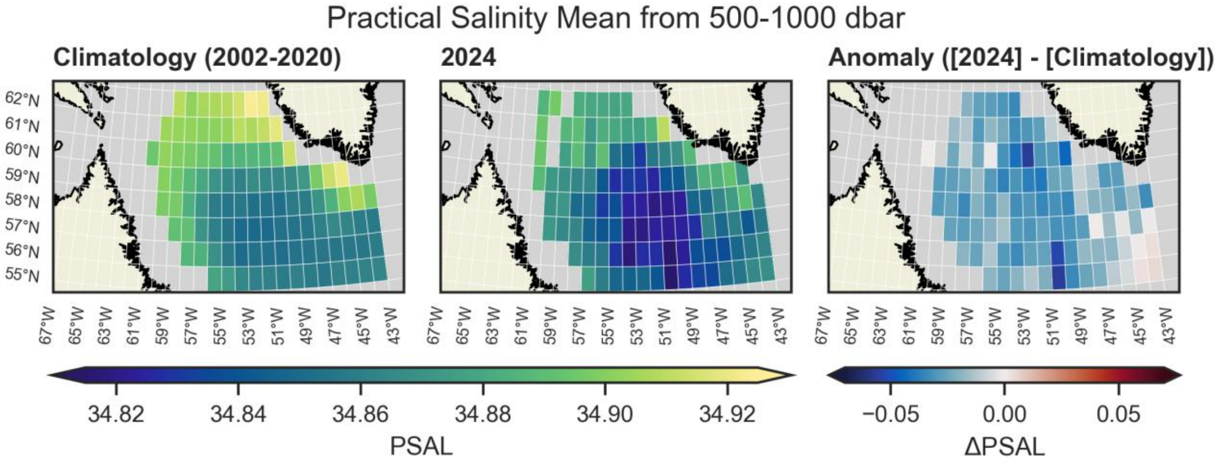

Figure 13. The averaged salinity in the water column in the range of 500-1000 dbar, measured by Argo profiles (right: climatology; middle: 2024; left: 2024 anomalies relative to the climatology).

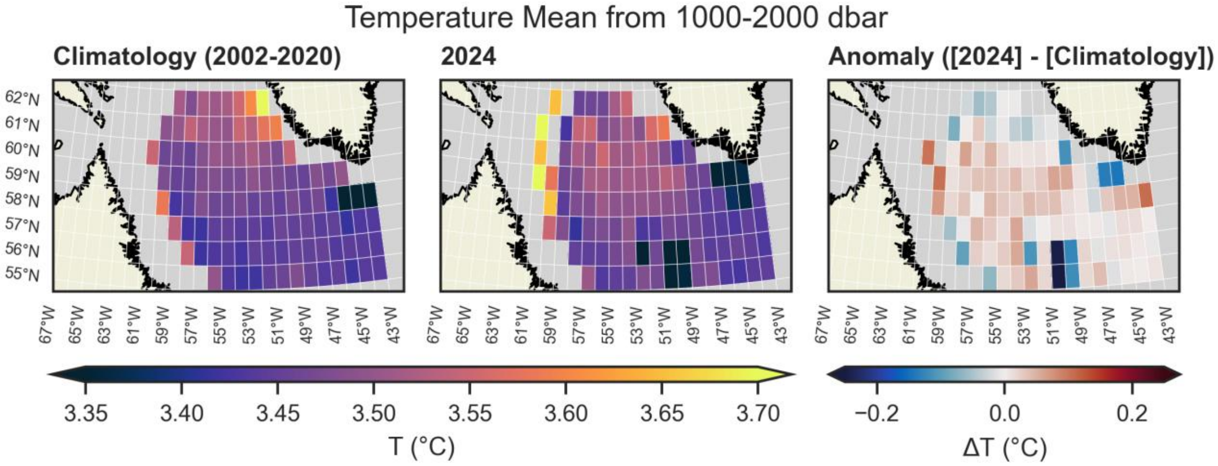

Figure 14. The averaged temperature in the water column in the range of 1000-2000 dbar, measured by Argo profiles (right: climatology; middle: 2024; left: 2024 anomalies relative to the climatology).

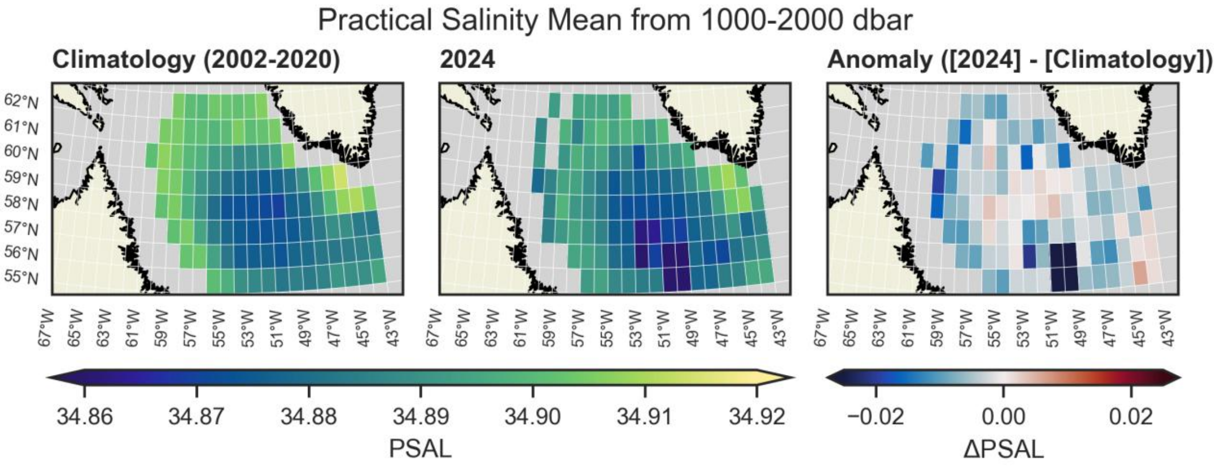

Figure 15. The averaged salinity in the water column in the range of 1000-2000 dbar, measured by Argo profiles (right: climatology; middle: 2024; left: 2024 anomalies relative to the climatology).

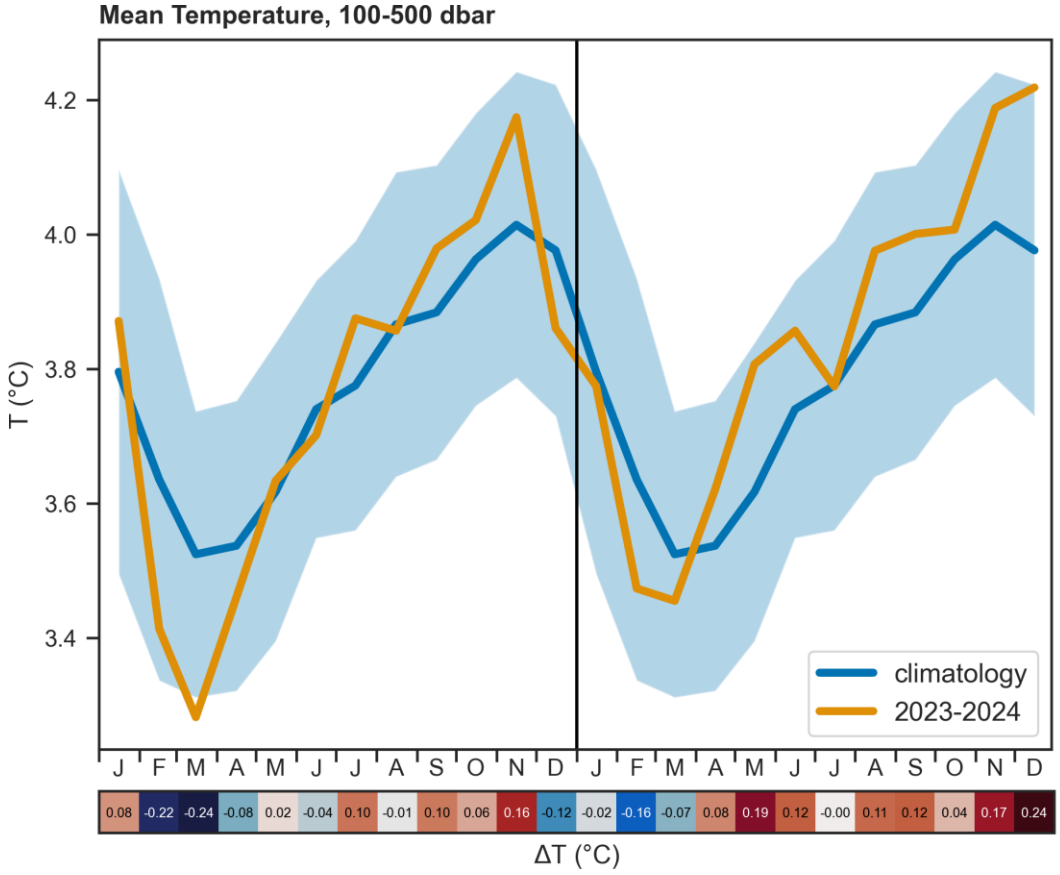

Figure 16. Time series of monthly temperature from 2023 to 2024 (orange) and the climatology of the 2002-2020 period (blue). The shaded area is plus/minus 1 standard deviation. The colours/numbers along the bottom show the difference between 2023/2024 (orange) and climatology (blue) for each month.

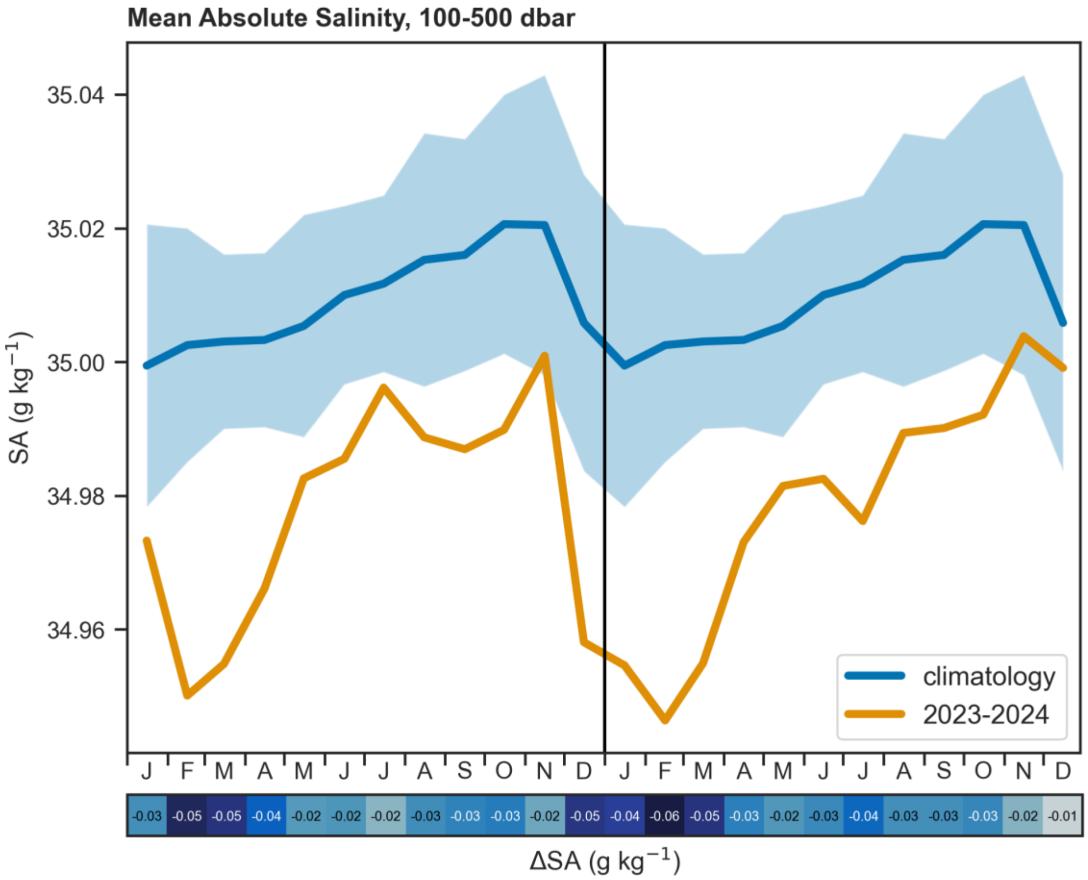

Figure 17. Time series of monthly salinity from 2023 to 2024 (orange) and the climatology of the 2002-2020 period (blue). The shaded area is plus/minus 1 standard deviation. The colours/numbers along the bottom show the difference between 2023/2024 (orange) and climatology (blue) for each month.

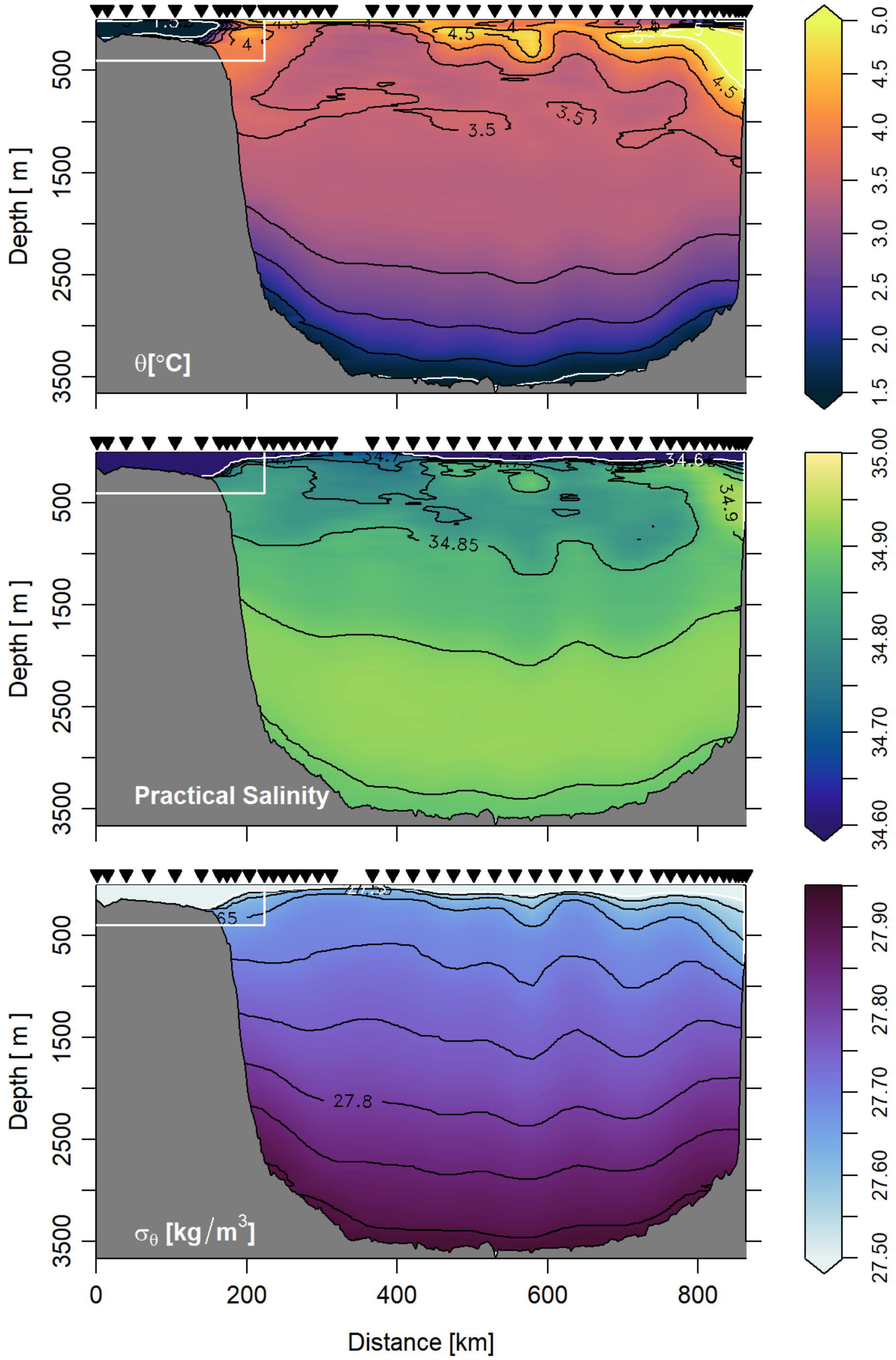

Figure 18. Temperature (top), salinity(middle), and density(bottom) distribution along the AR7W line from the 2024 cruise CTD data. Station locations are indicated by triangles along the top axis.

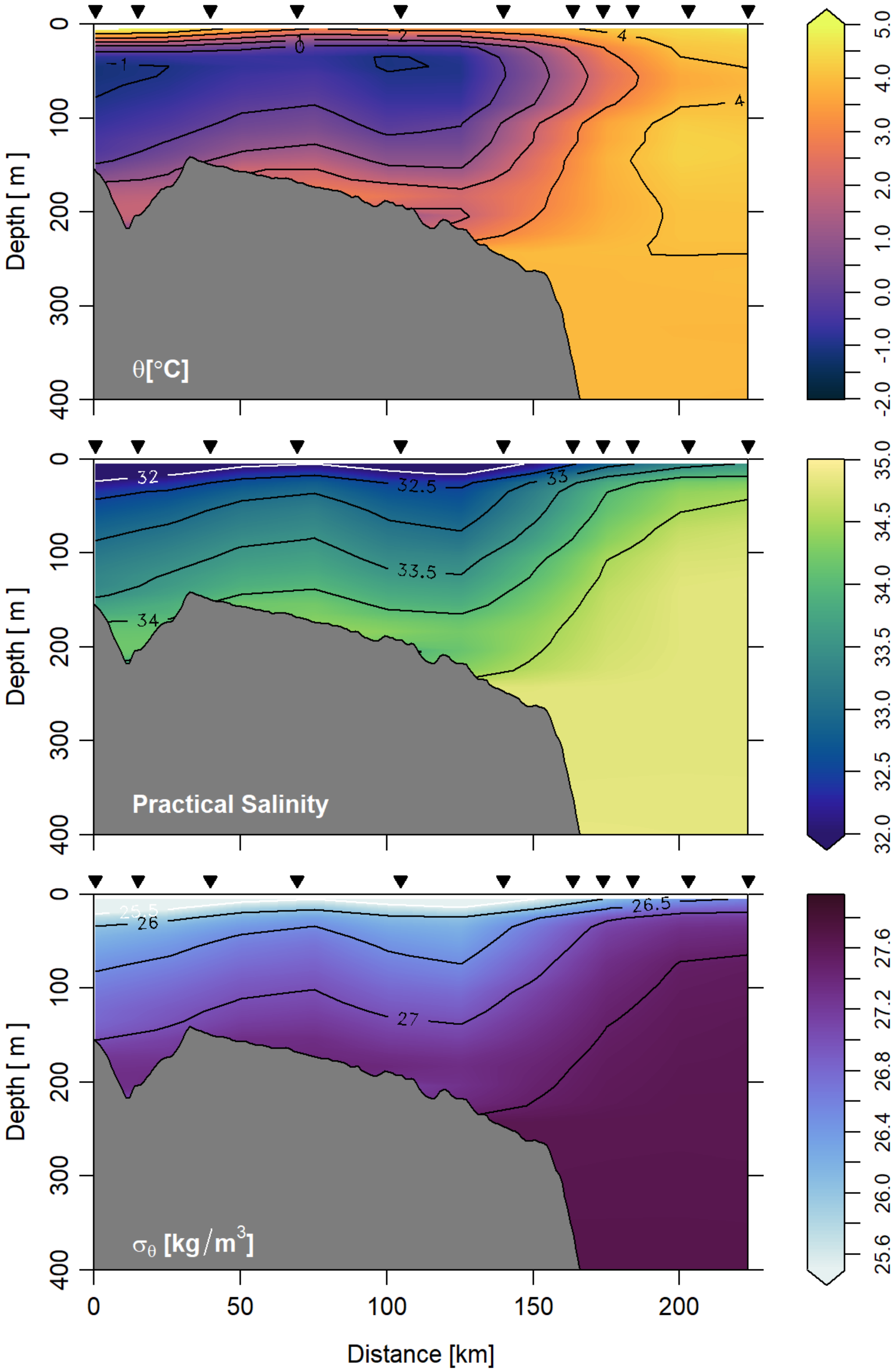

Figure 19. Temperature (top), salinity(middle), and density(bottom) distribution on the Labrador Shelf from the 2024 cruise CTD data. Station locations are indicated by triangles along the top axis.

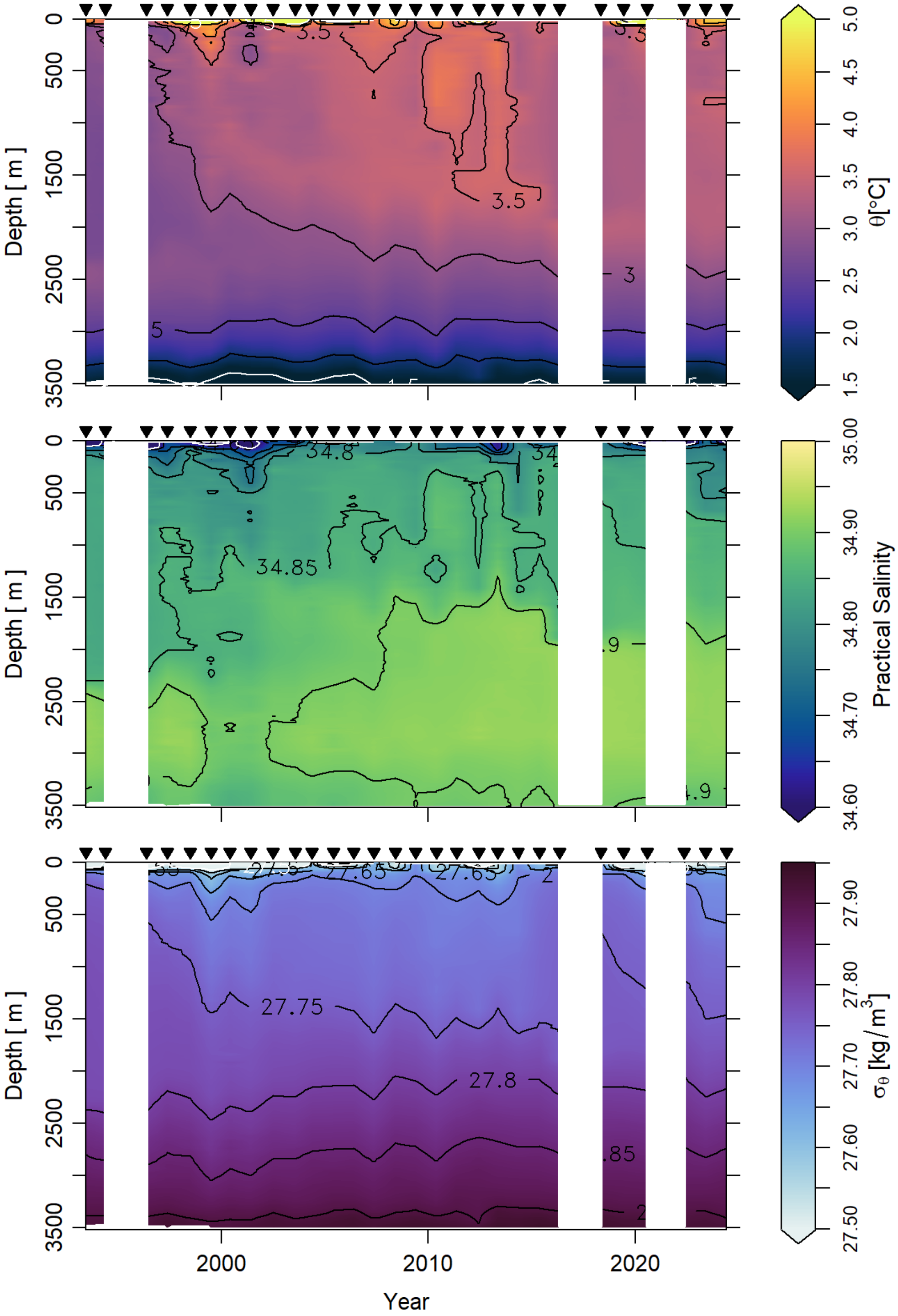

Figure 20. Evolution of the temperature (top), salinity (middle), and density (bottom) from AR7W Station 15.5 in the center of the Labrador Sea from ship CTD data.

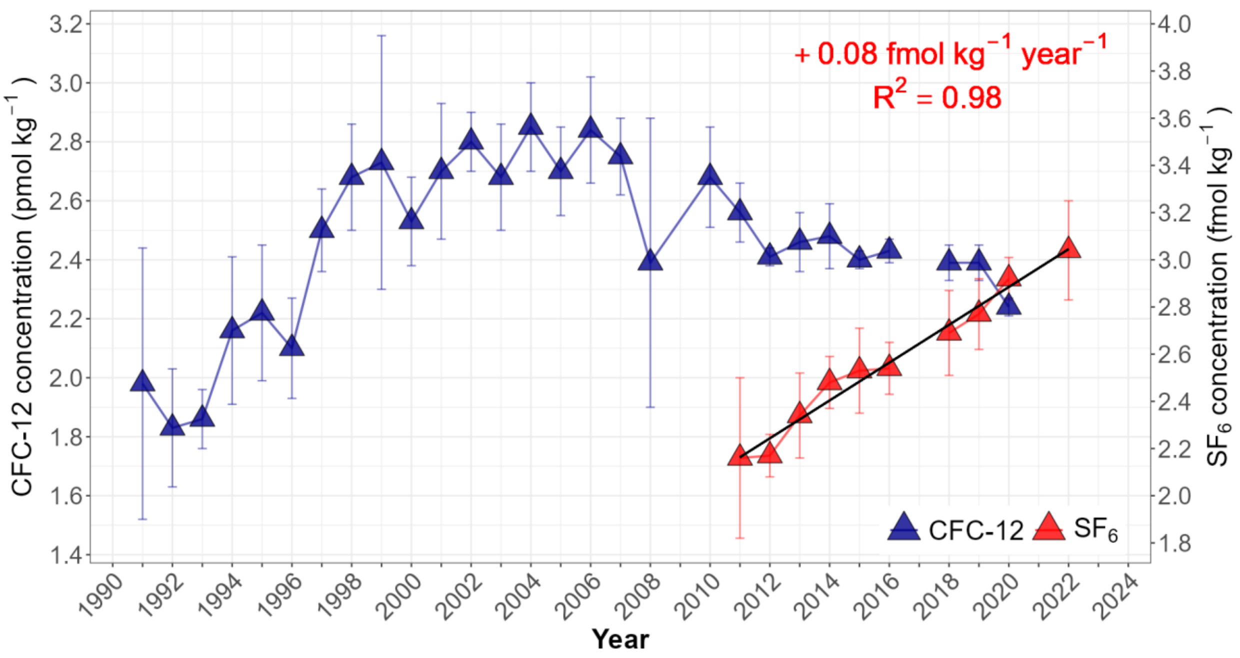

Figure 21. Annual mean concentrations of CFC-12 (blue solid triangles) and SF_6 (red solid triangles) in the Newly Ventilated Labrador Sea Water (150–500 m depth within 56°N to 59.1°N) from 1991 to 2024. Vertical bars indicate one standard deviation and black solid line corresponds to the linear regression of SF_6 against time for the period 2011-2022.

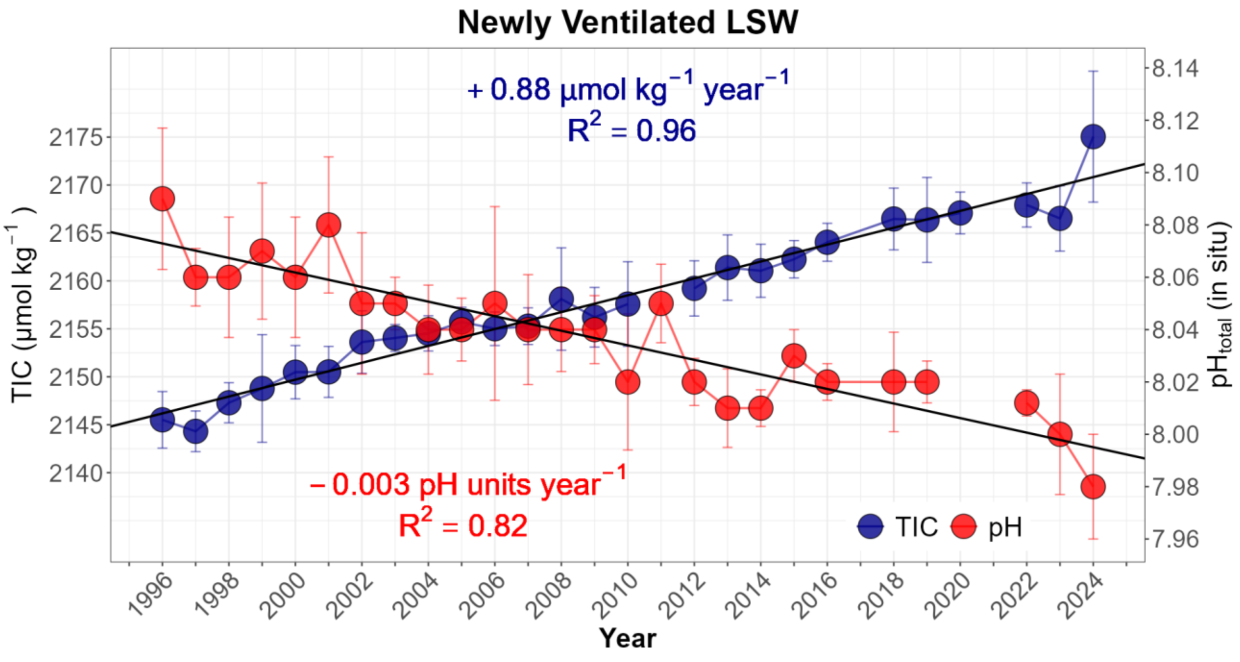

Figure 22. Time series of total inorganic carbon (TIC; blue solid circles) and pH (red solid circles) within the Newly Ventilated Labrador Sea Water (150–500 m depth within 56°N to 59.1°N). Vertical bars indicate one standard deviation and black solid lines correspond to the linear regression of TIC and pH against time for the period 1996-2024.

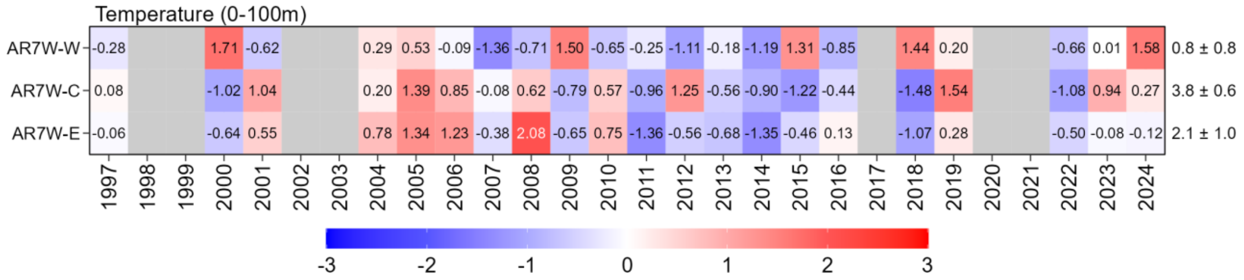

	1997	1998	1999	2000	2001	2002	2003	2004	2005	2006	2007	2008	2009	2010	2011	2012	2013	2014	2015	2016	2017	2018	2019	2020	2021	2022	2023	2024	
AR7W-W	-0.28			1.71	-0.62			0.29	0.53	-0.09	-1.36	-0.71	1.50	-0.65	-0.25	-1.11	-0.18	-1.19	1.31	-0.85		1.44	0.20			-0.66	0.01	1.58	0.8 ± 0.8
AR7W-C	0.08			-1.02	1.04			0.20	1.39	0.85	-0.08	0.62	-0.79	0.57	-0.96	1.25	-0.56	-0.90	-1.22	-0.44		-1.48	1.54			-1.08	0.94	0.27	3.8 ± 0.6
AR7W-E	-0.06			-0.64	0.55			0.78	1.34	1.23	-0.38	2.08	-0.65	0.75	-1.36	-0.56	-0.68	-1.35	-0.46	0.13		-1.07	0.28			-0.50	-0.08	-0.12	2.1 ± 1.0

Figure 23. Scorecards for average temperature in the water column (surface to 100 m) measured from the CTD during each bottle firing, from 1997 to 2023 for the AR7W-West (AR7W-W), AR7W-Central (AR7W-C), and AR7W-East (AR7W-E) polygons. Grey boxes indicate no data or late sampling years (not included in the reference period average). Numbers in the scorecard cells represent the annual standardized anomalies. Numbers on the right side indicate the mean values 1999–2020 (i.e., reference, °C) for a given region as well as the standard deviation (i.e., mean ± standard deviation).

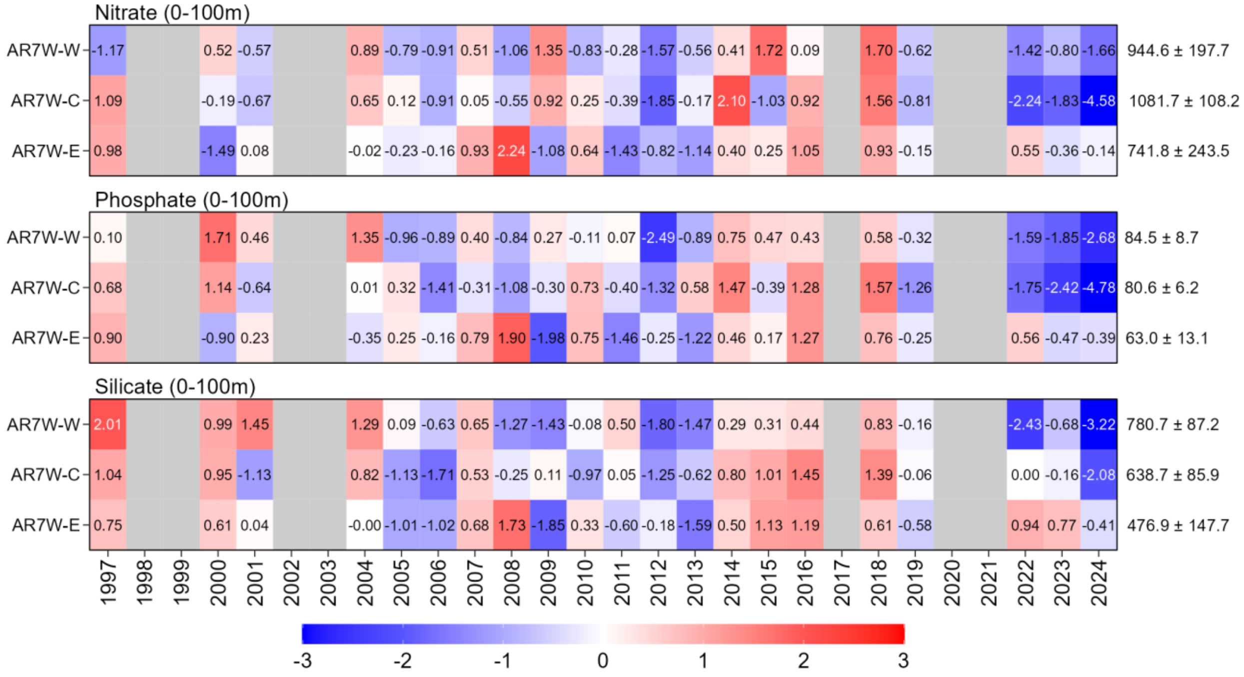

Nitrate (0-100m)

	1997	1998	1999	2000	2001	2002	2003	2004	2005	2006	2007	2008	2009	2010	2011	2012	2013	2014	2015	2016	2017	2018	2019	2020	2021	2022	2023	2024	
AR7W-W	-1.17			0.52	-0.57			0.89	-0.79	-0.91	0.51	-1.06	1.35	-0.83	-0.28	-1.57	-0.56	0.41	1.72	0.09		1.70	-0.62			-1.42	-0.80	-1.66	944.6 ± 197.7
AR7W-C	1.09			-0.19	-0.67			0.65	0.12	-0.91	0.05	-0.55	0.92	0.25	-0.39	-1.85	-0.17	2.10	-1.03	0.92		1.56	-0.81			-2.24	-1.83	-4.58	1081.7 ± 108.2
AR7W-E	0.98			-1.49	0.08			-0.02	-0.23	-0.16	0.93	2.24	-1.08	0.64	-1.43	-0.82	-1.14	0.40	0.25	1.05		0.93	-0.15			0.55	-0.36	-0.14	741.8 ± 243.5

Phosphate (0-100m)

	1997	1998	1999	2000	2001	2002	2003	2004	2005	2006	2007	2008	2009	2010	2011	2012	2013	2014	2015	2016	2017	2018	2019	2020	2021	2022	2023	2024	
AR7W-W	0.10			1.71	0.46			1.35	-0.96	-0.89	0.40	-0.84	0.27	-0.11	0.07	-2.49	-0.89	0.75	0.47	0.43		0.58	-0.32			-1.59	-1.85	-2.68	84.5 ± 8.7
AR7W-C	0.68			1.14	-0.64			0.01	0.32	-1.41	-0.31	-1.08	-0.30	0.73	-0.40	-1.32	0.58	1.47	-0.39	1.28		1.57	-1.26			-1.75	-2.42	-4.78	80.6 ± 6.2
AR7W-E	0.90			-0.90	0.23			-0.35	0.25	-0.16	0.79	1.90	-1.98	0.75	-1.46	-0.25	-1.22	0.46	0.17	1.27		0.76	-0.25			0.56	-0.47	-0.39	63.0 ± 13.1

Silicate (0-100m)

	1997	1998	1999	2000	2001	2002	2003	2004	2005	2006	2007	2008	2009	2010	2011	2012	2013	2014	2015	2016	2017	2018	2019	2020	2021	2022	2023	2024	
AR7W-W	2.01			0.99	1.45			1.29	0.09	-0.63	0.65	-1.27	-1.43	-0.08	0.50	-1.80	-1.47	0.29	0.31	0.44		0.83	-0.16			-2.43	-0.68	-3.22	780.7 ± 87.2
AR7W-C	1.04			0.95	-1.13			0.82	-1.13	-1.71	0.53	-0.25	0.11	-0.97	0.05	-1.25	-0.62	0.80	1.01	1.45		1.39	-0.06			0.00	-0.16	-2.08	638.7 ± 85.9
AR7W-E	0.75			0.61	0.04			-0.00	-1.01	-1.02	0.68	1.73	-1.85	0.33	-0.60	-0.18	-1.59	0.50	1.13	1.19		0.61	-0.58			0.94	0.77	-0.41	476.9 ± 147.7

Figure 24. Scorecards for surface nutrients from 1997 to 2024 for the AR7W-West (AR7W-W), AR7W-Central (AR7W-C), and AR7W-East (AR7W-E) polygons. Grey boxes indicate no data or late sampling years (not included in the reference period average). Numbers in the scorecard cells represent the annual standardized anomalies. Numbers on the right side indicate the mean values 1999–2020 (i.e., reference, mmol m^{-2}) for a given region as well as the standard deviation (i.e., mean ± standard deviation).

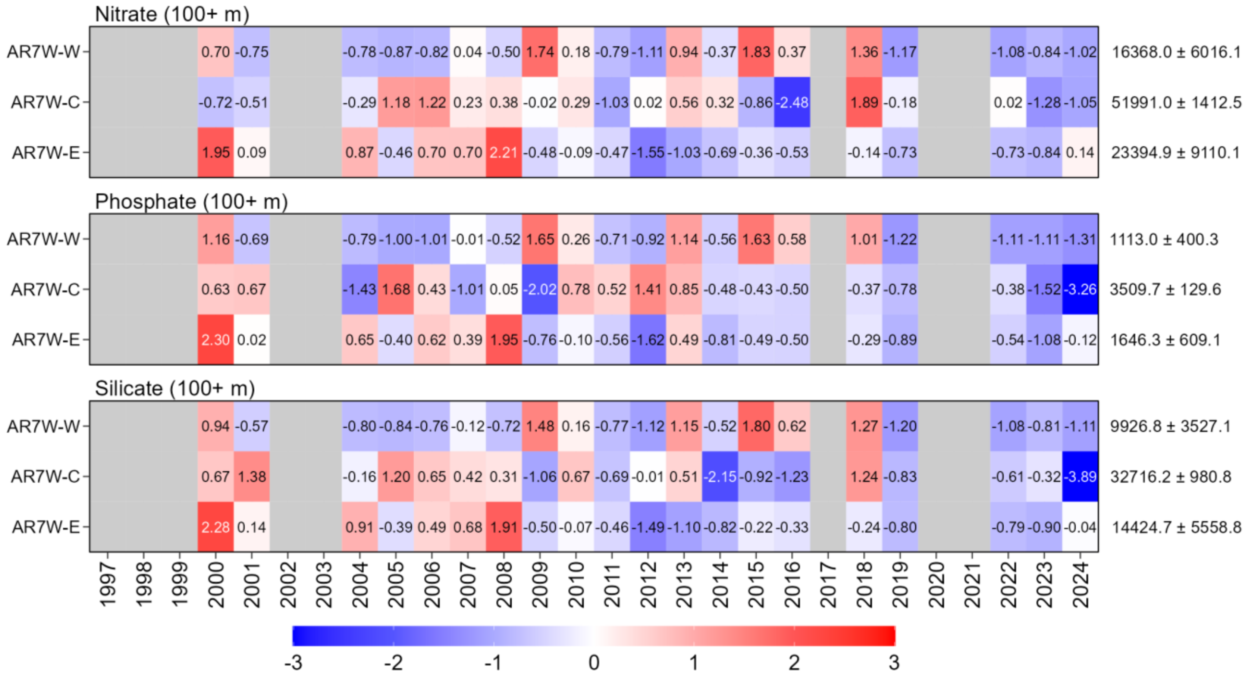

Nitrate (100+ m)

	1997	1998	1999	2000	2001	2002	2003	2004	2005	2006	2007	2008	2009	2010	2011	2012	2013	2014	2015	2016	2017	2018	2019	2020	2021	2022	2023	2024	
AR7W-W				0.70	-0.75			-0.78	-0.87	-0.82	0.04	-0.50	1.74	0.18	-0.79	-1.11	0.94	-0.37	1.83	0.37		1.36	-1.17			-1.08	-0.84	-1.02	16368.0 ± 6016.1
AR7W-C				-0.72	-0.51			-0.29	1.18	1.22	0.23	0.38	-0.02	0.29	-1.03	0.02	0.56	0.32	-0.86	-2.48		1.89	-0.18			0.02	-1.28	-1.05	51991.0 ± 1412.5
AR7W-E				1.95	0.09			0.87	-0.46	0.70	0.70	2.21	-0.48	-0.09	-0.47	-1.55	-1.03	-0.69	-0.36	-0.53		-0.14	-0.73			-0.73	-0.84	0.14	23394.9 ± 9110.1

Phosphate (100+ m)

	1997	1998	1999	2000	2001	2002	2003	2004	2005	2006	2007	2008	2009	2010	2011	2012	2013	2014	2015	2016	2017	2018	2019	2020	2021	2022	2023	2024	
AR7W-W				1.16	-0.69			-0.79	-1.00	-1.01	-0.01	-0.52	1.65	0.26	-0.71	-0.92	1.14	-0.56	1.63	0.58		1.01	-1.22			-1.11	-1.11	-1.31	1113.0 ± 400.3
AR7W-C				0.63	0.67			-1.43	1.68	0.43	-1.01	0.05	-2.02	0.78	0.52	1.41	0.85	-0.48	-0.43	-0.50		-0.37	-0.78			-0.38	-1.52	-3.26	3509.7 ± 129.6
AR7W-E				2.30	0.02			0.65	-0.40	0.62	0.39	1.95	-0.76	-0.10	-0.56	-1.62	0.49	-0.81	-0.49	-0.50		-0.29	-0.89			-0.54	-1.08	-0.12	1646.3 ± 609.1

Silicate (100+ m)

	1997	1998	1999	2000	2001	2002	2003	2004	2005	2006	2007	2008	2009	2010	2011	2012	2013	2014	2015	2016	2017	2018	2019	2020	2021	2022	2023	2024	
AR7W-W				0.94	-0.57			-0.80	-0.84	-0.76	-0.12	-0.72	1.48	0.16	-0.77	-1.12	1.15	-0.52	1.80	0.62		1.27	-1.20			-1.08	-0.81	-1.11	9926.8 ± 3527.1
AR7W-C				0.67	1.38			-0.16	1.20	0.65	0.42	0.31	-1.06	0.67	-0.69	-0.01	0.51	-2.15	-0.92	-1.23		1.24	-0.83			-0.61	-0.32	-3.89	32716.2 ± 980.8
AR7W-E				2.28	0.14			0.91	-0.39	0.49	0.68	1.91	-0.50	-0.07	-0.46	-1.49	-1.10	-0.82	-0.22	-0.33		-0.24	-0.80			-0.79	-0.90	-0.04	14424.7 ± 5558.8

Figure 25. Scorecards for deep nutrients from 1997 to 2024 for the AR7W-West (AR7W-W), AR7W-Central (AR7W-C), and AR7W-East (AR7W-E) polygons. Grey boxes indicate no data or late sampling years (not included in the reference period average). Numbers in the scorecard cells represent the annual standardized anomalies. Numbers on the right side indicate the mean values 1999–2020 (i.e., reference, mmol m^{-2}) for a given region as well as the standard deviation (i.e., mean ± standard deviation).

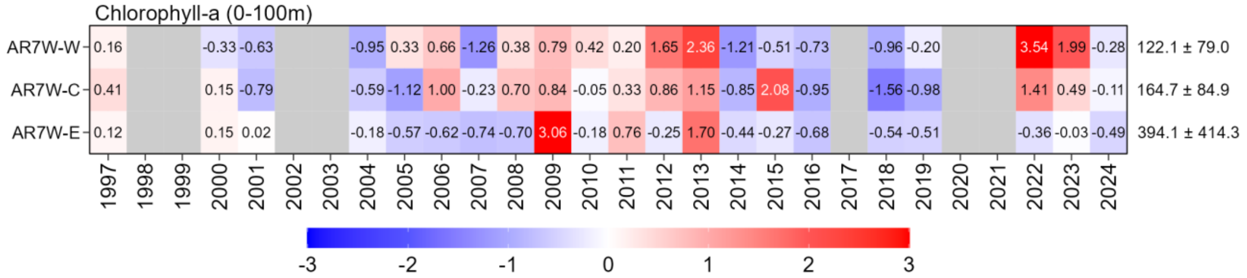

Chlorophyll-a (0-100m)

	1997	1998	1999	2000	2001	2002	2003	2004	2005	2006	2007	2008	2009	2010	2011	2012	2013	2014	2015	2016	2017	2018	2019	2020	2021	2022	2023	2024	
AR7W-W	0.16			-0.33	-0.63			-0.95	0.33	0.66	-1.26	0.38	0.79	0.42	0.20	1.65	2.36	-1.21	-0.51	-0.73		-0.96	-0.20			3.54	1.99	-0.28	122.1 ± 79.0
AR7W-C	0.41			0.15	-0.79			-0.59	-1.12	1.00	-0.23	0.70	0.84	-0.05	0.33	0.86	1.15	-0.85	2.08	-0.95		-1.56	-0.98			1.41	0.49	-0.11	164.7 ± 84.9
AR7W-E	0.12			0.15	0.02			-0.18	-0.57	-0.62	-0.74	-0.70	3.06	-0.18	0.76	-0.25	1.70	-0.44	-0.27	-0.68		-0.54	-0.51			-0.36	-0.03	-0.49	394.1 ± 414.3

Figure 26. Scorecards for in situ chl-a from 1997 to 2024 for the AR7W-West (AR7W-W), AR7W-Central (AR7W-C), and AR7W-East (AR7W-E) polygons. Grey boxes indicate no data or late sampling years (not included in the reference period average). Numbers within cells represent the annual standardized anomalies. Numbers on the right side indicate the mean values 1999–2020 (i.e., reference, mg m^{-2}) for a given region as well as the standard deviation (i.e., mean ± standard deviation).

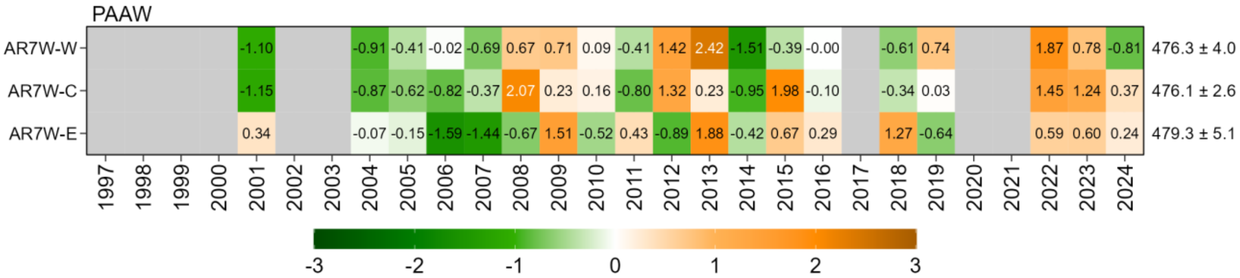

	1997	1998	1999	2000	2001	2002	2003	2004	2005	2006	2007	2008	2009	2010	2011	2012	2013	2014	2015	2016	2017	2018	2019	2020	2021	2022	2023	2024	
AR7W-W					-1.10			-0.91	-0.41	-0.02	-0.69	0.67	0.71	0.09	-0.41	1.42	2.42	-1.51	-0.39	-0.00		-0.61	0.74			1.87	0.78	-0.81	476.3 ± 4.0
AR7W-C					-1.15			-0.87	-0.62	-0.82	-0.37	2.07	0.23	0.16	-0.80	1.32	0.23	-0.95	1.98	-0.10		-0.34	0.03			1.45	1.24	0.37	476.1 ± 2.6
AR7W-E					0.34			-0.07	-0.15	-1.59	-1.44	-0.67	1.51	-0.52	0.43	-0.89	1.88	-0.42	0.67	0.29		1.27	-0.64			0.59	0.60	0.24	479.3 ± 5.1

Figure 27. Scorecards for PAAW metric derived from surface phytoplankton absorption measurements from 1997 to 2024 for the AR7W-West (AR7W-W), AR7W-Central (AR7W-C), and AR7W-East (AR7W-E) polygons. Grey boxes indicate no data. Numbers within cells represent the annual standardized anomalies. Numbers on the right side indicate the mean values 1999–2020 (i.e., reference) for a given region as well as the standard deviation (i.e., mean ± standard deviation).

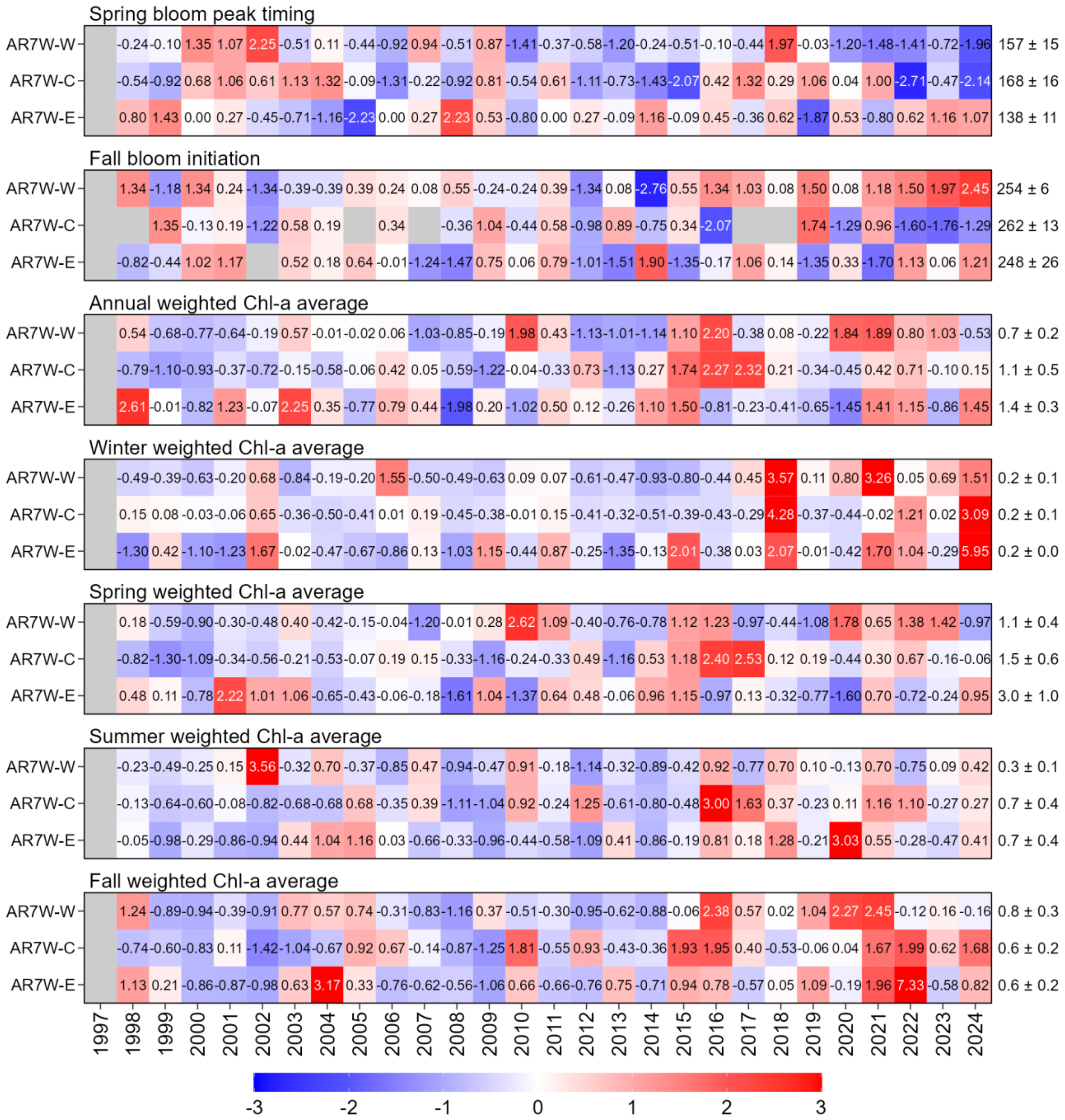

Spring bloom peak timing

	1997	1998	1999	2000	2001	2002	2003	2004	2005	2006	2007	2008	2009	2010	2011	2012	2013	2014	2015	2016	2017	2018	2019	2020	2021	2022	2023	2024	
AR7W-W		-0.24	-0.10	1.35	1.07	2.25	-0.51	0.11	-0.44	-0.92	0.94	-0.51	0.87	-1.41	-0.37	-0.58	-1.20	-0.24	-0.51	-0.10	-0.44	1.97	-0.03	-1.20	-1.48	-1.41	-0.72	-1.96	157 ± 15
AR7W-C		-0.54	-0.92	0.68	1.06	0.61	1.13	1.32	-0.09	-1.31	-0.22	-0.92	0.81	-0.54	0.61	-1.11	-0.73	-1.43	-2.07	0.42	1.32	0.29	1.06	0.04	1.00	-2.71	-0.47	-2.14	168 ± 16
AR7W-E		0.80	1.43	0.00	0.27	-0.45	-0.71	-1.16	-2.23	0.00	0.27	2.23	0.53	-0.80	0.00	0.27	-0.09	1.16	-0.09	0.45	-0.36	0.62	-1.87	0.53	-0.80	0.62	1.16	1.07	138 ± 11

Fall bloom initiation

	1997	1998	1999	2000	2001	2002	2003	2004	2005	2006	2007	2008	2009	2010	2011	2012	2013	2014	2015	2016	2017	2018	2019	2020	2021	2022	2023	2024	
AR7W-W		1.34	-1.18	1.34	0.24	-1.34	-0.39	-0.39	0.39	0.24	0.08	0.55	-0.24	-0.24	0.39	-1.34	0.08	-2.76	0.55	1.34	1.03	0.08	1.50	0.08	1.18	1.50	1.97	2.45	254 ± 6
AR7W-C			1.35	-0.13	0.19	-1.22	0.58	0.19		0.34		-0.36	1.04	-0.44	0.58	-0.98	0.89	-0.75	0.34	-2.07			1.74	-1.29	0.96	-1.60	-1.76	-1.29	262 ± 13
AR7W-E		-0.82	-0.44	1.02	1.17		0.52	0.18	0.64	-0.01	-1.24	-1.47	0.75	0.06	0.79	-1.01	-1.51	1.90	-1.35	-0.17	1.06	0.14	-1.35	0.33	-1.70	1.13	0.06	1.21	248 ± 26

Annual weighted Chl-a average

	1997	1998	1999	2000	2001	2002	2003	2004	2005	2006	2007	2008	2009	2010	2011	2012	2013	2014	2015	2016	2017	2018	2019	2020	2021	2022	2023	2024	
AR7W-W		0.54	-0.68	-0.77	-0.64	-0.19	0.57	-0.01	-0.02	0.06	-1.03	-0.85	-0.19	1.98	0.43	-1.13	-1.01	-1.14	1.10	2.20	-0.38	0.08	-0.22	1.84	1.89	0.80	1.03	-0.53	0.7 ± 0.2
AR7W-C		-0.79	-1.10	-0.93	-0.37	-0.72	-0.15	-0.58	-0.06	0.42	0.05	-0.59	-1.22	-0.04	-0.33	0.73	-1.13	0.27	1.74	2.27	2.32	0.21	-0.34	-0.45	0.42	0.71	-0.10	0.15	1.1 ± 0.5
AR7W-E		2.61	-0.01	-0.82	1.23	-0.07	2.25	0.35	-0.77	0.79	0.44	-1.98	0.20	-1.02	0.50	0.12	-0.26	1.10	1.50	-0.81	-0.23	-0.41	-0.65	-1.45	1.41	1.15	-0.86	1.45	1.4 ± 0.3

Winter weighted Chl-a average

	1997	1998	1999	2000	2001	2002	2003	2004	2005	2006	2007	2008	2009	2010	2011	2012	2013	2014	2015	2016	2017	2018	2019	2020	2021	2022	2023	2024	
AR7W-W		-0.49	-0.39	-0.63	-0.20	0.68	-0.84	-0.19	-0.20	1.55	-0.50	-0.49	-0.63	0.09	0.07	-0.61	-0.47	-0.93	-0.80	-0.44	0.45	3.57	0.11	0.80	3.26	0.05	0.69	1.51	0.2 ± 0.1
AR7W-C		0.15	0.08	-0.03	-0.06	0.65	-0.36	-0.50	-0.41	0.01	0.19	-0.45	-0.38	-0.01	0.15	-0.41	-0.32	-0.51	-0.39	-0.43	-0.29	4.28	-0.37	-0.44	-0.02	1.21	0.02	3.09	0.2 ± 0.1
AR7W-E		-1.30	0.42	-1.10	-1.23	1.67	-0.02	-0.47	-0.67	-0.86	0.13	-1.03	1.15	-0.44	0.87	-0.25	-1.35	-0.13	2.01	-0.38	0.03	2.07	-0.01	-0.42	1.70	1.04	-0.29	5.95	0.2 ± 0.0

Spring weighted Chl-a average

	1997	1998	1999	2000	2001	2002	2003	2004	2005	2006	2007	2008	2009	2010	2011	2012	2013	2014	2015	2016	2017	2018	2019	2020	2021	2022	2023	2024	
AR7W-W		0.18	-0.59	-0.90	-0.30	-0.48	0.40	-0.42	-0.15	-0.04	-1.20	-0.01	0.28	2.62	1.09	-0.40	-0.76	-0.78	1.12	1.23	-0.97	-0.44	-1.08	1.78	0.65	1.38	1.42	-0.97	1.1 ± 0.4
AR7W-C		-0.82	-1.30	-1.09	-0.34	-0.56	-0.21	-0.53	-0.07	0.19	0.15	-0.33	-1.16	-0.24	-0.33	0.49	-1.16	0.53	1.18	2.40	2.53	0.12	0.19	-0.44	0.30	0.67	-0.16	-0.06	1.5 ± 0.6
AR7W-E		0.48	0.11	-0.78	2.22	1.01	1.06	-0.65	-0.43	-0.06	-0.18	-1.61	1.04	-1.37	0.64	0.48	-0.06	0.96	1.15	-0.97	0.13	-0.32	-0.77	-1.60	0.70	-0.72	-0.24	0.95	3.0 ± 1.0

Summer weighted Chl-a average

	1997	1998	1999	2000	2001	2002	2003	2004	2005	2006	2007	2008	2009	2010	2011	2012	2013	2014	2015	2016	2017	2018	2019	2020	2021	2022	2023	2024	
AR7W-W		-0.23	-0.49	-0.25	0.15	3.56	-0.32	0.70	-0.37	-0.85	0.47	-0.94	-0.47	0.91	-0.18	-1.14	-0.32	-0.89	-0.42	0.92	-0.77	0.70	0.10	-0.13	0.70	-0.75	0.09	0.42	0.3 ± 0.1
AR7W-C		-0.13	-0.64	-0.60	-0.08	-0.82	-0.68	-0.68	0.68	-0.35	0.39	-1.11	-1.04	0.92	-0.24	1.25	-0.61	-0.80	-0.48	3.00	1.63	0.37	-0.23	0.11	1.16	1.10	-0.27	0.27	0.7 ± 0.4
AR7W-E		-0.05	-0.98	-0.29	-0.86	-0.94	0.44	1.04	1.16	0.03	-0.66	-0.33	-0.96	-0.44	-0.58	-1.09	0.41	-0.86	-0.19	0.81	0.18	1.28	-0.21	3.03	0.55	-0.28	-0.47	0.41	0.7 ± 0.4

Fall weighted Chl-a average

	1997	1998	1999	2000	2001	2002	2003	2004	2005	2006	2007	2008	2009	2010	2011	2012	2013	2014	2015	2016	2017	2018	2019	2020	2021	2022	2023	2024	
AR7W-W		1.24	-0.89	-0.94	-0.39	-0.91	0.77	0.57	0.74	-0.31	-0.83	-1.16	0.37	-0.51	-0.30	-0.95	-0.62	-0.88	-0.06	2.38	0.57	0.02	1.04	2.27	2.45	-0.12	0.16	-0.16	0.8 ± 0.3
AR7W-C		-0.74	-0.60	-0.83	0.11	-1.42	-1.04	-0.67	0.92	0.67	-0.14	-0.87	-1.25	1.81	-0.55	0.93	-0.43	-0.36	1.93	1.95	0.40	-0.53	-0.06	0.04	1.67	1.99	0.62	1.68	0.6 ± 0.2
AR7W-E		1.13	0.21	-0.86	-0.87	-0.98	0.63	3.17	0.33	-0.76	-0.62	-0.56	-1.06	0.66	-0.66	-0.76	0.75	-0.71	0.94	0.78	-0.57	0.05	1.09	-0.19	1.96	7.33	-0.58	0.82	0.6 ± 0.2

Figure 28. Scorecards for seasonal surface chl-a metrics derived from the OC-CCI multi satellite sensor product (timing is the day of year, and averages are measured in mg m^{-3}) from 1998 to 2024 for the AR7W-West (AR7W-W), AR7W-Central (AR7W-C), and AR7W-East (AR7W-E) polygons. Grey boxes indicate no data. Numbers within cells represent the annual standardized anomalies. Numbers on the right side indicate the mean values 1999–2020 (i.e., reference) for a given region as well as the standard deviation (i.e., mean ± standard deviation).

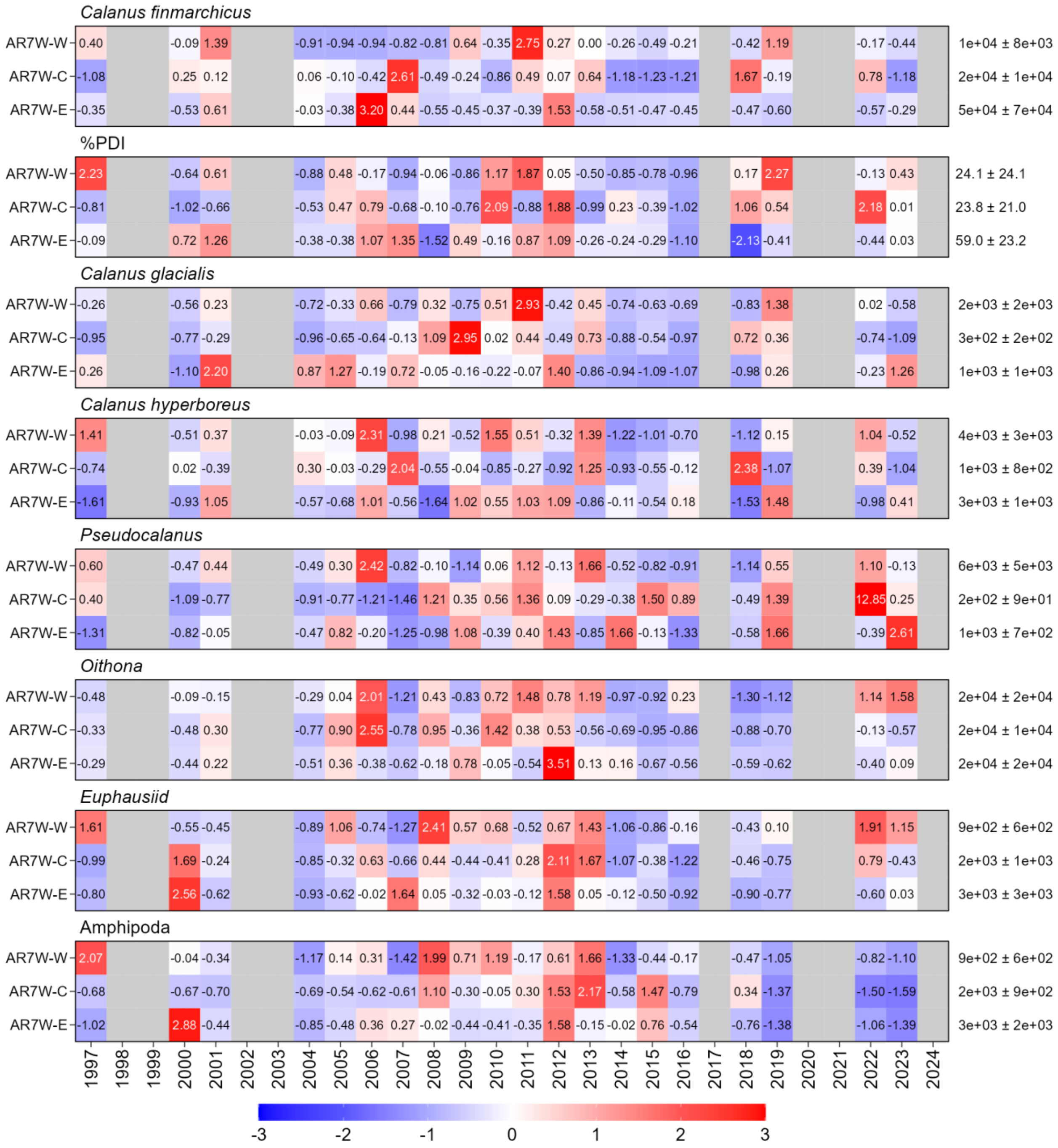

	1997	1998	1999	2000	2001	2002	2003	2004	2005	2006	2007	2008	2009	2010	2011	2012	2013	2014	2015	2016	2017	2018	2019	2020	2021	2022	2023	2024	
Calanus finmarchicus																													
AR7W-W	0.40			-0.09	1.39			-0.91	-0.94	-0.94	-0.82	-0.81	0.64	-0.35	2.75	0.27	0.00	-0.26	-0.49	-0.21		-0.42	1.19			-0.17	-0.44		1e+04 ± 8e+03
AR7W-C	-1.08			0.25	0.12			0.06	-0.10	-0.42	2.61	-0.49	-0.24	-0.86	0.49	0.07	0.64	-1.18	-1.23	-1.21		1.67	-0.19			0.78	-1.18		2e+04 ± 1e+04
AR7W-E	-0.35			-0.53	0.61			-0.03	-0.38	3.20	0.44	-0.55	-0.45	-0.37	-0.39	1.53	-0.58	-0.51	-0.47	-0.45		-0.47	-0.60			-0.57	-0.29		5e+04 ± 7e+04
%PDI																													
AR7W-W	2.23			-0.64	0.61			-0.88	0.48	-0.17	-0.94	-0.06	-0.86	1.17	1.87	0.05	-0.50	-0.85	-0.78	-0.96		0.17	2.27			-0.13	0.43		24.1 ± 24.1
AR7W-C	-0.81			-1.02	-0.66			-0.53	0.47	0.79	-0.68	-0.10	-0.76	2.09	-0.88	1.88	-0.99	0.23	-0.39	-1.02		1.06	0.54			2.18	0.01		23.8 ± 21.0
AR7W-E	-0.09			0.72	1.26			-0.38	-0.38	1.07	1.35	-1.52	0.49	-0.16	0.87	1.09	-0.26	-0.24	-0.29	-1.10		-2.13	-0.41			-0.44	0.03		59.0 ± 23.2
Calanus glacialis																													
AR7W-W	-0.26			-0.56	0.23			-0.72	-0.33	0.66	-0.79	0.32	-0.75	0.51	2.93	-0.42	0.45	-0.74	-0.63	-0.69		-0.83	1.38			0.02	-0.58		2e+03 ± 2e+03
AR7W-C	-0.95			-0.77	-0.29			-0.96	-0.65	-0.64	-0.13	1.09	2.95	0.02	0.44	-0.49	0.73	-0.88	-0.54	-0.97		0.72	0.36			-0.74	-1.09		3e+02 ± 2e+02
AR7W-E	0.26			-1.10	2.20			0.87	1.27	-0.19	0.72	-0.05	-0.16	-0.22	-0.07	1.40	-0.86	-0.94	-1.09	-1.07		-0.98	0.26			-0.23	1.26		1e+03 ± 1e+03
Calanus hyperboreus																													
AR7W-W	1.41			-0.51	0.37			-0.03	-0.09	2.31	-0.98	0.21	-0.52	1.55	0.51	-0.32	1.39	-1.22	-1.01	-0.70		-1.12	0.15			1.04	-0.52		4e+03 ± 3e+03
AR7W-C	-0.74			0.02	-0.39			0.30	-0.03	-0.29	2.04	-0.55	-0.04	-0.85	-0.27	-0.92	1.25	-0.93	-0.55	-0.12		2.38	-1.07			0.39	-1.04		1e+03 ± 8e+02
AR7W-E	-1.61			-0.93	1.05			-0.57	-0.68	1.01	-0.56	-1.64	1.02	0.55	1.03	1.09	-0.86	-0.11	-0.54	0.18		-1.53	1.48			-0.98	0.41		3e+03 ± 1e+03
Pseudocalanus																													
AR7W-W	0.60			-0.47	0.44			-0.49	0.30	2.42	-0.82	-0.10	-1.14	0.06	1.12	-0.13	1.66	-0.52	-0.82	-0.91		-1.14	0.55			1.10	-0.13		6e+03 ± 5e+03
AR7W-C	0.40			-1.09	-0.77			-0.91	-0.77	-1.21	-1.46	1.21	0.35	0.56	1.36	0.09	-0.29	-0.38	1.50	0.89		-0.49	1.39			12.85	0.25		2e+02 ± 9e+01
AR7W-E	-1.31			-0.82	-0.05			-0.47	0.82	-0.20	-1.25	-0.98	1.08	-0.39	0.40	1.43	-0.85	1.66	-0.13	-1.33		-0.58	1.66			-0.39	2.61		1e+03 ± 7e+02
Oithona																													
AR7W-W	-0.48			-0.09	-0.15			-0.29	0.04	2.01	-1.21	0.43	-0.83	0.72	1.48	0.78	1.19	-0.97	-0.92	0.23		-1.30	-1.12			1.14	1.58		2e+04 ± 2e+04
AR7W-C	-0.33			-0.48	0.30			-0.77	0.90	2.55	-0.78	0.95	-0.36	1.42	0.38	0.53	-0.56	-0.69	-0.95	-0.86		-0.88	-0.70			-0.13	-0.57		2e+04 ± 1e+04
AR7W-E	-0.29			-0.44	0.22			-0.51	0.36	-0.38	-0.62	-0.18	0.78	-0.05	-0.54	3.51	0.13	0.16	-0.67	-0.56		-0.59	-0.62			-0.40	0.09		2e+04 ± 2e+04
Euphausiid																													
AR7W-W	1.61			-0.55	-0.45			-0.89	1.06	-0.74	-1.27	2.41	0.57	0.68	-0.52	0.67	1.43	-1.06	-0.86	-0.16		-0.43	0.10			1.91	1.15		9e+02 ± 6e+02
AR7W-C	-0.99			1.69	-0.24			-0.85	-0.32	0.63	-0.66	0.44	-0.44	-0.41	0.28	2.11	1.67	-1.07	-0.38	-1.22		-0.46	-0.75			0.79	-0.43		2e+03 ± 1e+03
AR7W-E	-0.80			2.56	-0.62			-0.93	-0.62	-0.02	1.64	0.05	-0.32	-0.03	-0.12	1.58	0.05	-0.12	-0.50	-0.92		-0.90	-0.77			-0.60	0.03		3e+03 ± 3e+03
Amphipoda																													
AR7W-W	2.07			-0.04	-0.34			-1.17	0.14	0.31	-1.42	1.99	0.71	1.19	-0.17	0.61	1.66	-1.33	-0.44	-0.17		-0.47	-1.05			-0.82	-1.10		9e+02 ± 6e+02
AR7W-C	-0.68			-0.67	-0.70			-0.69	-0.54	-0.62	-0.61	1.10	-0.30	-0.05	0.30	1.53	2.17	-0.58	1.47	-0.79		0.34	-1.37			-1.50	-1.59		2e+03 ± 9e+02
AR7W-E	-1.02			2.88	-0.44			-0.85	-0.48	0.36	0.27	-0.02	-0.44	-0.41	-0.35	1.58	-0.15	-0.02	0.76	-0.54		-0.76	-1.38			-1.06	-1.39		3e+03 ± 2e+03

Figure 29. Scorecards for mesozooplankton abundances from 1997 to 2024 for AR7W-West (AR7W-W), AR7W-Central (AR7W-C), and AR7W-East (AR7W-E) expressed as normalized anomalies (dimensionless) based on 1999–2020 reference period. The second panel from the top shows the Population Development Index (%PDI) calculated as the sum abundance of *C. finmarchicus* copepodite CI-CIII * 100 and divided by the sum of all developmental stages. Numbers on the right side indicate the mean values 1999–2020 (i.e., reference period) for a given region as well as the standard deviation (i.e., mean number of individuals per m^2 ± standard deviation). Grey cells indicate anomalies were omitted due to late sampling or that no sampling occurred that year due to lack of vessel (2017, 2021).

Appendix

Ocean Color Polygon Seasons

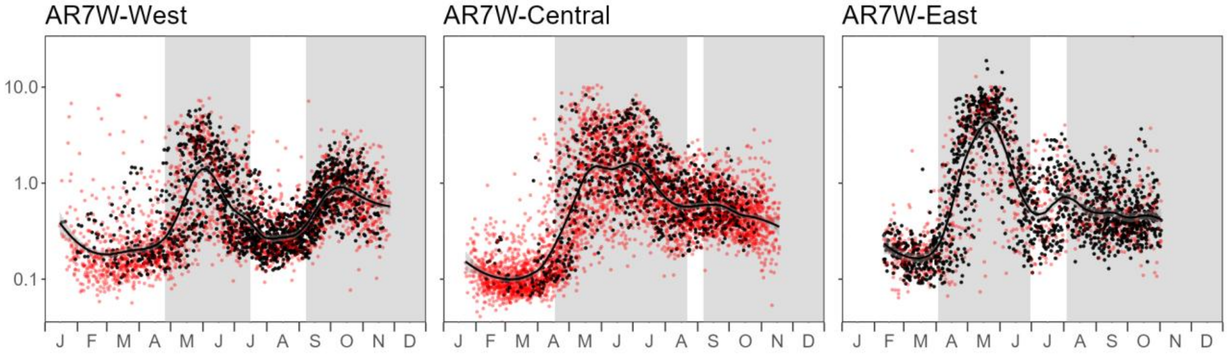

Figure 30. Time series of daily average concentrations within each Labrador Sea polygon over the climatological period (1999-2020). Grey shaded areas indicate the spring and fall bloom periods (i.e., region-specific 'seasons'). White areas indicate the winter and summer 'seasons'. Red circles corresponds to daily data coverage of less than 20% of a polygon. Days of the year marking the transition from winter to spring, spring to summer, and summer to fall are 116, 197, and 251 (AR7W-West), 108, 234, and 250 (AR7W-Central), and 93, 181, and 216 (AR7W-East).